Effect verification of wicking fabric on inhibition to frost heave at cold region pavement

寒冷地舗装の凍上抑制に対するウィッキングファブリックの効果検証

By

Yuwei WU

A thesis submitted in partial fulfillment of the requirements for the degree of Doctor of Philosophy in Engineering
under the guidance and supervision of
Professor Tatsuya ISHIKAWA

Examined by the Doctoral Committee
Professor Tatsuya ISHIKAWA
Professor Yoichi WATABE
Professor Satoshi NISHIMURA

September 2022

English Engineering Education Program (e3)
Laboratory of Analytical Geomechanics
Division of Field Engineering for the Environment
Graduate School of Engineering
Hokkaido University
Sapporo, Hokkaido, Japan

ABSTRACT

Pavements in the cold region may be seriously damaged by frost heave. The frost heave generates as follows: water in the large void freezes under the freezing point and results in ice crystals, meanwhile, the remaining water in small capillaries or absorbed as a film on the soil particle surface remain unfrozen. This unfrozen water has lower free energy at a lower negative temperature. Thus, the gradient of the water potential develops along with the gradient of the temperature. Thus, water may be drawn up from the warm portion and contribute to the formation of pore ice. Eventually, as the pores ice particles grow, they can connect with each other to form an ice lens, and this will result in the soil expanding. The expansion of soil in pavements during the freezing process may cause a significant deformation and result in road failures. To eliminate or reduce the freezing effect and inhibit the frost heave, reducing the moisture migration to the freezing front is an effective way. In order to inhibit frost heave during the freezing process, a new geotextile, wicking fabric (WF) that can drain water from the unsaturated frost- susceptible soil has been invented. However, the effectiveness of the WF in inhibiting frost heave during the freezing process was rarely invested in the previous studies. Therefore, in this study, both laboratory experiments and numerical simulations are conducted to investigate the inhibitory effect of WF on frost heave. As the soil in most of the base layers is unsaturated, experimental and numerical studies for unsaturated soil with and without WF installed were carried out to analyze the water migration during the freezing process. In the laboratory experiments, the one-dimensional frost heave tests were implemented to examine the frost susceptibility of soil samples, and the effects of various experimental factors (such as cooling rate, soil type, overburden pressure, water supply system, and initial saturation) on the frost heave. In addition, model tests were conducted to determine the frost heave inhibition effect by installing WF during the freezing process.

To better understand the inhibition effect of WF on frost heave, a thermo-hydro-mechanical (THM) coupled model was established. The proposed THM coupled model considers the interaction between the temperature field, the hydraulic field, and the mechanical field during the freezing process. The coupled relations are described by combining the Richards equation, the mass conservation equation, and the Navier equation. These partial differential equations are numerically solved by finite element software (COMSOL). The energy conversation equation is used to describe heat transfer and latent heat during ice-water phase change in the thermal field. The VG model is introduced to describe volumetric water content variation in unsaturated soils in the hydraulic field. The deformation of soil during freezing is described by introducing a linear elastic model in the mechanical field. Besides, in order to accurately simulate the water migration and the frost heave of soil-WF

system during freezing, an evaporation model was developed to describe the boundary condition of the WF and reproduce the evaporation and water absorption process of the WF. The proposed evaporation model simplifies the water absorption and drainage process of the WF, taking into account the effects of ambient temperature, soil temperature, and soil water content variation during freezing on the water drainage efficiency of the WF. The model can quickly predict the drainage effect of WF during freezing, while optimizing the simulation process of WF-soil system in which the water absorption effect of WF varies with the environmental conditions.

The validity and applicability of the THM coupled model are verified by comparing frost heave test results with the simulation results under different experimental conditions. Meanwhile, the validity of the evaporation model is confirmed by comparing the model test results with the simulation results. Both results show the effectiveness of WF on frost heave inhibition. Finally, the effect of different experimental conditions on the ability of WF to inhibit frost heave was investigated by simulating the model with and without WF under various experimental conditions (soil type, groundwater table, and cooling rate). According to the frost heave test, the frost heave is proportional to initial saturation and inversely proportional to cooling rate and overburden pressure. Furthermore, the opened system (with water supply) can cause a larger frost heave deformation than the closed system (without water supply). On the other hand, based on the model test results, soil samples with WF installed produce significantly less frost heave under the same freezing conditions than without WF. Moreover, soil types, cooling rates, and the groundwater table can also affect the efficacy of WF in inhibiting frost heave. WF produces better suppression in the following situations: soil samples with low permeability, low cooling rates, and a lower groundwater table.

Last but not least, since the existing models which use some ideal simplification conditions in predicting the inhibition effect of WF on frost heave may overestimate the suppression effect when the practical application may not meet the simplification criteria, the proposed model is applied to pavement sections with and without buried WF to illustrate the performance and practicality. By providing a continuous water supply and a sufficient contact surface between the WF and the surrounding dry atmosphere during the freezing process, the proposed model can successfully simulate the frost heave inhibition effect of the WF. The comparison of simulation results with experimental results has demonstrated the applicability of the proposed model in reproducing water migration in the WF-soil system. The model is also shown to be capable of simulating the effect of WF on frost heave inhibition accurately.

Chapter 1 introduces the background, objective, main technical path, and organization of this study. Chapter 2 introduces the development, classification, and summary of THM coupled models, and also summarizes the current state of research on WF. Chapter 3 introduces the theoretical foundations used in this study, including the THM coupling model and the evaporation model. Chapter 4 introduces the frost heave test with a THM coupled model built based on the theory proposed in Chapter 3 to verify the validity of the numerical model by comparing the test and simulation results. Chapter 5 presents the model tests of WF. By comparing the model test results with simulation results, the validity of the evaporation model is verified. Furthermore, the frost heave and water redistribution of both with and without the WF model are simulated under different experimental conditions. Chapter 6 shows the field test of WF in the test pavement and the numerical simulation to verify the performance and practicality of the numerical model proposed in this study. Chapter 7 summarizes the conclusions and recommendations of the study.

< This dissertation is a modified and revised form of the following original journals and proceedings>

1. Wu, Y.W., Ishikawa, T* Coupled THM analysis on the Freezing-Thaw behavior of pavement with Wicking Fabric. 60th Annual meeting of Hokkaido Branch Japanese Geotechnical Society. 11-18. Hokkaido, Japan, 2018.1.25-2018.1.26.
2. Wu, Y.W., Ishikawa, T*., Maruyama, K., Ueno, C., Yasuoka, T., & Okuda, S. (2022). Modeling Wicking Fabric Inhibition Effect on Frost Heave. Applied Sciences, 12(9), 4357.
3. Wu, Y.W., Ishikawa, T*(2022). A thermal-hydrao-mechanical coupled analysis on frost susceptible soils. Sciences in Cold and Arid Regions, 4 (14) (in press)
4. Yasuoka, T., Ishikawa, T., Luo, B., Wu, Y.W., Maruyama, K., & Ueno, C. (2022). Coupled Analysis on Frost-Heaving Depression Effect of Geosynthetics Drainage Material for Road Pavement. In Advances in Transportation Geotechnics IV (pp. 509-520). Springer, Cham.

ACKNOWLEDGEMENT

First and foremost, I would like to express my deepest gratitude and appreciation to my supervisor Prof. Tatsuya Ishikawa for his guidance, valuable advice, and continuous support throughout my doctoral study. I have been deeply influenced by Prof. Tatsuya Ishikawa's immense specialized knowledge, outstanding academic level, and stringent academic spirit throughout my doctoral program. I am very pleased and privileged to be one of his students, and his guidance becomes a precious part of my lifelong heritage. There are no words to adequately express my gratitude to such an amazing advisor.

Professor Ishikawa proposed this topic, provided generous amounts of time and intellectual effort towards problem-solving discussions, and provided encouragement and emotional support. All of the articles reviewed in this study were delivered and suggested by Professor Ishikawa to the author. Throughout the completion of this study, his thoughtful advice, constructive criticism, and constant support have made it a pleasant and satisfying experience for the author.

My deep appreciation goes to all members of the doctoral committee, Prof. Yoichi Watabe, and Prof. Satoshi Nishimura for their valuable comments, constructive suggestions, and tremendous support not only on this dissertation but also on the annual evaluations. It would not have been possible to complete this dissertation without their help.

I would like to express my sincere gratitude to Sho Okuda and Tomohisa Yasuoka, who provided a great deal of help to make the experimental part of this article possible. The discussions with Drs. Luo Bin and Zhu Yulong provided a deeper understanding of the numerical model as well. I would like to acknowledge the students from the Laboratory of Analytical Geomechanics for their help during these three years. In addition, I would like to extend my sincere thanks to my friends in Sapporo because without their support, it would be very hard for me to cope with the difficulties.

I would like to wholeheartedly thank my boyfriend, Xingyue Ren, and our parents. In addition to supporting me in my studies and in my personal life, Dr. Ren has taken utmost care of me during my doctoral study.Their love and unconditional support encourage me to overcome any difficulties in my life. I feel honored to be their loved one. This dissertation cannot be accomplished without their love.

TABLE OF CONTENTS

LIST OF FIGURES

LIST OF TABLES

1 INTRODUCTION

1.1 Background

Approximately half of the land surface is covered by cold zones(Yu et al., 2022). Several infrastructure projects have been implemented in the region, including the Harbin-Qiqihar High-Speed Railway, Trans-Siberian Railway, the Alaska Highway, the Harbin-Dalian High-Speed Railway, and the Qinghai-Xizang Railway(Wu et al., 2008). Frost heave has been discovered as a key cause of engineering failure in the cold area throughout the construction and operation processes(Janoo and Berg, 1990; Roy et al., 1992; Zhang and Kevern, 2021). Damages caused by frost heave include swellings (shown in Figure 1.1(a), fatigue cracks (shown in Figure 1.1(b)), potholes (shown in Figure 1.1(c)), corrugations (shown in Figure 1.1(d)), edge cracks (shown in Figure 1.1(e)), etc.(Miller and Bellinger, 2003; Zhang and Kevern, 2021).

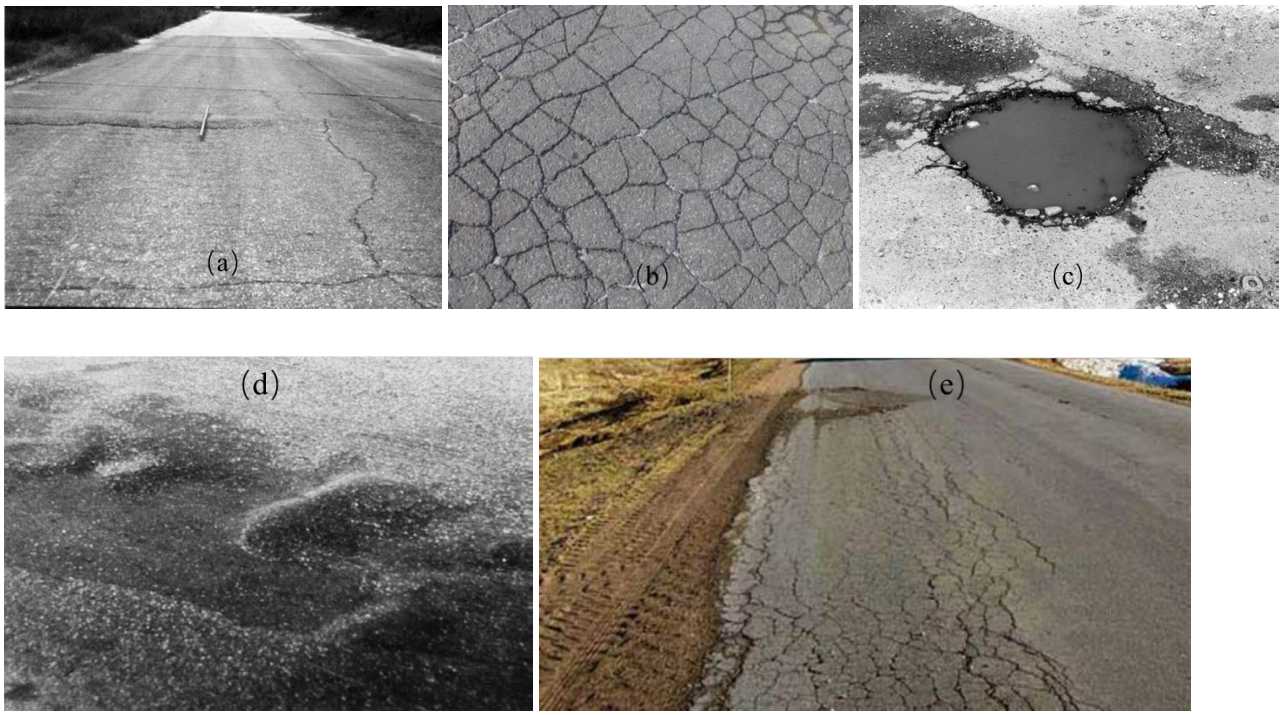

Figure 1.1 Different types of pavement damage caused by frost heave. (a). Swellings; (b) Fatigue cracks; (c) Potholes; (d) Corrugations; (e) Edge Cracks. (adapted from Miller and Bellinger, 2003; Zhang and Kevern, 2021).

In order to mitigate or eliminate the damage caused by frost heave to cold region pavements, it is important to understand: (1) the mechanisms and conditions under which frost heave takes place, in other words, how frost heave damages cold

region pavements. (2), the measures that inhibit the occurrence of frost heave and the effectiveness of these measures in inhibiting frost heave. An extensive study has been undertaken to answer these questions and to propose a tool that can predict the frost heave on soils during the freezing process.

1.1.1 Frost heave occurrence

In general, frost heave refers to the uplifting of the soil surface that occurs as a result of the freezing of water in the soil, which is ice lensing. A portion of the additional water can be drawn upward from the unfrozen soil beneath the freezing front by the freezing process. This is typically much greater than that caused simply by the expansion of water after freezing (about 9%)(Peterson and Krantz, 2003). It has been demonstrated by Taber (1929, 1930), who carried out frost heave tests in soils with benzene, which contracts upon freezing, to replace the pore water. Even though the soil was saturated with benzene, frost heaving still occurred during freezing. Consequently, the expansion of water when it freezes is not the primary cause of frost heave. It is the ice lens formation that is responsible for the frost heave. Mellor(1970) confirms Taber's view that unfrozen water exists at -10°C and that seepage paths in this form allow water to continuously migrate to the freezing front. For the mechanism of water migration, British physical chemist Everett first proposed the theory that water flow is driven by surface tension at the ice-water interface, and the presence of a curved liquid surface at the ice-water interface is direct evidence of the existence of surface tension. For the mechanism of water migration, British physical chemist Everett(Edlefsen and Anderson, 1943) proposed the theory that water flow is driven by surface tension at the ice-water interface, and the presence of a curved liquid surface at the ice-water interface is direct evidence of the existence of surface tension. The ice lens forms because of the different chemical potentials of the ice and supercooled pore water contained within the soil cause the water to be attracted to the ice lenses. The presence of a thin film of unfrozen water at the interface between ice and soil particles provides uniform thickening of the ice lenses(Derjaguin and Churaev, 1978). The film allows water to flow around the soil particles and provide an even supply to the lenses. As shown in Figure 1.2 (a) (Lay, 2005), ice lenses are formed in a frost heave test specimen. Moreover, as depicted in Figure 1.2 (b), the mechanism of ice lensing is also discussed as well as the moisture migration in the frost soils (Rosenqvist et al., 2016). In summary, it is generally recognized that three factors lead to the formation of ice lenses, and hence the formation of frost heave, are frost-susceptible soil (a significant amount of fines in the soil); subfreezing temperatures (freezing temperatures must penetrate the soil, and, in general, thicker lenses will result from slower freezing rates); and water (must be available from the groundwater table, infiltration, an aquifer, or held within the voids of fine-grained soil) (Chamberlain, 1981; Holtz et al., 1981). The frost heave will be eliminated or minimized if any one of the above conditions is removed.

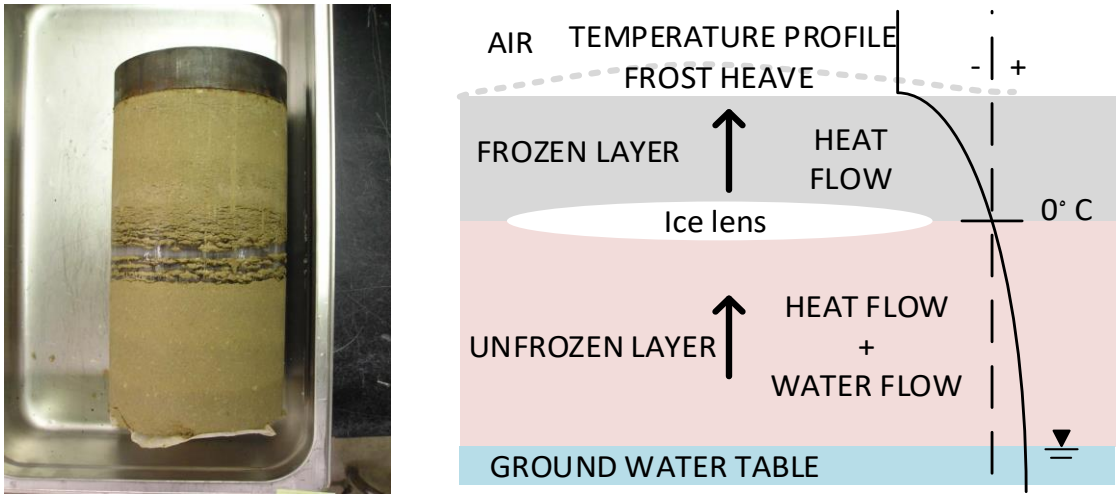

Figure 1.2 Illustration of ice lenses growth (a) ice lensing specimen; (b) microscopic ice lenses growth in soil.

1.1.2 Limitation of the conventional frost heave inhibition system and new system with WF

For frost heave to occur, three conditions must be met: (1) freezing temperature, (2) frost susceptible soils, and (3) the presence of a continuous source of water (Holtz et al., 1981) . Removing any of the three factors above will eliminate or dramatically reduce the frost heave. Typical measures include replacing frost susceptible soils with non-susceptible ones, installing insulation layers to reduce frost penetration, increasing overburden pressure, and installing a capillary barrier to stop the water flow to reduce surface water accumulation (Kinosita, 1989; Sheng, 1994; Ye et al., 2007).

As for the first condition, i.e., minimizing the effects of temperature changes on pavement during freezing. A common practice nowadays is to add insulation to pavements, such as structural polymer foam. The study by Edgar et al (2014). investigated the use of structural polymer injections underneath the pavement to prevent freezing. By injecting structural polymer beneath the pavement, a thermal barrier is formed that reduces heat loss beneath the pavement, preventing freezing fronts from propagating to the roadbed. By creating an insulating layer, the foam both supports the pavement and reduces heat loss. The thermal state of the foam layer is measured by placing thermistors above and below the foam layer. It was found that the temperature beneath the polymer was maintained at or above the freezing point, thereby controlling the frost heave. The ground measurement data showed that the frost heave is reduced from 3 in to 0.5 in. (75 to 13 mm) over two winters, while untreated areas still showed a frost heave of 3 in.

For the second point, one common way to prevent frost heave is to replace frost-susceptible soils with nonfrost-susceptible materials. In accordance with this idea, Gieselman (2007) conducted an experiment to investigate the mechanism of this

method of inhibiting frost heave by replacing a frost-susceptible layer (hydrophobic layer) between the frost front and the groundwater table. The experimental results showed that in the hydrophobic layer, the freezing front advanced more rapidly and therefore the surrounding water did not have enough time to migrate to the freezing edge. Compared to the soil before replacement, fewer ice lenses are formed during freezing and less water is released during thawing in the replacement soil layer. Consequently, the replacement soil layer could reduce the amount of water absorbed from the groundwater table during winter, thereby reducing the total amount of freezing and swelling occurs.

In regard to the third point, geosynthetics are commonly used as capillary barriers to reduce the excess water supply during the freezing process. Henry and Holtz (2011) investigated this method by freezing cylindrical soil specimens containing geosynthetics from the top side. In order to induce potential ice lenses to form during the freezing process, the specimen was supplied with water from the bottom. These results demonstrate that dry geosynthetics and fine soils can act as capillary barriers to prevent frost heave. However, a moist geotextile containing fine soils will not act as a capillary barrier. The reason for this is that geotextiles possess a considerable wet and dry hysteresis, meaning that wet geotextiles are more likely to absorb and transmit water than dry ones when subjected to the same suction (Zhang et al., 2019). Likewise, an effective capillary barrier will allow frost penetration more quickly than the original soil. While the soil beneath it may bulge during thawing, the soil above it will have a much lower moisture content and therefore maintain soil strength. Despite the fact that the capillary barrier reduces the amount of water on the upper side of the geotextile, excess water can still accumulate below the geotextile since the geotextile only prevents the upward migration of water and does not remove excess water from the roadbed. As a consequence, the soil beneath the geotextile will lose its stiffness due to the accumulation of water.

Given the high cost of transporting materials to the remote site and the long distance, the most practical method for reducing frost heave is reducing the water content in the pavement structure (Lin et al., 2017). Recently, geotextiles and geocomposites have been used as capillary barriers in pavements to reduce water absorption and frost heaving. However, capillary barriers only obstruct the upward flow of capillary water and the excess water could accumulate beneath the capillary barriers. Further, if the groundwater table is shallow and the base course contains more than 4% fine particles, the soil's content will continuously increase due to capillary action(Siswosoebrotho and Widodo, 2005). This will ultimately reduce the pavement stiffness. The conventional geotextile installed drainage system is shown in Figure 1.3(a). In order to resolve the above issues of conventional geotextiles in engineering applications, type of woven geotextile with wicking ability was recently developed that is capable of providing both lateral drainage and minimize upward water migration in both saturated and unsaturated conditions (Zhang et al., 2012). As shown in Figure 1.3 (b), when WF was

installed in the subgrade, the air humidity above the roadway is typically dry (less than 50% relative humidity) and the soil, as well as the geotextile, are wet (close to 100% relative humidity), a large suction gradient would form between the geotextile and soil (Zhang et al., 2012). Thus, installing WF in the subgrade helps carry both gravitational and capillary water to the facing of the road slopes and eventually evaporated to the ambient atmosphere. Specifically, upwardly migrating moisture that reached the WF can be laterally diverted to the pavement shoulders (Zornberg et al., 2017).

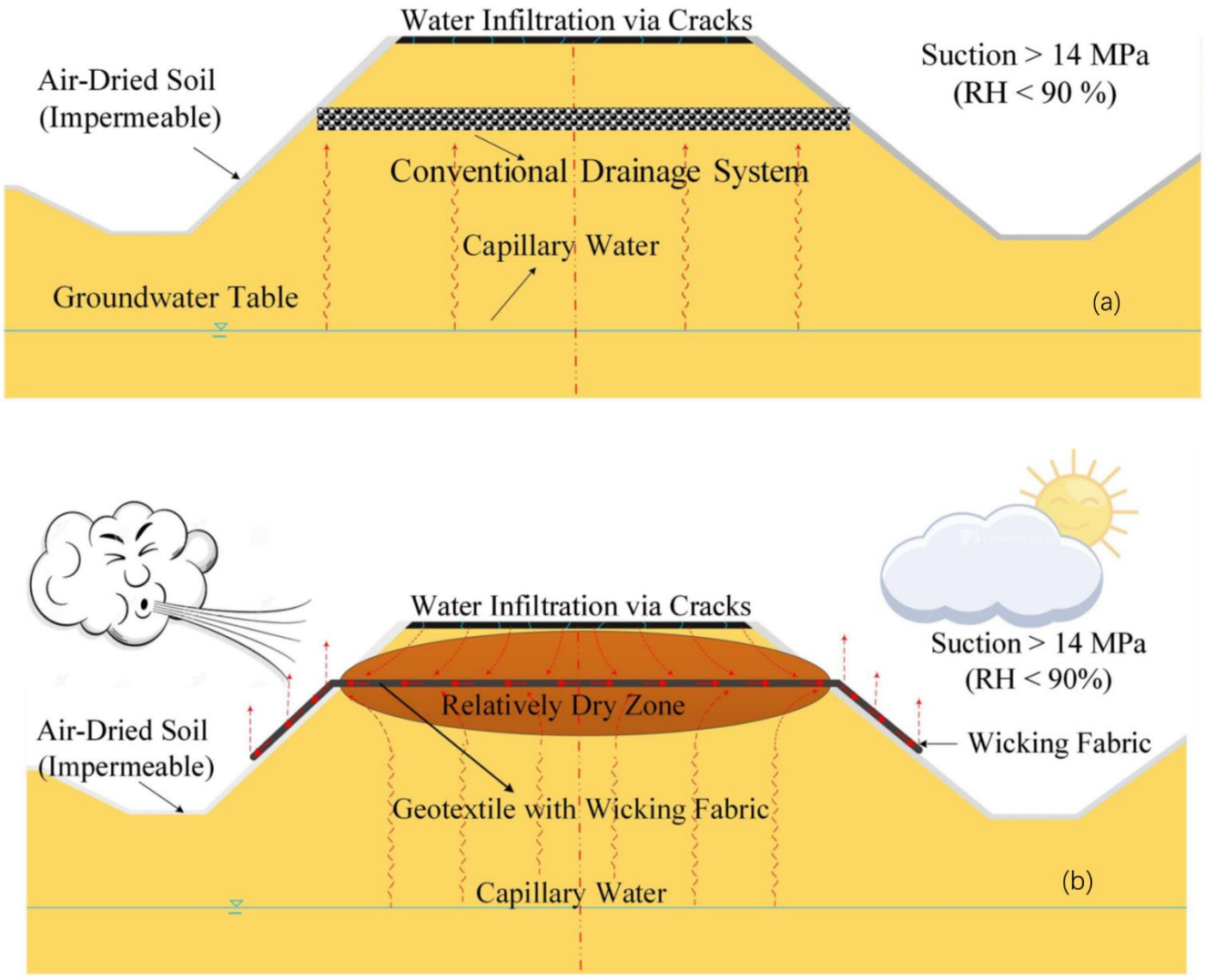

Figure 1.3 Pavement structure water drainage system installed with (a) conventional geotextile; (b) wicking fabric (adapted from Lin et al. (2019)).

1.2 Research Objectives

The purpose of this thesis is to explore the inhibiting effect of WF on frost heave under freezing conditions by analyzing the thermal-hydro-mechanical (THM) coupled relationships. For this purpose, this study attempts to,

1. Propose a THM coupled model to reproduce the freezing process of unsaturated soil;
2. Examine the applicability and validity of the proposed model by comparing the simulation results with the test data during freezing process for Touryo and Tomakomai soil;
3. Do the parametric studies under different initial saturation, overburden pressure, cooling rates, and drainage and supply (open and close system) conditions;
4. Propose a numerical model which can describe the water absorption process of WF during the freezing process and predict the frost heave of soil-WF system;
5. Discuss the applicability and reliability of the proposed model by comparing numerical simulations with test results of laboratory model test;
6. Conduct parametric analysis under different analytical conditions (soil type, groundwater table, and cooling rate) to investigate the relationship between the experimental conditions and the frost heave inhibition effect of WF;
7. Illustrate the performance and practicality of the proposed model by applied the model to the pavement sections with and without buried WF.

1.3 Research Methodology

The focus of the research in this thesis is to discuss the inhibitory effect of WF on frost heave considering the Thermal-hydro-mechanical (THM) coupled relations on frost heave under freezing conditions. For this purpose, this study attempts to,

1. experimentally examining frost heave susceptibility of soil samples, as well as examining the effectiveness of various experimental conditions (e.g. water supply system, soil type, cooling rate, initial saturation, and overburden pressure) on frost heave.
2. propose a coupled THM model to simulate the unsaturated soil freezing behavior, using the finite element method (FEM) to solve the model numerically. The proposed model should be able to reproduce the unsaturated soil freezing process under a variety of experimental conditions.
3. conducted model tests to compare the frost heave of the soil installed with and without WF, demonstrating the inhibitory effect of WF on frost heave.

4. develop a numerical model which simulates the water drainage behavior of WF during the freezing process while taking into account variations in soil water content and the water drainage efficiency of WF over time.

5. investigate the factors that may affect the water drainage efficiency of WF during the freezing process.

The following methodological steps have been established, and each is considered a prerequisite for the next step. A brief description of these methodological steps follows.

(1) 1-D Frost heave test

(2) Mechanistic THM coupled modeling

(3) Numerical model validation and parametric analysis

(4) WF model test

(5) Mechanistic WF evaporation modeling

(6) Numerical model validation and parametric analysis

(7) Application of THM coupled model in pavement

Hence, both experiments and numerical simulations are conducted in this study. The 1-D frost heave tests and WF model tests are carried out. The coupled THM model and evaporation model are proposed and verified by comparing the simulation results with the experimental results. In the freezing process, permeability changes, water-ice phase changes, as well as water and ice content variations are all calculated. The VG model, mass conservation equation, and Naver's equation are expressed as PDEs and solved by FEM software. With respect to the inhibitory effect of WF on frost heave, a numerical model to reproduce water absorption by WF during the freezing process has been developed, which is based on the evaporation model proposed by Fredlund et al. (2016) , with reference to the simplification of Guo on the water absorption of WF(Guo et al., 2017). In this model, heat transfer, deformation, water migration, phase change, and evaporation of soil during freezing are simulated.

1.4 Organization of Thesis

This dissertation is divided into seven chapters.

Chapter 1: This chapter introduces the background of this study. This chapter also present a brief overview of the disaster caused by frost heave in cold regions pavements, the reasons for frost heave, as well as prevention measures. The objective, purpose, and main technical path are briefly presented. The organization of this dissertation is also outlined.

Chapter 2: Various numerical methods (hydrodynamic model, rigid ice model, segregation potential model, and thermomechanical model) are discussed in this chapter for the calculation of the freezing process in soils. Additionally, the characteristics of the new geotextile (WF) and the current state of research on WF are presented. Furthermore, this chapter summarizes the shortcomings of previous research as well as the innovations of this study.

Chapter 3 A theoretical framework is presented in this chapter. The unsaturated soil freezing model and the WF evaporation model with multi-physical field descriptions are presented respectively. In the freezing model, the governing equations for the temperature, hydro and mechanical fields are presented as well as the coupling relationships for each field. The simplified evaporation model used in this study is also presented.

Chapter 4 This chapter presents a one-dimensional frost heave test. A comparison between the results of the freezing experiments and those calculated from the numerical model is presented to illustrate the reliability and validity of the THM coupled model. Furthermore, the chapter discusses the frost heave under different experimental conditions using the THM coupled model.

Chapter 5 This chapter presents the process of WF model testing and the simplified numerical evaporation model. The validity of the proposed evaporation model has been confirmed by a comparison of the results of temperature, hydrological, and mechanical fields between the model tests and numerical simulations. Additionally, the inhibitory effect of WF on frost heave is also demonstrated. On the basis of this conclusion, the influence of freezing conditions on the inhibition effect of WF on frost heave is discussed.

Chapter 6 The numerical modeling of coupled multi-physical fields is used for predicting the reduction of frost heave in field pavements following the installation of WF.

Chapter 7: This chapter summarizes the findings and conclusions of the previous chapters. Recommendations for further research are offered as well.

Figure 1.4 illustrates the research scheme of this study.

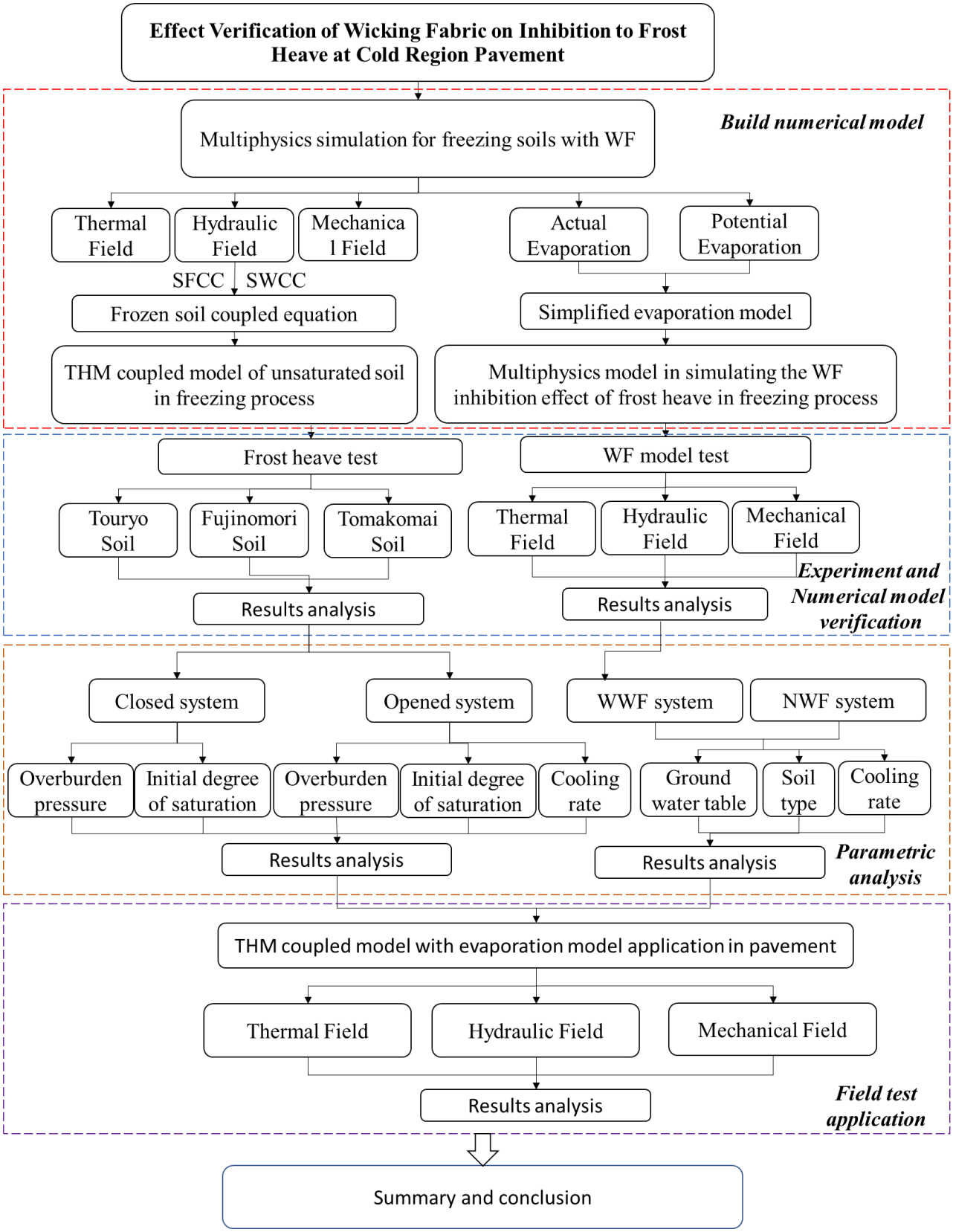

Figure 1.4 Research scheme of this subject.

2 LITERATURE REVIEW

2.1 THM Coupled Models

The freezing process changes the soil temperature, water content, ice content, and volume of the soil as heat propagates through the soil. Additionally, material parameters associated with these properties, such as thermal conductivity and permeability, are also subject to dynamic changes in response to temperature. The change in these variables over time is due to the interaction of different physical fields. Modelling multi-physical field coupling is generally concerned with investigating how the parameters change as they interact with one another in real time. After Everett's capillary-ice model was proposed(first of frost heave theory) (Everett, 1961), Miller developed a rigid ice model(second frost heave theory) based on it(Miller, 1972). Harlan then presented a theoretical model of hydrothermal coupling as applied to the freezing process in soils(Harlan, 1973a). Currently, the segregation potential model is the most widely used semi-empirical model, developed by Konrad based on the experimental study(Konrad and Morgenstern, 1980a, 1981a, 1982a). In addition to these models, there are others based on the mechanical theory of mixtures to describe the behavior of the thermal–moisture-induced deformation of freezing soils, such as thermal models (Duquennoi et al., 1989; Fremond and Mikkola, 1991a; Li et al., 2000, 2002).

2.1.1 Capillary-ice model

Everett has studied moisture migration driving force and has proposed the capillary theory of frost heave (first theory of frost heave)(Everett, 1961). In this model, the capillary force, created by the surface tension and surface energy at the ice-water interface, is the driving force for the moisture migration. As the moisture migrates through the pores, it continuously replenishes the ice lens. In the freezing process, the pore size can have a significant effect on the frost heave. The Young-Laplace equation can be used to defy the capillary force in the following manner,

$$p_i - p_w = \frac{2\sigma_{iw}}{r} \tag{2.1}$$

In this situation, if the ice particle radius r is greater than the effective radius of the soil pore r_p, the ice cannot invade the soil pore. Only if $p_i - p_w$ is large enough so that $r = r_p$, the ice particles can intrude into the soil pores. The critical pressure difference for ice intrusion into soil pores T_p can therefore be expressed as follows,

$$T_p = T_0\left(1 - \frac{2\sigma_{iw}}{L_f p_l r_p}\right) \tag{2.2}$$

Studies have shown that the maximum frost heave pressure in soil samples can be well predicted by T_p, which is determined by the finest 10% of the soil particles(Gaskin, and Sutherland, 1973). As suggested by Peppin and Style, further experiments to observe particle structure and distribution on the surface of the ice crystal could provide additional insight into this issue. Peppin and Style discussed the viscosity resistance of an unfrozen water film and recommended the Clapeyron equation with a dynamic term be used to describe the water pressure at the base of the ice crystals. Due to the fact that the addition of a dynamic term would provide a more accurate value for the calculated water flow rate(Peppin and Style, 2013). Further, Martin(1959) pointed out that a supercooled zone exists below the ice crystal, where the ice particles grow in cracks and macropores. As soon as the ice pressure reaches a critical value (that is, when it exceeds the soil tensile strength and the overburden pressure).

2.1.2 Rigid ice model

The ice pressure in this model does not need to be zero. In the 1980s, O'Neill(1985) proposed a rigid ice model based on Miller's frozen fringe theory(Miller, 1972). This model divided the soil column into three parts: the frozen zone, the frozen fringe, and the unfrozen zone. There is an area between the freezing front and the base of the warmest ice lens known as the frozen fringe, where ice and water coexist and physical processes such as phase change and water migration occur. It is assumed that ice and water pressures satisfy the Clapeyron equation, and that moisture migration follows Darcy's Law. Neutral pressure is used in this model to determine whether an ice lens will form within the frozen fringe, as it is viewed as a rigid unit together with the ice particles underneath it, moving through the soil at the same rate. Based on the analogy between the unfrozen unsaturated soil and the saturated frozen soil, the mass and energy conservation equations for the rigid ice model during one-dimensional freezing are,

$$(\rho_i - \rho_w)\frac{\partial \theta_i}{\partial t} - \frac{\partial}{\partial x}\left(\frac{k}{g}\left(\frac{\partial p_w}{\partial x} - \rho_w g\right) - \rho_i V_i \theta_i\right) = 0 \tag{2.3}$$

$$\sum(\rho C\theta)_n \frac{\partial T}{\partial t} - \frac{\partial}{\partial x}\left(\lambda \frac{\partial T}{\partial x}\right) - \rho_i L_f \left(\frac{\partial \theta_i}{\partial T} + V_i \frac{\partial \theta_i}{\partial x}\right) = 0 \tag{2.4}$$

The rigid ice model describes the mechanism of formation of an ice lenticular body. It is believed that the soil skeleton breaks at the point where the ice is generated, and the overburden pressures are balanced by a neutral pressure (equivalent pore pressure). This means that when the neutral pressure is greater than the ice water pressure, ice formation is possible. The Neutral pressure can be expressed as follows,

$$p_{or} = \chi_{or} p_w (1 - \chi_{or}) p_i \tag{2.5}$$

Although the rigid ice model considers mass and heat transfer phenomena within the frozen fringe and is able to describe the generation of discontinuous ice lenses within the soil by establishing a criterion for the formation of ice lenses, its development is somewhat hampered by the presence of too many parameters in the model(Lu et al., 2017).

2.1.3 Hydrodynamic model

Harlan successfully applied Darcy's Law to the coupled heat transfer analysis of partially frozen porous media by analogy with water migration in unsaturated soils using a fully implicit finite-difference format and proposed the famous 'Hydrodynamic Model' in 1973. The migration of water in this model is driven by the gradient of soil water potential. In addition, the model takes into account latent heat and moisture flow as components of heat transfer(Harlan, 1973a). The mass and energy conservation equations for this model are expressed as,

$$\rho_l \frac{\partial \theta_l}{\partial t} + \rho_i \frac{\partial \theta_i}{\partial t} = \rho_l \frac{\partial}{\partial z}\left(k \frac{\partial H}{\partial z}\right) \tag{2.6}$$

$$C \frac{\partial T}{\partial t} + \rho_l c_l \frac{\partial (v_l T)}{\partial z} = \rho_l \frac{\partial}{\partial z}\left(\lambda \frac{\partial T}{\partial z}\right) + L_f \rho_i \frac{\partial \theta_i}{\partial t} \tag{2.7}$$

The majority of existing hydrodynamic models are TH coupled models; now there is a trend in the geotechnical community to construct a THM model by importing the TH framework(Nishimura et al., 2009; Thomas et al., 2009). Mu et al.(1987) proposed a hydro-thermal-mechanical coupled model for saturated frozen soil based on the Harlan model. A creep constitutive equation based on the increment was developed considering the relationship between soil porosity and frost heave strain. Instead of combining the SWCC and Clapeyron equations, Guymon and Luthin (1974) estimated ice content through the empirical relationship proposed by Nakano and Brown (1971) . There have been other models developed in a similar manner, which may be considered as modifications of the Harlan model (Taylor and Luthin, 1978; Jame and Norum, 1980; Noborio et al., 1996; Newman and Wilson, 1997; Hansson et al., 2004). A study was conducted by Li et al. on the frost heave failure mechanism of the canal. He developed a hydro-thermal-mechanical numerical model of saturated frozen soil based on the energy, mass balance equation, and momentum equation. A comparison of the temperature field and the deformation field indicates that the model is valid (Li et al., 2015, 2018). Zhang et al. (Zeng et al., 2011b, 2011a)developed a one-dimensional two-phase model that fully accounted for diffusion, advection, and dispersion, as well as the effect of soil pressure gradients on evaporation. Their measurements validated their model. Teng et al. (2016)proposed an analytical model to describe water redistribution during evaporation using the Richards equation, as well as an exponential function to describe the relationship between hydraulic conductivity and water content.

One significant difference between the different models is the choice of independent variables. The independent variables in the Richards model are expressed as either pressure, water content, or a mixture of these variables. Briggs contends that the fluid is linearly related to the gradient of water content (Briggs, 1897), but not to the gradient of pressure. As a result, Dirksen and Miller suggest using the water content as an independent variable to represent the Richards equation in order to gain a more accurate understanding of the hydraulic field(Dirksen and Miller, 1966).

2.1.4 Segregation potential model

Konrad proposed the concept of segregation potential, where the ratio between the moisture migration rate in the frozen fringe and the temperature gradient is defined as the segregation potential SP_0.(Konrad and Morgenstern, 1980, 1981, 1982) Specifically, negative pressure at the ice-water interface combined with the moisture migration resistance caused by low permeability frozen fringe is the driving force for moisture migration. If the overburden pressure is taken into account, the model can be expressed as follows,

$$v_l = (SP_0 \cdot e^{-aP_e}) gradT \tag{2.8}$$

$$\frac{dh}{dt} = 1.09(SP_0 \cdot e^{-aP_e}) gradT + 0.09n\frac{dD}{dT} \tag{2.9}$$

With respect to the segregated ice, Nixon defines the segregation pressure in a manner similar to that used in the rigid ice model. This model proposes a neutral pressure which is comprised of pore ice pressure and pore water pressure. The new ice particles only form when the neutral pressure is greater than the overburden pressure. The Neutral pressure can be expressed in a similar way as it was expressed in the rigid ice model. Besides pressure, suction at the frost front, cooling rate, soil type, and other factors can also affect segregation (Nixon, 1991). Once the segregation potential and other thermodynamic parameters are known, it is possible to calculate the frost heave. The segregation potential can be represented mathematically as follows,

$$SP_0 = \frac{v_w}{\nabla T}$$

As long as the temperature gradient at the freezing front is known, the segregation potential model shows excellent performance in engineering applications by estimating the segregation potential using in situ frost heave data (Saarelainen, 1992). It is important to note, however, that the segregation potential is independent of soil properties, and when the

temperature gradient is unknown, it is difficult to determine the segregation potential and, consequently, its application is somewhat limited (Li, 2021).

2.1.5 Thermomechanical model

The thermodynamic model was developed first by Duquennoi et al. (1989), and then refined by Fremond (1991). The model establishes the conservation equations of each physical field based on the equations for mass conservation, energy conservation, and momentum conservation, and deduces the constitutive equations of frozen soil through entropy inequality, as well as the introduction of free energy and dissipation potential functions. The model describes the transport of heat and moisture as well as the generation of negative pore pressure. The derivation of the model is rigorous; however, due to its strong theoretical background, its application in engineering is limited.

2.2 WF Properties

2.2.1 WF characteristic

The WF is a woven geotextile composed of polypropylene and nylon fibers. Nylon fibers will enhance lateral drainage, while polypropylene polymers will provide strength to the fabric(Zornberg et al., 2017). Researchers have conducted experiments to better understand the characteristics of WF and the mechanism by which it transports moisture. The figure below illustrates an example of a WF that contains high-tensile polypropylene and nylon fibers.

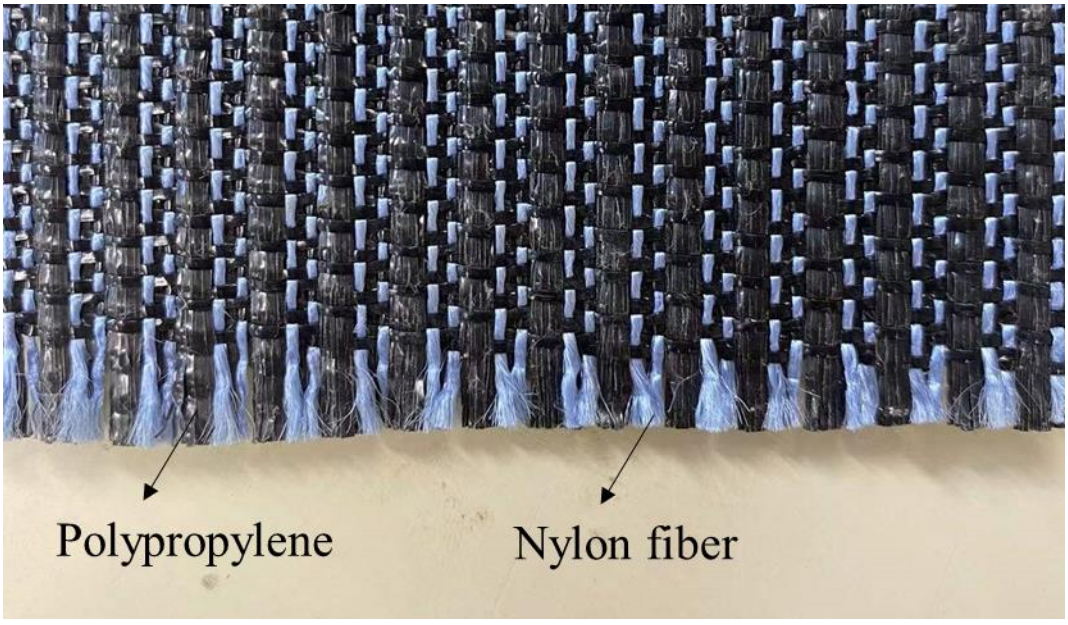

Figure 2.1 Schematic interpretation of THM coupling.

Moisture may flow out of WFs via capillary tubes, and these capillary tubes generate capillary forces, which facilitate the absorption of moisture from the soil around them. Unlike conventional geotextiles which have a circular cross-section, WF has an irregular cross-section consisting of grooves with a diameter of approximately 5-12 um (Figure 2.3). WF fibers are made of nylon, which is both hydrophilic and hygroscopic. In practice, since the WFs are exposed to air at one end, the difference between the relative humidity in the air and the relative humidity in the soil is what drives the flow of water in the capillaries. When the air is dry outside, the geotextile can continually transport moisture out of the soil. In this instance, the grooves act as capillaries within the fibers, which remove water from the geotextile through the grooves aligned along the fiber's longitudinal axis.

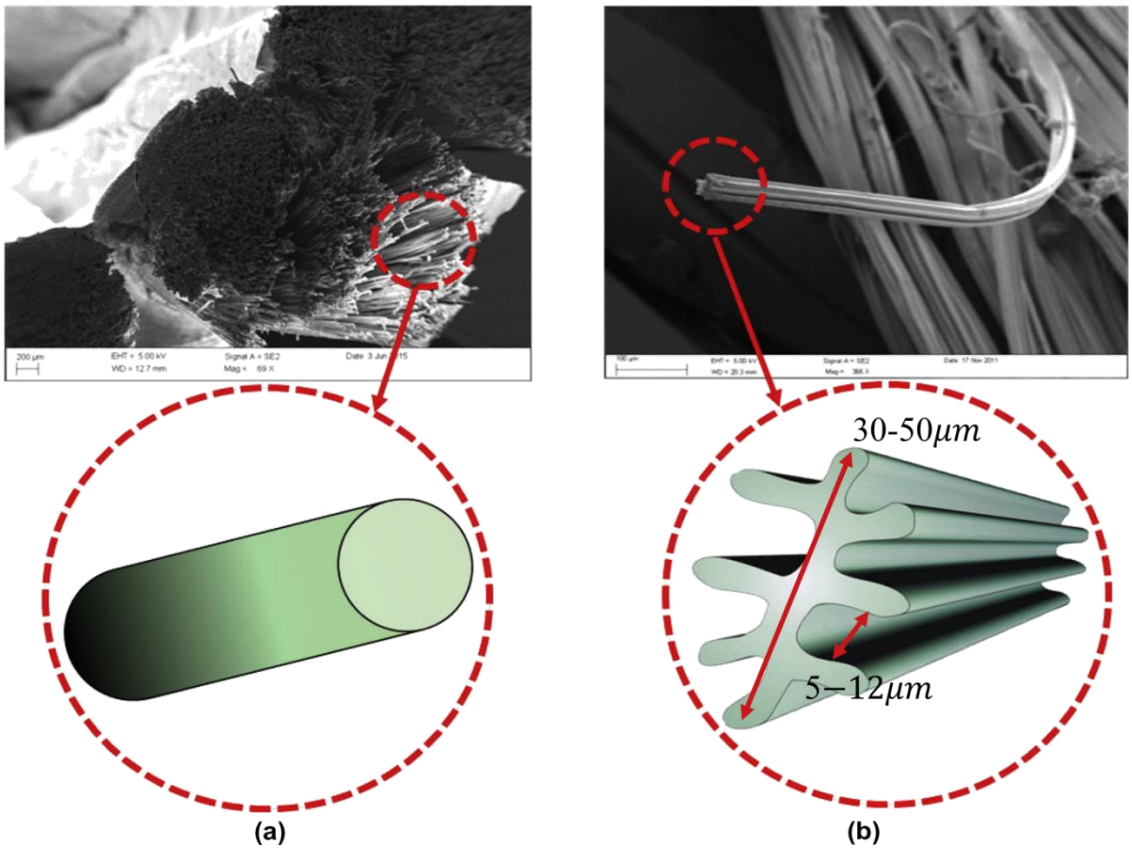

Figure 2.2 Cross-section of fibers in geotextiles, (a) traditional geotextile; (b) wicking fabric(modified from Zornberg et al. (2017) and Guo et al., (2022)).

Bahador et al.(2013) investigated the effect of WF on moisture distribution and plastic deformation in paved and unpaved sections using numerical simulations. Han et al. (2014) analyzed the microstructure of WF and presented an explanation for the water absorption working mechanism of this material. An experiment conducted by Guo et al.(2019) indicated that the capillary of the WF could effectively drain water from the soil column up to a considerable distance through the WF.

Lin et al.(2019) performed a comprehensive laboratory test to characterize the property of the WF and soil–WF interactions, as is shown in Figure 2.3. He proposed an inter-yarn air entry value (AEV) and an inner-yarn AEV, which correspond to the suction generated by the pores between fiber bundles and the deep grooves of individual fibers, respectively. The results showed that the WF can effectively drain water until the suction reaches the inner-yarn air entry value. Furthermore, several researchers have attempted to simulate the drainage process of WF with numerical tools. For instance, Lin et al. (2019) conducted a numerical simulation to quantify the drainage ability of a soil–WF system, which demonstrated that the soil–WF system can reduce the water content of the pavement by 2% from the optimum value. Yasuoka et al.(2022) performed a numerical simulation and indicated that WF could drain water and inhibit frost heave.

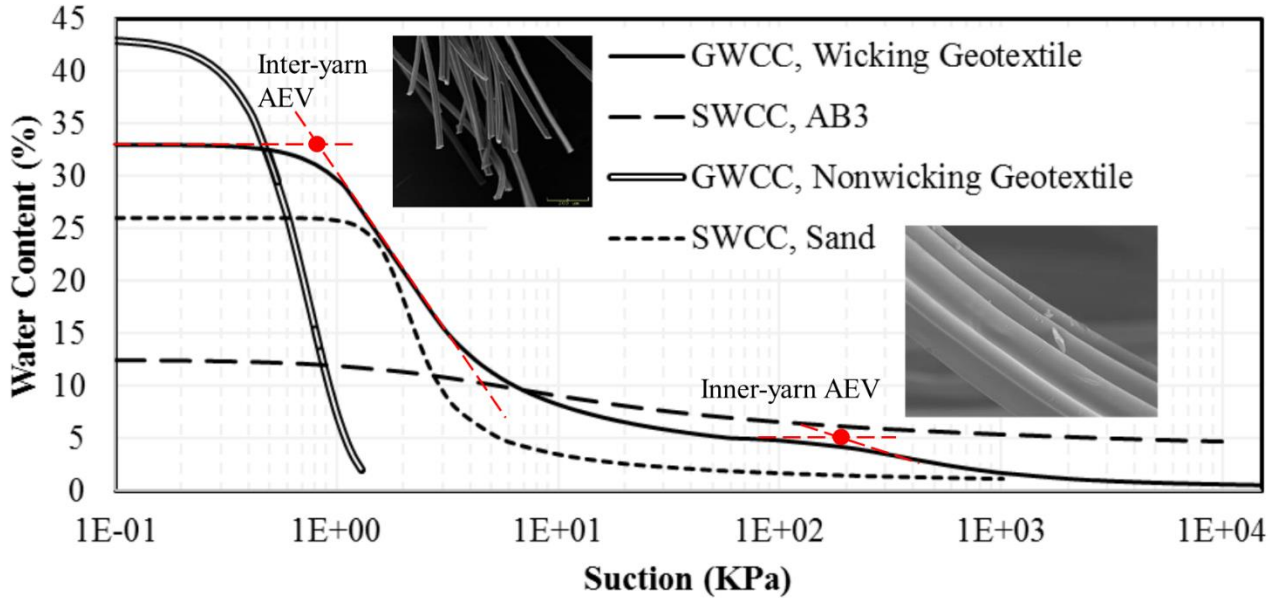

Figure 2.3 WF theoretical moisture storage(adapted from Lin et al. (2019)).

2.2.2 WF application

Since there is a significant difference between the microstructure of WF and conventional geotextiles, there are some differences in their application. The most significant difference between WF and conventional geotextiles is that WF can be used for gravity drainage in saturated soils, as well as horizontal drainage in unsaturated soils by evaporation, while conventional geotextiles can only be used in saturated conditions (Guo et al., 2017). The laboratory tests have demonstrated that WF is effective as a drainage material, the geotextile has been used in various engineering projects to address problems that cannot be solved with traditional construction methods(Azevedo, 2016; Hachem and Ghassan, 2018).

In a test section along the Dalton Highway near Beaver Slide, this unpaved section of road that was damaged by frost heaving and thawing. It was constructed by installing WF for the prevention of frost boils. It has been shown that traditional rehabilitation methods are not sufficient to address the annual recurrence of the condition. Therefore, two layers of WF spaced 18 inches apart were installed above the subgrade, and 3 feet of WF were exposed to the air at the road edge in order to create a suction gradient, which is the primary driving force for drainage(Zhang et al., 2014). An inspection of the road condition at the site of the test section conducted five year after installation indicates that the soil moisture content is much less than the saturated water content, and there is no evidence of frost heave or road damage(Lin et al., 2017).

WF was also successfully applied to a Wisconsin State Trunk Highway to treat severe deformation of the road surface caused by differential settlement and frost heave. The soil consisted of a 9m-deep deposit of saturated silt and peat in this section. Post-construction field reports indicated that the installation of WF and biaxial geogrids over the subgrade ensured a pavement that both performed as expected and was economically advantageous by avoiding the need for soil replacement. (Hachem and Ghassan, 2018).

Although several models have been developed to estimate the effectiveness of WF in draining moisture, limitations in applying the boundary condition of WF remain. Most previous numerical models do not take into account the influence of the surrounding environment on the water absorption process of WF. In general, the water absorption process is simulated by setting a constant pressure boundary at the end of the WF. Indeed, such a simplification might still be able to reproduce the WF absorption process. Nevertheless, it has been demonstrated that the absorption effect of WF can be impacted by ambient conditions (e.g., temperature, relative humidity) (Han and Guo, 2017). It is therefore very important to consider the influence of the environment conditions when simulating the water absorption process of WF.

3 MULTIPHYSICS SIMULATION FOR FREEZING SOILS WITH WF: THEORETICAL FRAMEWORK

This chapter discusses the theoretical framework of a multi-physics hybrid coupled model, which means there are bidirectional coupling process and unidirectional coupling process in the coupled model (Jiang et al., 2014). The coupled model combines Fourier's law for heat transfer, the generalized Richards equation for water migration in unsaturated soils, and mechanical constitutive relationships. Various coupling parameters are defined for transferring information between each physical field. The frost heave effect is described by various relations, such as the similarity of drying and freezing processes and the Clapeyron equation for phase equilibrium in phase-change processes. Also, this chapter describes the simplified process of water absorption process by WF installed in the soil during freezing and the deficiencies of the simplified model. Specifically, the proposed evaporation model considered the boundary condition which is related to the change in soil water content over time.

3.1 THM Coupled Model

To simulate transient, simultaneous heat and mass flow with phase change in frozen, partially saturated, homogeneous soil, the following assumptions are made:

(1) Darcy's law is applicable to moisture movement in both saturated and unsaturated conditions.

(2) The porous media is a non-deformable and isotropic material.

(3) The impact of the mechanical (M) field on thermal-hydraulic (TH) fields is ignored.

A schematic depicting the interaction between various physics fields in the proposed model is shown in Figure 3.1. The ignored coupled relationship between the mechanical field and thermal-hydraulic fields is illustrated as dash lines.)

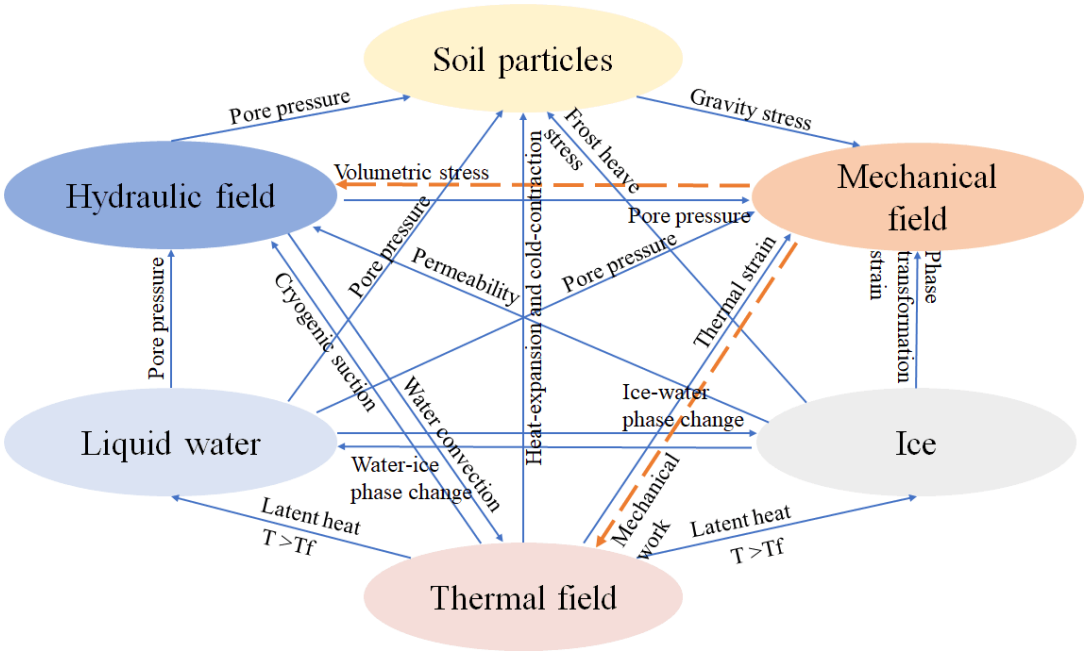

Figure 3.1 Schematic interpretation of THM coupling.

3.1.1 Governing equation of thermal field

Based on the energy conservation principle, the partial differential equation (PDE) to describe the transient heat flow in the freezing process can be written as (De Vries, 1958; Nassar and Horton, 1989, 1992),

$$C_v \frac{\partial T}{\partial t} = \nabla(\lambda \nabla T) + L_f \rho_i \frac{\partial \theta_i}{\partial t} \tag{3.1}$$

where C_v is the volumetric heat capacity of the soil; T is temperature; λ is the thermal conductivity of the soil; L_f is the latent heat of fusion; ρ_i is the density of ice; and θ_i is the volumetric ice content.

The thermal conductivity of the frozen and unfrozen soil can be generally expressed as follows (Côté and Konrad, 2005),

$$\lambda = (\lambda_{sat} - \lambda_{dry})\lambda_r + \lambda_{dry} \tag{3.2}$$

where, λ_{sat} is the thermal conductivity of saturated soil, λ_{dry} is the thermal conductivity of the dry soil, λ_r is the normalized thermal conductivity, θ_u is the volumetric unfrozen water content.

The thermal conductivity of saturated soil and normalized thermal conductivity can be calculated by Equations (3.3) and (3.4) follows (Côté and Konrad, 2005),

$$\lambda_{sat} \begin{cases} \lambda_s^{1-n} \lambda_i^{n-\theta_u} \lambda_u^{\theta_u} & T < T_f \\ \lambda_s^{1-n} \lambda_u^{\theta_u} & T \geq T_f \end{cases} \tag{3.3}$$

$$\lambda_{dry} = \chi \times 10^{-\eta n} \tag{3.4}$$

$$\lambda_r = \frac{K_0 S}{1+(K_0-1)S} \tag{3.5}$$

where K_0 is an empirical parameter depending on soil type.

The volumetric heat capacity can be calculated using the weighted algorithm as,

$$C_v = C_s(1-n) + C_u\theta_u + C_i\theta_i \tag{3.6}$$

To reduce the nonlinearity, the concept of apparent heat capacity can be used to merge the heat capacity with the second term of Equation (3.1) on the right hand, which accounts for the enthalpy change due to phase change (Anderson et al., 1973; Harlan, 1973),

$$C_a = C_v - L_f\rho_i\frac{d\theta_i}{dT} = C_v + \frac{{L_f}^2\rho_i}{gT}\frac{d\theta}{dh} \tag{3.7}$$

Thus, the volumetric ice content can be expressed as,

$$\frac{d\theta_i}{dT} = -\frac{L_f}{gT}\frac{d\theta}{dh} \tag{3.8}$$

And the total volumetric water content is the sum of the volumetric ice content and the volumetric unfrozen water content:

$$\theta = \theta_i + \theta_u \tag{3.9}$$

By using the generalized Clapeyron equation, the apparent volumetric heat capacity can be redefined by the hydraulic capacity C_H according to Hansson et al (2004). The hydraulic capacity is defined as the derivative of water content concerning the pressure head, which can be expressed as,

$$C_H = \frac{d\theta}{dh} = \begin{cases} \frac{\alpha_{vg}(n_{vg}-1)(\alpha_{vg}h)^{n_{vg}-1}}{\left((\alpha_{vg}h)^{n_{vg}}+1\right)^{\frac{2n_{vg}-1}{n_{vg}}}} & h < h_s \\ 0 & h \geq h_s \end{cases} \tag{3.10}$$

Therefore, Equation (3.6) can be rewritten as,

$$C_a = C_v + \frac{{L_f}^2\rho_i}{gT}C_H \tag{3.11}$$

Unfrozen water can also co-exist with ice in unsaturated soil during freezing. At this time, soil water potential remains in equilibrium with the vapor pressure over pure ice(Flerchinger and Saxton, 1989). Based on the thermodynamic relationship and the Clausius-Clapeyron equation, Dall'Amico (2011) proposed an equation to describe the relationship

between soil matric potential and final freezing temperature in the freezing process. When $T \geq T_f$, the soil is unfrozen; when $T < T_f$, the soil is under freezing conditions.

$$T_f = T_m + \frac{gT_m}{L_f} h \tag{3.12}$$

3.1.2 Governing equation of hydraulic field

Richard's equation was adopted to describe the flow in the partially saturated porous medium. In this study, a mixed form of Richard's equation (Noborio et al., 1996; Fayer, 2000) was used, which can be written as,

$$\frac{\partial \theta_u}{\partial t} + \frac{\rho_i}{\rho_u} \frac{\partial \theta_i}{\partial t} = \nabla(K_r \nabla h + K_r \boldsymbol{i}) \tag{3.13}$$

For unfrozen unsaturated soil, the hydraulic conductivity can be expressed by using relative hydraulic conductivity, K_{wr}, which is a power function of the effective saturation S_e, per the Mualem-van Genuchten model,

$$K_r = K_{wr} K_s = K_s S_e^{\frac{1}{2}} \left[1 - \left(1 - S_e^{\frac{\lambda_{vg}}{\lambda_{vg-1}}} \right)^{\frac{\lambda_{vg-1}}{\lambda_{vg}}} \right]^2 \tag{3.14}$$

where

$$S_e = \frac{\theta - \theta_r}{\theta_s - \theta_r} = \left[1 + \left(\alpha_{vg} h \right)^{\lambda_{vg}} \right]^{\frac{1-\lambda_{vg}}{\lambda_{vg}}} \tag{3.15}$$

A characteristic of frozen soil is that its permeability decreases as ice saturation increases. Considering ice content, Jame and Norum (Jame and Norum, 1972) suggested an impedance factor approach to describe the permeability in the freezing process,

$$K_r = K_s I \tag{3.16}$$

Taylor and Luthin (1978)compared the simulation result with the data of Jame (1977), proposed and validated a relationship between the volumetric ice content and impedance factor, I, as follows.

$$I = 10^{-E_i \theta_i} \tag{3.17}$$

The most common way to determine E_i is proposed by Shoop and Bigl (1997):

$$E_i = \frac{5}{4} (K_s - 3)^2 + 6 \tag{3.18}$$

Similarly, for unsaturated frozen soil, the permeability can be expressed as,

$$K_r = IK_s S_e^{\frac{1}{2}} \left[1 - \left(1 - S_e^{\frac{\lambda_{vg}}{\lambda_{vg-1}}} \right)^{\frac{\lambda_{vg-1}}{\lambda_{vg}}} \right]^2 \tag{3.19}$$

Suppose h_s is the saturated matric potential (i.e., $h_s = 0$). Equations (21) and (23) are used to describe unsaturated soil permeability in the freezing process. Thus, the formulation of the permeability K_r under freezing conditions for saturated and unsaturated soils becomes:

$$K_r = \begin{cases} h < h_s & \begin{cases} K_s S_e^{\frac{1}{2}} \left(1 - \left(1 - (S_e)^{\frac{\lambda_{vg}}{\lambda_{vg-1}}} \right)^{\frac{\lambda_{vg-1}}{\lambda_{vg}}} \right)^2 & T \geq T_f \\ IK_s S_e^{\frac{1}{2}} \left(1 - \left(1 - (S_e)^{\frac{\lambda_{vg}}{\lambda_{vg-1}}} \right)^{\frac{\lambda_{vg-1}}{\lambda_{vg}}} \right)^2 & T < T_f \end{cases} \\ h \geq h_s & \begin{cases} IK_s & T < T_f \\ K_s & T \geq T_f \end{cases} \end{cases} \tag{3.20}$$

In order to model the water migration in the unsaturated soil and better understand the various potential energy of unsaturated flow, Scanlon has organized and explained the relevant concepts, as shown in Table 3.1(Scanlon et al., 1997).

Table 3.1 Various types of potential energy in unsaturated flow (adapted from Scanlon et al., 1997)

Potential energy type	Description
Gravitational potential	Elevation above reference level (e.g. groundwater table)
Matric potential	Capillary and adsorptive forces associated with the soil matrix
Suction/tension	Negative matric potential
Osmic(solute) potential	Variations in potential energy associated with solute concentration
Water potential	Matric and osmotic potential
Pneumatic potential	Associated with variations in air pressure
Hydraulic head	Matric and gravitational potential head
Pressure head	Matric potential head

3.1.3 Governing equation of mechanical field

According to Liu (2018), the linear elastic model is adequate for accurately simulating the frost heave test of unsaturated soil. Therefore, to control the complexity of the model, such a model was used in this study to describe deformation during

the freezing process. Navier's equation, which incorporates the equation of motion, strain, displacement correlation, and the constitutive relationship, serves as the governing equation in the mechanical field (Liu et al., 2020),

$$\nabla(C\nabla u) + F = 0 \tag{3.21}$$

where C is a fourth-order tensor of material stiffness; u is the displacement vector; F is the body force vector. And the strain-displacement relationship can be expressed as follows,

$$\varepsilon = \frac{1}{2}[\nabla u + (\nabla u)^T] \tag{3.22}$$

where ε is the infinitesimal strain tensor.

The simplified linear elastic constitutive equation can be derived as,

$$\sigma = D\varepsilon_{el} + \sigma_0 = D\left(\varepsilon - \varepsilon_{th} - \varepsilon_{tr} - \varepsilon_0 - \varepsilon_{hp}\right) + \sigma_0 \tag{3.23}$$

$$D = \frac{E(1-\nu)}{(1+\nu)(1-2\nu)}\begin{bmatrix} 1 & \frac{\nu}{(1-\nu)} & 0 \\ \frac{\nu}{(1-\nu)} & 1 & 0 \\ 0 & 0 & \frac{1-2\nu}{2(1-\nu)} \end{bmatrix} \tag{3.24}$$

where σ is Cauchy stress tensor; D is the stiffness matrix of soil skeleton; σ_0 is the initial stress vector; ε_{el} , ε_{th}, ε_{tr}, and ε_{hp} are the elastic strain, strain caused by thermal expansion, strain caused by water phase change, and strain caused by matric potential, respectively; and ε_0 is the initial strain. ε_{th}, ε_{tr}, and ε_{hp} can be separately expressed as follows (Liu and Yu, 2011),

$$\varepsilon_{th} = [\alpha(T - T_m) \quad \alpha(T - T_m) \quad 0]^T \tag{3.25}$$

$$\varepsilon_{tr} = [1.09(\theta_u + 0.9\theta_i - n) \quad 1.09(\theta_u + 0.9\theta_i - n) \quad 0]^T \tag{3.26}$$

$$\varepsilon_{hp} = [h/H \quad h/H \quad 0]^T \tag{3.27}$$

3.1.4 SWCC and SFCC

Williams and Smith (1989) describe the Soil-Water Characteristic Curve (SWCC) as the relationship between water content (volumetric, gravimetric, or saturation) and the pore water pressure (or suction). Generally, this curve is used to analyze the drying/wetting processes of soil and show the characteristics of various soil types. It is also widely used for analysing freezing processes in porous materials because of the similarity between drying and freezing processes (Koopmans and Miller, 1966). Over the past few decades, numerous empirical equations have been proposed for SWCCs, Liu have are summarized the frequently-used equations for soil water characteristic curves (SWCCs) in Table 3.2 (Brooks et al., 1964; van Genuchten, 1980; Fredlund et al., 1994; Fayer, 2000; Vogel et al., 2000; Liu et al., 2012).

Table 3.2 Various types of potential energy in unsaturated flow (adapted from Liu et al., 2012)

Reference	Equation
Gardner, 1958	$S_{re} = \frac{1}{1 + a\psi^n}$
Brooks and Corey, 1964	$S_{re} = \left(\frac{\psi_e}{\psi}\right)^{\lambda}$
Haverkamp et al., 1977	$S_{re} = \frac{a}{a + \psi^b}$
van Genuchten, 1980	$S_{re} = \left[\frac{1}{1 + (\alpha\psi)^n}\right]^m$
Williams et al., 1983	$\theta = exp\left[\frac{1}{b}(In\psi - a)\right]$
Bond et al., 1984	$\theta = a + blog(\psi) + clog^2(\psi) + dlog^4(\psi) + elog^4(\psi)$
Mckee and Bumb, 1984	$S_{re} = exp\left[-{(\psi - a)}/{b}\right]$
Bumb, 1987	$S_{re} = \frac{1}{1 + e^{{(\psi - a)}/{b}}}$
Fredlund and Xing, 1994	$\theta = \theta_s \left[\frac{1}{In\left(e + \left({\psi}/{a}\right)^n\right)}\right]^m$

Where *a,b,m,n*, are empirical constants.

When the soil is saturated, the unfrozen volumetric water content can be expressed as the saturated volumetric water content. For the unsaturated condition, the hydraulic properties of unsaturated soil may be used to describe the volumetric water content. In this study, the Van Genuchten- Mualem Equation (Mualem, 1976)with independent parameters α_{vg} and n_{vg} are used.

$$\theta_u = \begin{cases} (\theta_s - \theta_r)\left(\frac{1}{(|h|\alpha_{vg})^{nvg}+1}\right)^{\frac{nvg-1}{nvg}} + \theta_r & h < h_s \\ \theta_s & h \geq h_s \end{cases} \quad (3.28)$$

Meanwhile, a similar soil freezing characteristic curve (SFCC) is used to describe the relationship between temperature and suction in the freezing process. Assuming that the ice pressure is zero, Hansson (2004) proposed a generalized Clapeyron equation based on the thermal dynamic equilibrium theory. The Clapeyron equation can be used to convert sub-freezing temperature to suction. Based on this theory, the SFCC can be derived from SWCC by relating suction with

sub-freezing temperature. When the temperature is under the freezing point, the following equation can be used to evaluate the soil matric potential:

$$h = \frac{L_f}{g} In \frac{T}{T_f} \tag{3.29}$$

3.2 WF Evaporation Model

In this section, we firstly propose a coupled hydromechanical framework of FEM and MPM to simulate runoff, seepage, and large deformation of soil. In the FEM-MPM hybrid coupled model, surface flow and subsurface flow are bidirectional coupled through infiltration and exfiltration by using COMSOL Multiphysics software (COMSOL Multiphysics, 2018). The subsurface flow model and soil mechanics model are unidirectional coupled in two ways: (1) the mass of each material point is replaced by the mass of soil and water mixture, and (2) the effect of variable matric suction on the shear strength of each material point is considered into cohesion by using LSS method. Then, the governing equations used in the hybrid coupled model are presented.

3.2.1 Simplification of WF drainage process

The wetting process describes the movement of absorbed water in the geotextile. Geotextiles can remove water through gravity drainage and evaporation during a wet period. In saturated soils, gravity drainage occurs if sufficient water is supplied and the rate of water flow onto an exposed geotextile is greater than the evaporation rate. WF and conventional geotextiles can both provide gravity drainage. Besides serving as a gravity drainage device, WF can remove water in unsaturated soils by sucking it into the fibers. The water is transported to an exposed portion of the WF and evaporates into the air. In this study, the water removed by WF is described as an evaporating process.

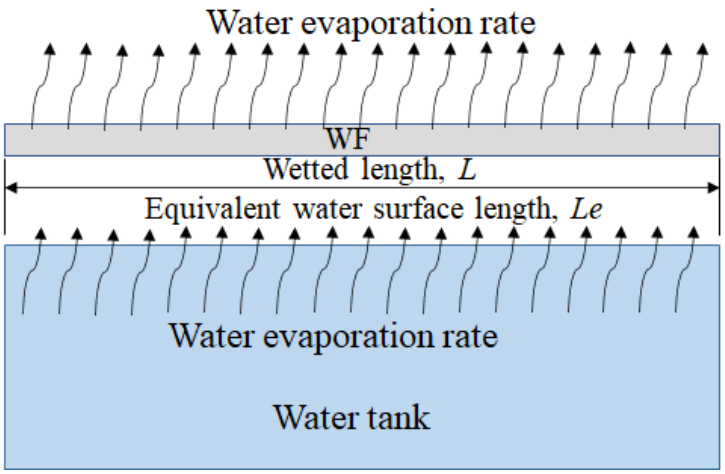

Figure 3.2 Schematic of water transport and evaporation in wicking geotextile (adapted from Guo et, al. 2017).

In this study, the water removed by WF is described as an evaporating process, as illustrated in Figure 2a. The model test simulation was simplified by using the following assumption for the evaporation process of WF: water evaporation from WF exposed to air (X) equals the water absorbed from WF buried in the soil (Y), as shown in Figure 2b. Accordingly, the numerical model calculated the evaporation of WF exposed to air and applied it to the WF buried in the soil as a line source. However, this simplification is limited. As the model assumes that the rate of evaporation from the WF is the same as the rate of water removal from the soil, this assumption only holds true when the area of WF exposed to air (*La*) is not less than the area buried in the soil (*Ls*). Therefore, when the area of the WF exposed to air is smaller than that buried in the soil, the evaporation amount calculated by this method will be higher than reality. Accordingly, the WF appears to be more effective at suppressing frost heave in the calculation than it is. In this case, the applied line source should be equal to the AE multiplied by the ratio of the exposed length and the buried length.

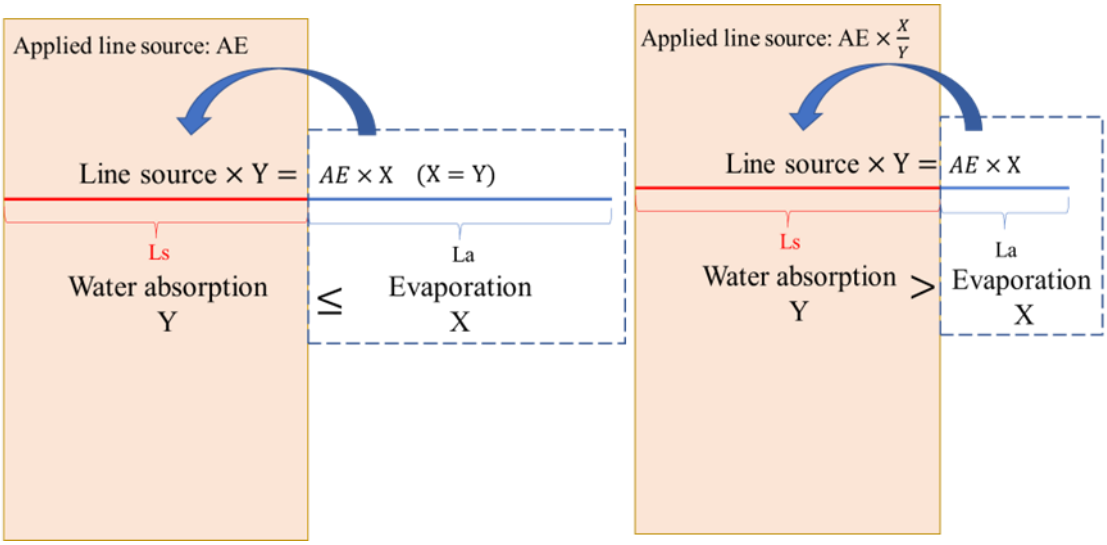

Figure 3.2 Simplified schematic of the evaporation model.

3.2.2 WF evaporation model

Referring to Fredlund et al.(2016), the actual evaporation rate can be expressed in the form of the thermodynamic equilibrium relationship between relative humidity and total suction,

$$AE = PE \times \exp^{\left(\frac{-\psi g w_v}{\zeta(1-RH\gamma_w)RT}\right)} \tag{3.30}$$

Where AE is the actual evaporation, PE is the potential evaporation. ψ is the matric suction ($\psi = -\rho_u g h$); ζ is a dimensional empirical parameter with a suggested value of 0.7; g is the gravity acceleration (m/s2), w_v is the molecular

mass of water, 0.018 kg/mol; RH is the relative humidity of overlaying air; γ_w is the unit mass of water, 9.807 kN/m3; R is the universal gas constant, 8.314 J/(mol·K)

The widely used equation to calculate the potential evaporation rate was proposed by Penman (1948), which is written as,

$$PE = \frac{\Gamma Q_n + \eta_e E_a}{\Gamma + \eta_e} \tag{3.31}$$

Where Γ stands for the slope of the saturation vapor pressure versus the temperature curve at the mean temperature of the air; η_e is psychrometric constant, 66.8 Pa/°C; Q_n is the heat budget; and E_a is the aerodynamic evaporative term, which can be expressed as,

$$E_a = 3.5(1 + 0.146U_a)(e_{a0} - e_a) \tag{3.32}$$

Where e_{a0} is the saturation vapor pressure of the mean air temperature, e_a is the actual vapor pressure of the air; U_a is the wind speed; The heat budget is caused by the net radiant energy available at the surface. The heat budget and the wind speed are neglected in the freezing process, so Eq. 23 can be simplified as,

$$PE = \frac{\eta_e 3.5(e_{a0} - e_a)}{\Gamma + \eta_e} \tag{3.33}$$

Tetens (1930) estimated Γ based on the air temperature as follows,

$$\Gamma = \frac{4098 e_{a0}}{(273.15 + T_a)^2} \tag{3.34}$$

and

$$e_{a0} = \frac{e^0(T_{amax}) + e^0(T_{amin})}{2} \tag{3.35}$$

$$e_a = \frac{e^0(T_{amax})\frac{RH_{amax}}{100} + e^0(T_{amin})\frac{RH_{amin}}{100}}{2} \tag{3.36}$$

$$e^0(T_a) = 0.6108\exp\left(\frac{17.27T_a}{T_a + 273.15}\right) \tag{3.37}$$

Where $e^0(T_a)$ is the saturation vapor pressure of the air at the air temperature T_a; T_{amax} and T_{amin} are the maximum and minimum temperature of the air, separately; RH_{amax} and RH_{amin} are the maximum and minimum relative humidity of the air, separately.

This study simulates the absorption of water by WF as an evaporation process and models this process numerically. In contrast to the evaporation process occurring under saturated conditions with sufficient water supply, the unsaturated soil evaporation model is coupled with the evaporation process of the WF. In addition, this study presents a numerical simulation of the WF evaporation process under unsaturated conditions. The model includes both the evaporation and freezing processes. Thus, the proposed model can be used to simulate the water uptake of WF in the unsaturated soil during freezing.

3.3 Summary

In this chapter, the specific coupling variables in the governing equations are refined using the macroscopic mass, momentum, and energy conservation equations derived from THM. In this study, a coupled multi-physical field model is proposed that describes seepage, heat transfer, and deformation of unsaturated soils during freezing by introducing basic assumptions. The unfrozen water content is estimated by considering the distribution of unfrozen water within the frozen void and unfrozen void. The parameters have clear physical significance. Additionally, the model can be derived continuously near the freezing point. Finally, the established evaporation model considers the effects of temperature and water content changes on the water absorption effect of WF during freezing, which allows a more accurate prediction of the WF absorption effect.

4 VALIDATION OF FROST HEAVE TEST

In Chapter 3, the authors present a THM coupling model of the unsaturated soil freezing process. However, the validity and applicability of the model are not examined yet. This chapter shows three soil samples widely distributed in Hokkaido. These soils are used to conduct the 1-D frost heave tests to verify the frost heave susceptibility of soils and the effect of different experimental conditions on frost heave. The numerical models are also established based on the theoretical framework proposed in Chapter 3. The experimental data from the 1-D frost heave tests are used to verify the validity of the THM coupled model. Meanwhile, the coupled physical properties variation of soil during freezing, including suction, permeability and water content, are calculated based on the developed model.

4.1 One-Dimensional Frost Heave Test

The one dimensional frost heave test is generally used to determine the value of frost heave ratio and frost susceptibility of the soil. In this study, Tomakomai soil, Touryo soil and Fujinomori soil are used to conduct this frost heave test.

.

4.1.1 Experiment setup

An illustration of the frost heave testing apparatus is shown in Figure 4.1. The apparatus has two thermostatic baths, which, by circulating antifreeze liquid at a specific temperature, control the temperature of the cap and pedestal independently. A platinum resistance thermometer sensor was used to measure the temperatures in the apparatus. In this way, any temperature difference between the cap and the pedestal might be set arbitrarily. To further control the temperature of the specimen, cold water at 2 degrees Celsius was circulated between the inner cell and the pressure cell, and thermally insulating materials were placed between the frost-heave cell and the inner cell. A pneumatic actuator was used to apply overburden pressure in the range of 0 to 130 kPa. Three sheath-type thermocouples were inserted into the specimen through the frost-heave cell to examine the thermal distribution. At heights of 0.75 cm, 2.18 cm, and 3.58 cm from the specimen bottom, these thermocouples were located. In addition, the inflow and outflow of water were determined using a differential transducer connected to a double tube burette.

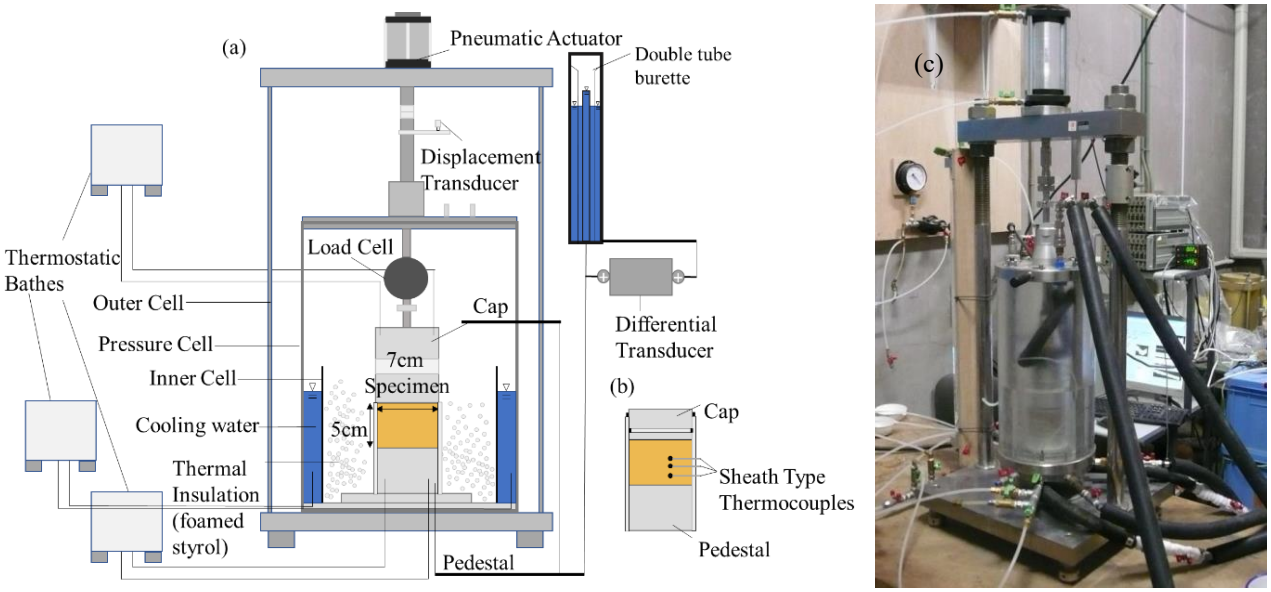

Figure 4.1 Frost heave test apparatus (a) a general view; (b) temperature measurement of specimen; (c) picture of the test set up.

4.1.2 Soil column preparation

The dimensions of the mold with diameter of 7 cm and a height of 5 cm. Assemble the mold and place the soil sample into it in three times, then ram the soil sequentially. For each tamping, the plastic sheet should be placed over the soil sample to avoid the soil staining the bottom of the heavy hammer. Every time the soil sample was tamped, scraped the upper surface of the soil in order to create an uneven surface and ensure a good bite and connection with the next layer of soil. A soil sample can then be removed carefully from the mold after it has been disassembled.

4.1.3 Test procedure

Place the permeable stone on the base, place the filter paper soaked with distilled water on the permeable stone, and place the soil specimen on to the lower cooling plate. Place the filter paper on the top surface of the specimen and bring the upper plate gently into contact with specimen. Temperature sensors are inserted into the soil sample through small holes reserved for monitoring the temperature at different heights in the soil sample over time during the freezing process. It is recommended that the pipe which circulates the cooling brine be positioned horizontally at the same height as the instrument to ensure that the brine can flow freely. The screws between the mold and the base should be tightened. Set the external mold on the base and insert insulation material (expanded polystyrene) between the frozen mold and the outer mold. In order to control the water supply system during the freezing process, the inlet and outlet pipes are connected at the bottom of the instrument following the installation of the insulation layer. Afterwards, the outermost mold should be

installed. Having adjust the upper-pressure gauge so that it is integrated with the lower part, install the thermal sensor at the top surface to monitor the temperature variation at the boundary. Adjust the pneumatic actuator to connect the lower part of the experimental instrument to the upper part. Then, set the pressure of the upper pump and lower pump to zero as initial state. Finally, assembling the displacement sensor.

4.2 Verification of THM coupled model

The simulations of frost heave tests with three types of frost susceptible soils were performed under various test conditions, including overburden pressure (σ_{ob}), water supply system (closed-system/opened-system), cooling rate (U), and initial saturation (S_0). The size of the sample, boundary conditions, and the mesh of the two-dimensional model under a plane strain condition is shown in Figure 4.2. The boundary conditions of each field follow the actual test condition. Note that the hydraulic boundary on the top surface depends on the water supply system (opened-system or closed-system) used in each experiment. COMSOL software, a commercial multiphysics simulation platform, was used to solve the presented coupled model. In which, the closed systems are those within which existing water cannot escape or additional water cannot be absorbed (Taber, 1930). And the open system is one that can absorb water from the outside during the freezing process.

4.2.1 Model configuration

The simulations of frost heave tests with three types of frost susceptible soils were performed under various test conditions, including overburden pressure (σ_{ob}), water supply system (closed-system/opened-system), cooling rate (U), and initial saturation (S_0). The size of the sample, boundary conditions, and the mesh of the two-dimensional model under a plane strain condition is shown in Figure 4.2. The boundary conditions of each field follow the actual test condition. Note that the hydraulic boundary on the top surface depends on the water supply system (opened-system or closed-system) used in each experiment. COMSOL software, a commercial multiphysics simulation platform, was used to solve the presented coupled model. The model developed herein was applied to a typical THM freezing process, and the simulation results were compared against the experimental results from Tokoro *et al.* (2016) and Ishikawa et al. (2015).

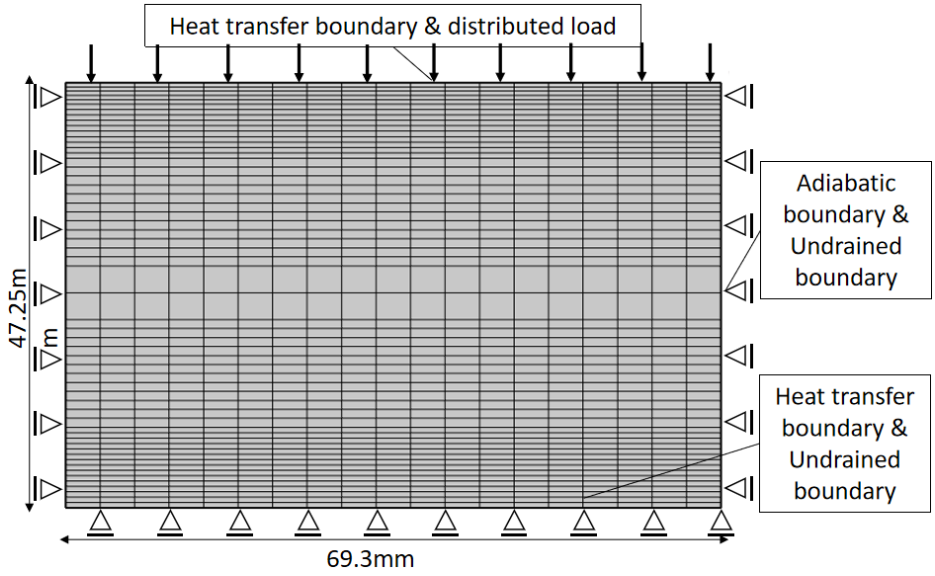

Figure 4.2 Frost heave test apparatus (a) a general view; (b) temperature measurement of specimen; (c) picture of the test set up.

For the thermal field, the soil was frozen from the bottom up. Thus, the adiabatic boundary was imposed on both lateral sides, a constant thermal boundary was imposed on the top surface, and a constant cooling rate U was imposed on the bottom. For the hydraulic field, the impermeable boundary was imposed on both lateral sides and the base. Herein, an open system permits free intake and discharge of water by setting a constant hydraulic pressure boundary on the top surface, whereas the closed system prohibits water intake by setting an impermeable boundary on the top surface. For the mechanical field, the bottom was fixed in both vertical and horizontal directions, and both lateral side boundaries were fixed in the horizontal direction, while a prescribed overburden pressure was applied on the top surface.

4.2.2 Material properties and input parameters

The soils used in this study are all widely distributed in Hokkaido, Japan. Figure 4.3 shows the grain size distribution curves of the simulated samples. In this simulation, three typical frost-susceptible soils were used: Fujinomori soil (medium frost-susceptible loess), Touryo soil (high frost-susceptible volcanic soil), and Tomakomai soil (medium frost-susceptible volcanic soil). Fujinomori soil contains 18% clay, 78% silt, and 4% sand, while Tomakomai soil consists of 3% clay, 19% silt, and 78% sand, and Touryo soil consists of 26% clay, 21% silt, and 53% sand. According to ASTM, the Touryo soil, Fujinomori soil, and Tomakomai soil are classified as clayed sand (SC), lean clay (CL), and lean clay (CL), respectively. The soil input parameters used in the numerical simulation are listed in Table 1.

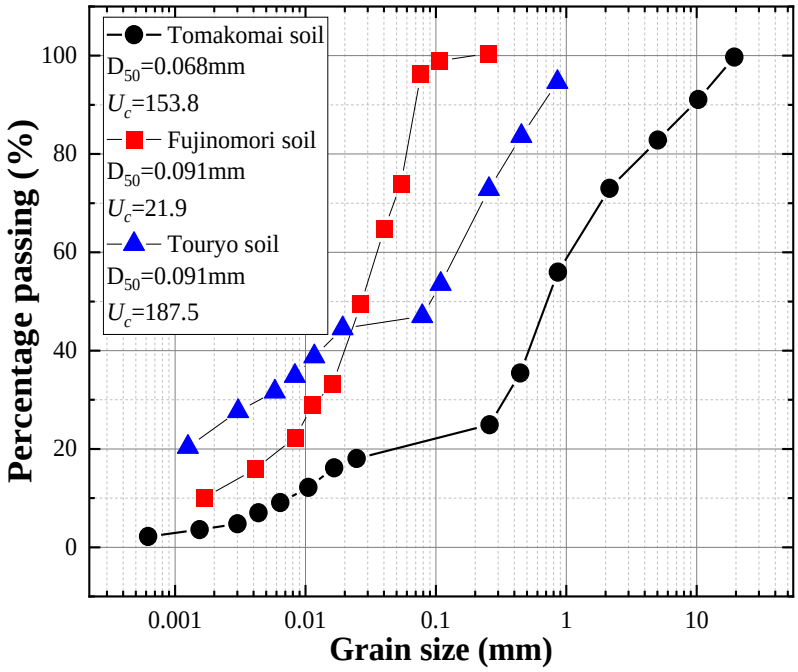

Figure 4.3 Grain size distribution curve of simulated soil samples.

Table 4.1 Soil properties used in the numerical simulation.

Abbreviation/ symbol	Parameter	Value			Unit
		Touryo soil	Fujinomori soil	Tomakomai soil	
C_s	Volumetric heat capacity of the soil particles	1.8E6	1.3E6	8.59E5	$J/m^3 \cdot K$
λ_s	Thermal conductivity of the soil mixture	1.61	0.83	1.61	$W/(m \cdot K)$
χ	Material parameters accounting for the particle shape effect	0.75	0.75	0.75	$W/(m \cdot K)$
η	Material parameters accounting for the particle shape effect	1.2	1.2	1.2	1
ρ_d	Dry density of soil particles	1400	1460	1200	Kgm^{-3}
n	Porosity	0.45	0.455	0.55	1
T_m	Final freezing temperature at	272.95	272.90	273.05	K

	atmospheric pressure				
α_{vg}	Van-Genuchten- Mualem fitting parameter	93.2	1.904	25.02	MPa^{-1}
λ_{vg}	Van-Genuchten- Muale fitting parameter	1.596	1.865	1.54	1
S_s	Saturated degree of saturation	96.7	100	95.1	%
S_r	Residual degree of saturation	37.8	18.5	33.5	%
k_s	Saturated water hydraulic conductivity	1E-8	5E-10	9.16E-9	ms^{-1}
α_{Tu}	Thermal expansion coefficient	1.2E-5	1.2E-5	1.2E-6	K^{-1}
E	Young's modulus of soil	40	12.5	8.5	MPa
H	Modulus related to matric potential	7653	7653	7653	m
υ	Poisson's ratio	0.4	0.33	0.4	1

The dry density and porosity of each soil sample are determined from the average of the results from each test group. Based on the recommendations of Guymon et al. (1993), the thermal conductivity and volumetric heat capacity of soil particles were determined according to the results of water retention tests. The Mualem-van Genuchten model parameters used in Equation 3.14-3.15 were obtained through parameter fitting to the water retention test (Ishikawa et al., 2015) . Based on permeability test results (Ueda et al., 2005; Nakamura et al., 2011; Stuurop et al., 2021), saturated hydraulic conductivity was determined for each soil. It should be noted that thermal expansion is considered to have only a marginal effect on the frost behavior of soil; thus, the thermal expansion coefficient for water is set to zero. Other parameters are given by previous studies(Liu and Yu, 2011; Luo et al., 2017) .

4.2.3 Numerical model verification

To verify the model, the numerical simulation results were compared against the frost heave test data conducted with Touryo soil by Ishikawa et al. (2015) and with Fujinomori soil by Tokoro et al. (2016), separately. In this study, the boundary conditions of the numerical model were set as the following: the cooling rate was set as -

0.2℃ at the pedestal, and the cap temperature remains 0.1℃; the overburden pressure was set as 10kPa in the top surface; permeable boundary condition was used at the top surface. In cold regions, pavements and foundations may be affected by uneven frost heave, so accurate prediction of frost heave is helpful in designing long-term maintenance programs.

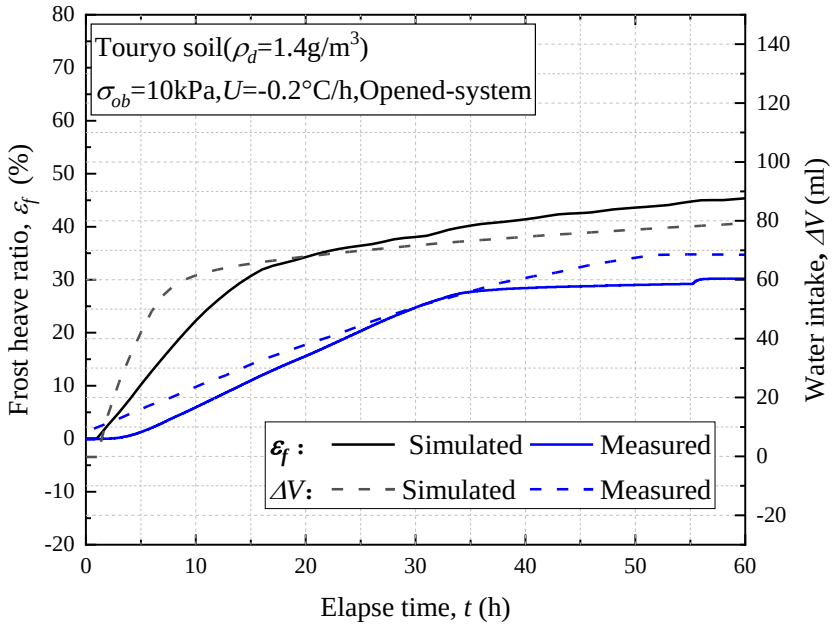

Figure 4.4 Frost heave test apparatus (a) a general view; (b) temperature measurement of specimen.

As shown in Figure 4.3, the tendency of the frost heave and water migration amount in the numerical simulation agrees very well with those in the experiment. It also can be seen that the frost heave ratio increased with the water intake amount, which indicates that sufficient water supply is a critical factor for ice growth and frost heave. Although the frost heave ratio and the amount of water migration are overestimated at the beginning of the freezing process, the difference between test results and simulation results decreases as the freezing process proceeds. Yu et al. (2020) and Zhao et al. (2013). Have also reported similar phenomena because of the sudden ice-water phase transition at the early simulation stage.

The two Fujinomori soil columns were forced to freeze under controlled boundary conditions in the experimental study of Tokoro et al. (2016). In this paper, by using the setup with their study, the soil columns were initially saturated. The cooling rate applied on the pedestals -0.075℃/h, and the cap temperature remained 0.1℃. Moreover, different overburden pressures as 50kPa and 100kPa were set on the top boundary of the samples. As shown in Figure 5, the results of the numerical model are in good agreement with the observed

values. Under both 50 kPa and 100 kPa conditions, the simulation results for the water intake amount of Touryo soil are in good agreement with the test results. Due to the sudden ice-water phase transition, the frost heave strain simulation results of Touryo soil are also somewhat overestimated at the beginning of the simulation, and as freezing progresses, the difference between numerical simulations and experimental results gradually diminishes.

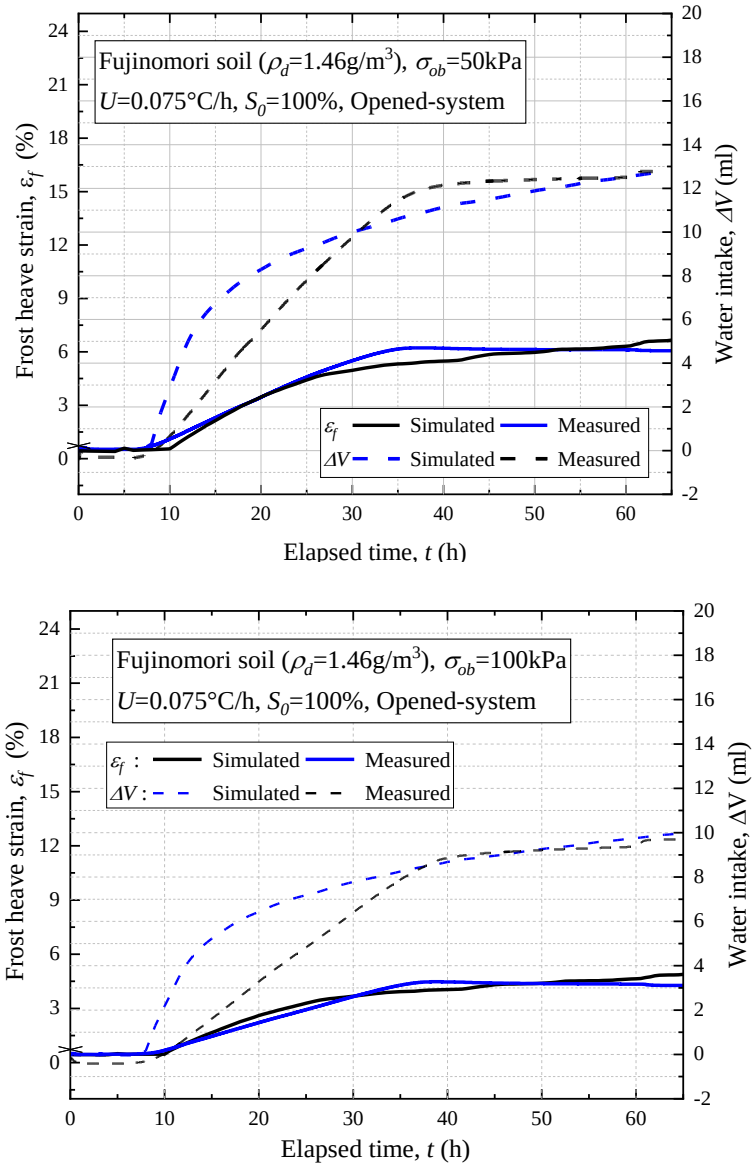

Figure 4.5 Comparison between numerical and experimental results of frost heave tests for Fujinomori soil on over burden pressure of (a) σ_{ob}=50kPa; (b) σ_{ob}=100kPa.

4.3 Parametric Analysis Using THM Coupled Model

To illustrate the stability of the proposed model in different conditions, frost heave tests of Touryo soil and Tomakomai soil were conducted for 60 hours. Factors affecting the frost heave amount of soils were summarized in Table 4.2.

Table 4.2 Experimental conditions

Number	Water supply system	σ_{ob} (kPa)		U (K/h)		S_0 (%)	
		Tomakomai soil	Touryo soil	Tomakomai soil	Touryo soil	Tomakomai soil	Touryo soil
1	Opened-system	5.0	5.0	0.2	0.2	95.0	81.7
2	Opened-system	10.0	10.0	0.2	0.2	95.0	76.1
3	Opened-system	15.0	10.0	0.2	0.4	95.0	69.0
4	Opened-system	10.0	10.0	0.1	0.8	95.0	70.0
5	Opened-system	10.0	50.0	0.2	0.2	69.9	81.0
6	Opened-system	10.0	100.0	0.2	0.2	80.2	92.7
7	Opened-system	10.0	200.0	0.2	0.2	95.0	82.7
8	Closed-system	5.0	0.0	0.2	0.2	95.0	98.9
9	Closed-system	10.0	5.0	0.2	0.2	95.0	98.9
10	Closed-system	15.0	10.0	0.2	0.2	95.0	98.9
11	Closed-system	10.0	10.0	0.2	0.2	66.1	98.9
12	Closed-system	10.0	10.0	0.2	0.2	79.0	98.9

4.3.1 Opened system

Figure 4.5 shows the influence of cooling rate on frost heave in an open system. The simulation results agree well with the

4.3.1.1 Effect of cooling rate on frost heave deformation

Figure 4.5 shows the influence of cooling rate on frost heave in an open system. The simulation results agree well with the test data. Meanwhile, the cooling rate has an obvious effect on frost heave, which shows higher cooling rate leads to less frost heave ratio. The unfrozen water tends to migrate to the freezing front driven by the cryogenic suction during freezing. Under a high cooling rate, the freezing front proceeds quickly from the cold end to the warm one of the specimen, which does not allow enough time for unfrozen water to migrate to

the freezing front and accumulate ice. On the contrary, when the cooling rate is low, a large amount of unfrozen water can migrate to the freezing front and form ice lenses, resulting in a larger amount of frost heave.

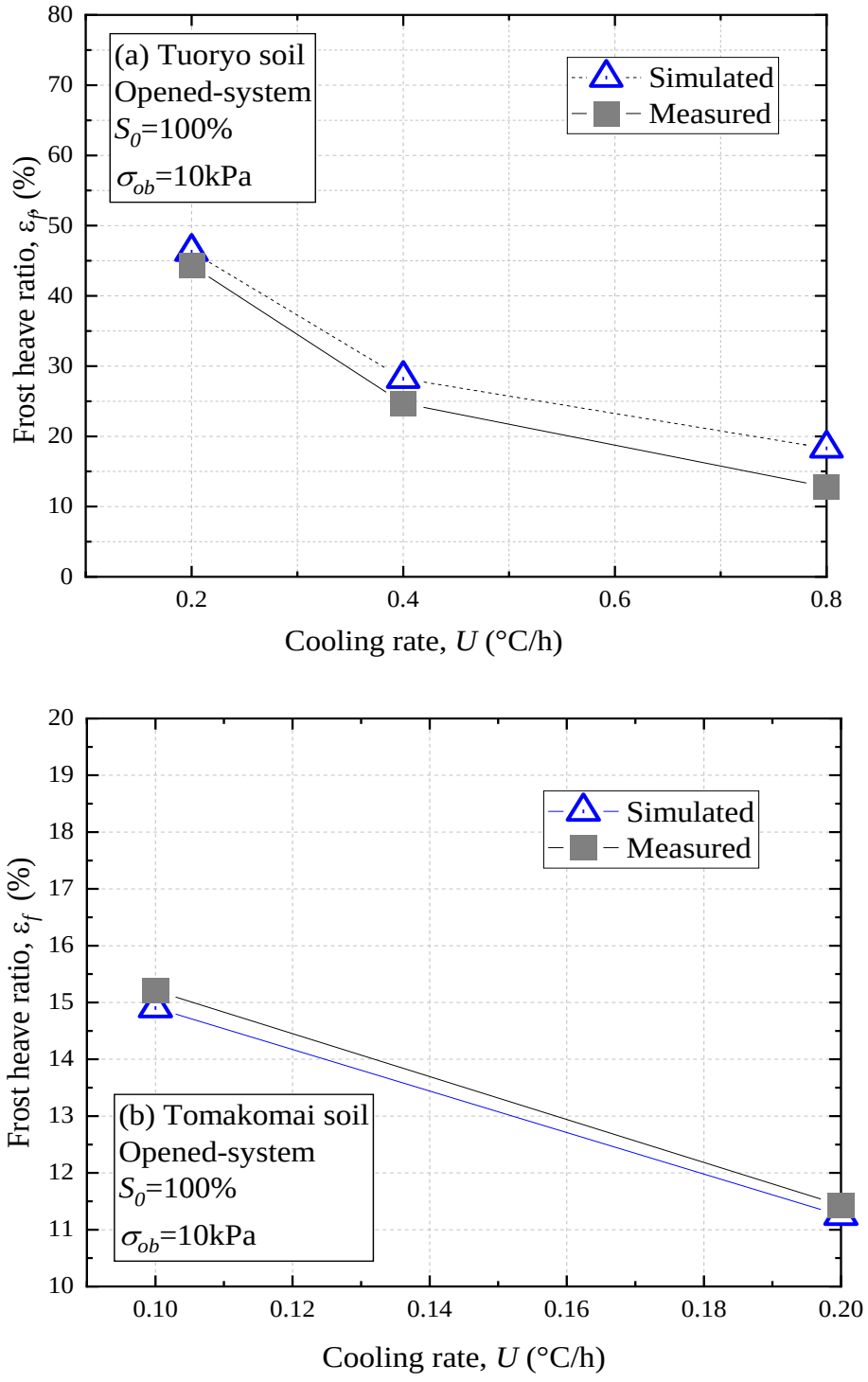

Figure 4.6 Influence of cooling rate in opened-system frost heave tests of (a) Touryo soil; (b) Tomakomai soil.

4.3.1.2 *Effect of overburden pressure on frost heave deformation*

Figure 4.6 illustrates the influence of overburden pressure on frost heave in the open system. The simulation results are close to the measured data. Moreover, the impact of overburden on frost heave is noticeable; the larger the overburden pressure is applied, the smaller the frost heave amount is generated. Meanwhile, the frost heave in the open system is much larger than in the closed system under the identical overburden pressure, as free water supply enables more ice accumulation.

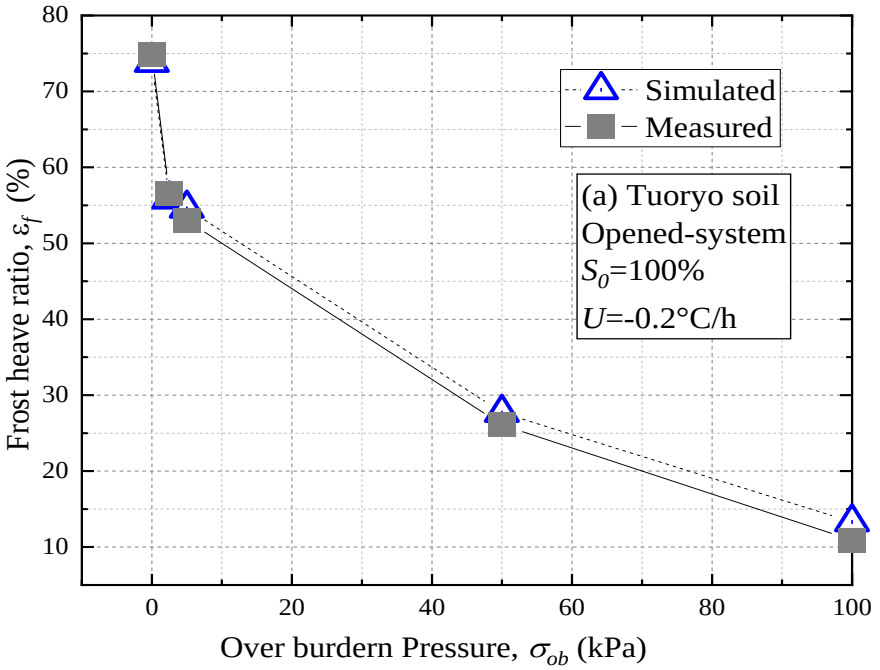

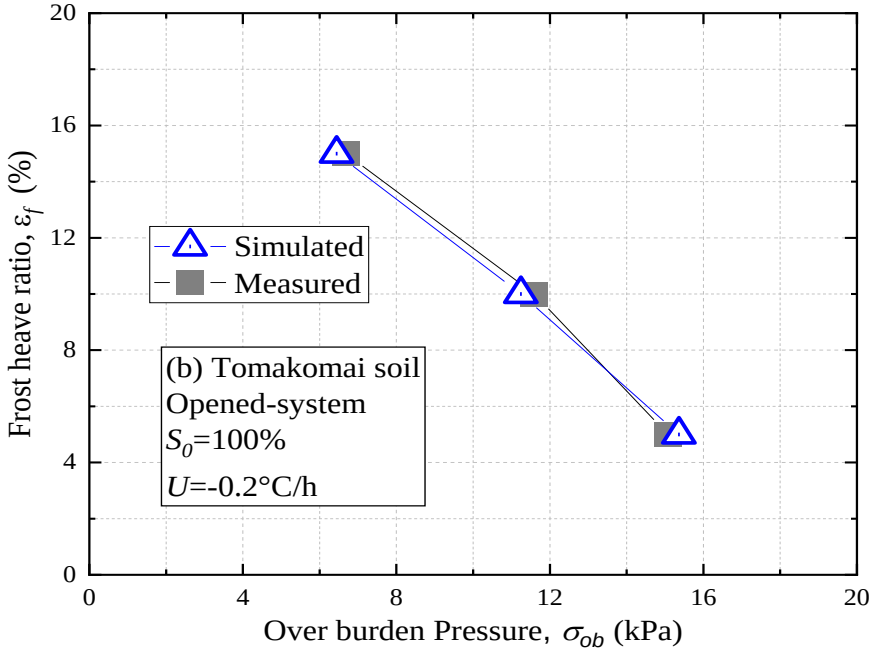

Figure 4.7 Influence of over burden pressure in opened-system frost heave tests of (a) Touryo soil; (b) Tomakomai soil.

4.3.1.3 Effect of initial saturation on frost heave deformation

Figure 4.7 depicts the influence of the initial saturation on frost heave in the open system. The simulation results fit the experimental results well. Higher initial saturation for both Touryo and Tomakomai soil leads to a more significant frost heave than lower initial saturation. The high frost heave amount is attributed to the higher water content. This tendency can be observed more clearly in Touryo soil, which has higher initial and residual degrees of saturation compared with Tomakomai soil. Larger initial and residual degrees of saturation indicate more pore water in Touryo soil. With negligible hydraulic permeability, the unfrozen water is harder to drain out than Tomakomai soil.

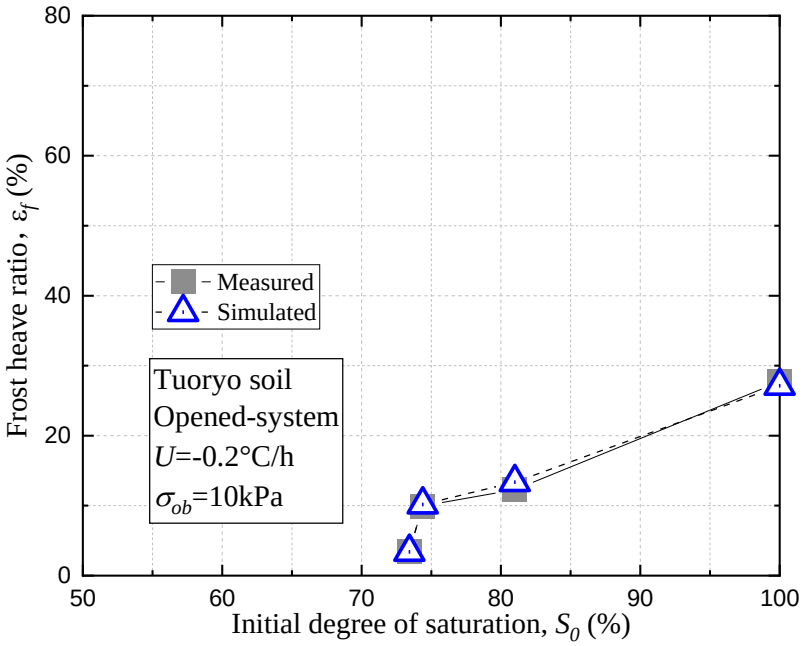

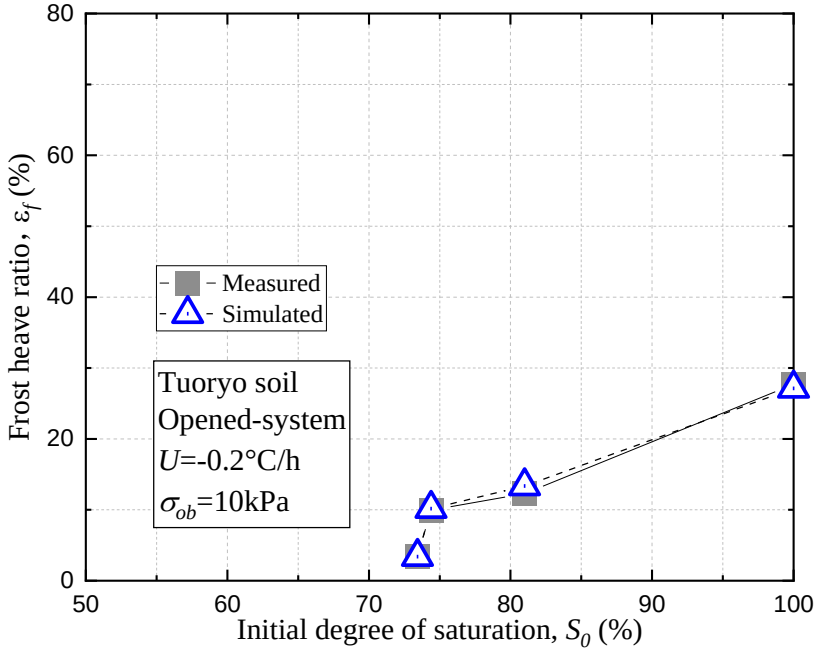

Figure 4.8 Influence of initial degree of saturation in opened-system frost heave tests of (a) Touryo soil; (b) Tomakomai soil.

4.3.2 Closed system

4.3.2.1 Effect of over burdern pressure on frost heave deformation

Figure 4.8 shows the comparison between measured and simulated frost heave ratios under different overburden pressures in the closed-system frost heave tests. The numerical models performed well in the simulations with two soil types. According to the simulation results, the frost heave amounts under 15 kPa are almost identical for Touryo and Tomakomai soil. In addition, it can be seen that the higher the overburden pressure was applied, the smaller the frost heave occurred, as the overburden pressure generated an initial strain shown in Equation (3.23).

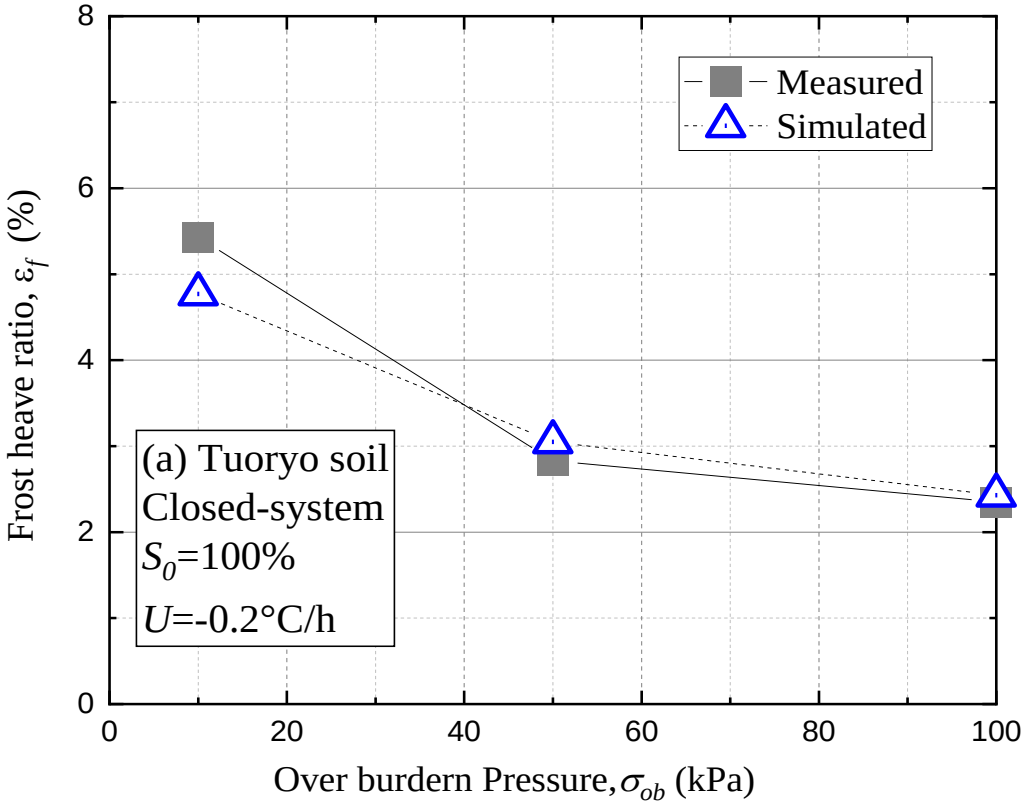

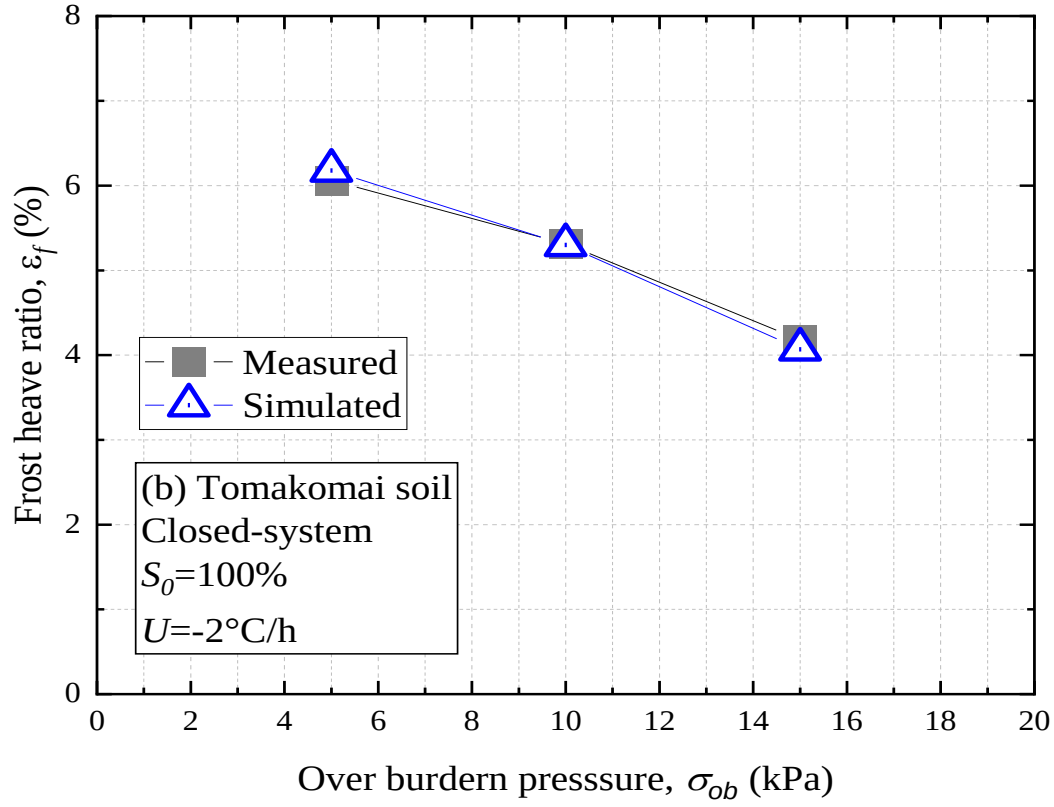

Figure 4.9 Influence of overburden pressure in closed-system frost heave tests of (a) Touryo soil; (b) Tomakomai soil.

4.3.2.2 *Effect of initial saturation on frost heave deformation*

Figure 4.9 compares the frost heave ratios of Touryo and Tomakomai soil from the simulations and experiments under the various initial saturation in the closed system. The comparations show that the simulation results agree well with the test data. Moreover, lower initial saturation leads to a smaller frost heave ratio since lower water content allows less water migration to the freezing front.

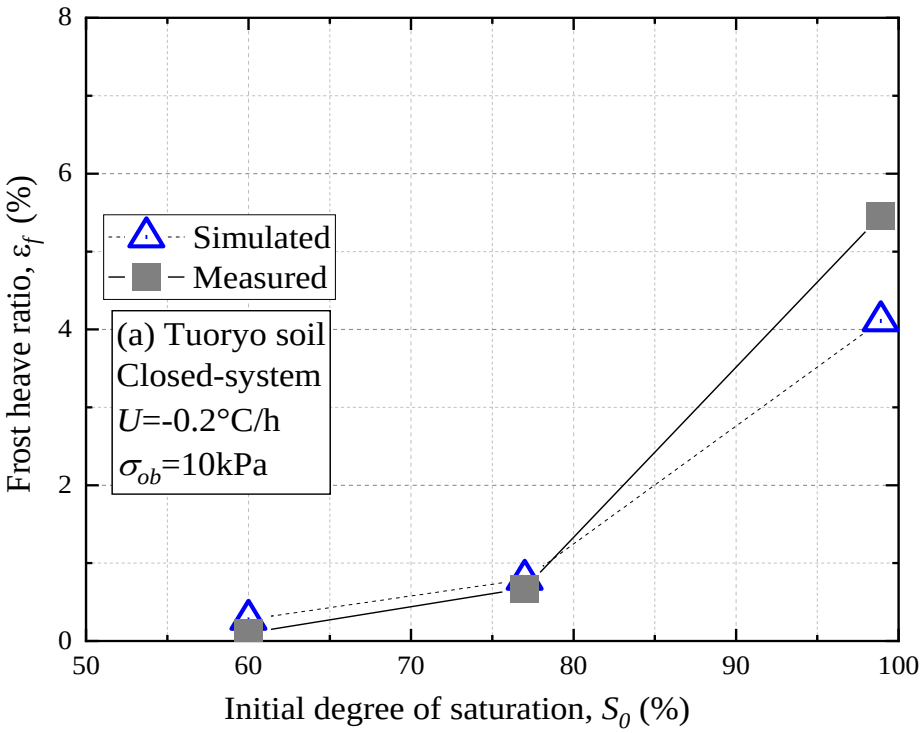

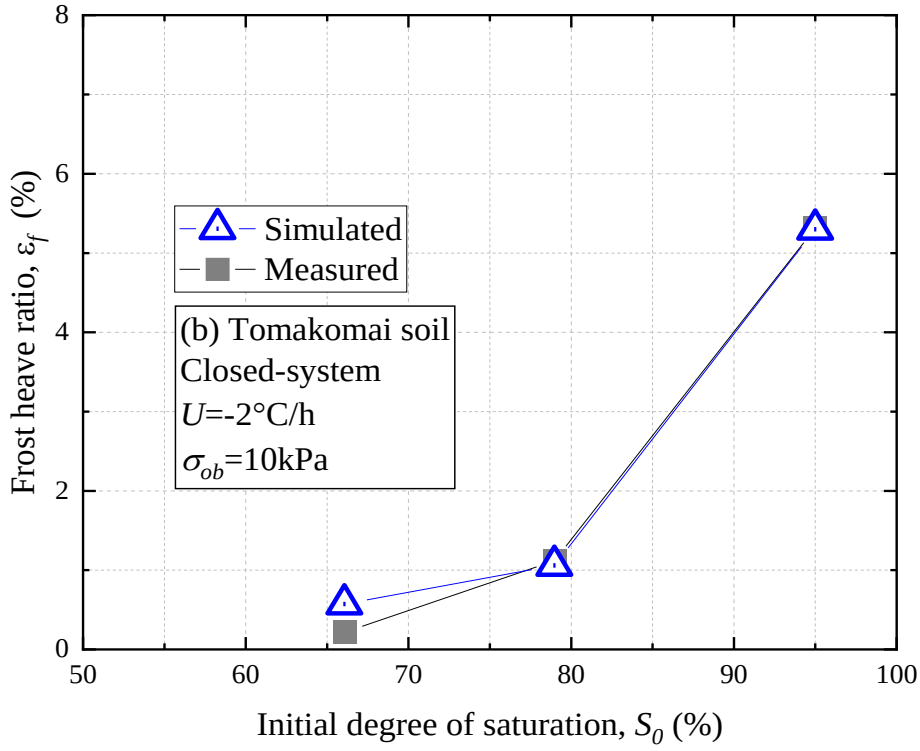

Figure 4.10 Influence of initial degree of saturation in closed-system frost heave tests of (a) Touryo soil; (b) Tomakomai soil.

4.3.3 Typical parameters analysis

Because the phase interaction with each other, coupled phenomena are a very characteristic feature of the problems(Gens and Olivella, 2001). Thus, a typical parameters analysis is conducted in this section. To reproduce the freezing process and observe the freezing mechanism, a closed-system frost heave test of fully saturated Touryo soil was chosen as the prototype for the computational model construction in the simulation. The specimen was frozen from the bottom up, and the pedestal temperature changed from 0℃ to -3℃ in 15 hours, and the cap temperature remained 0.1℃. The sample was thermally insulated on the sides. Furthermore, a constant overburden pressure σ_{ob}=10kPa was applied to the top surface. The impermeable boundary condition was applied to all the boundaries.

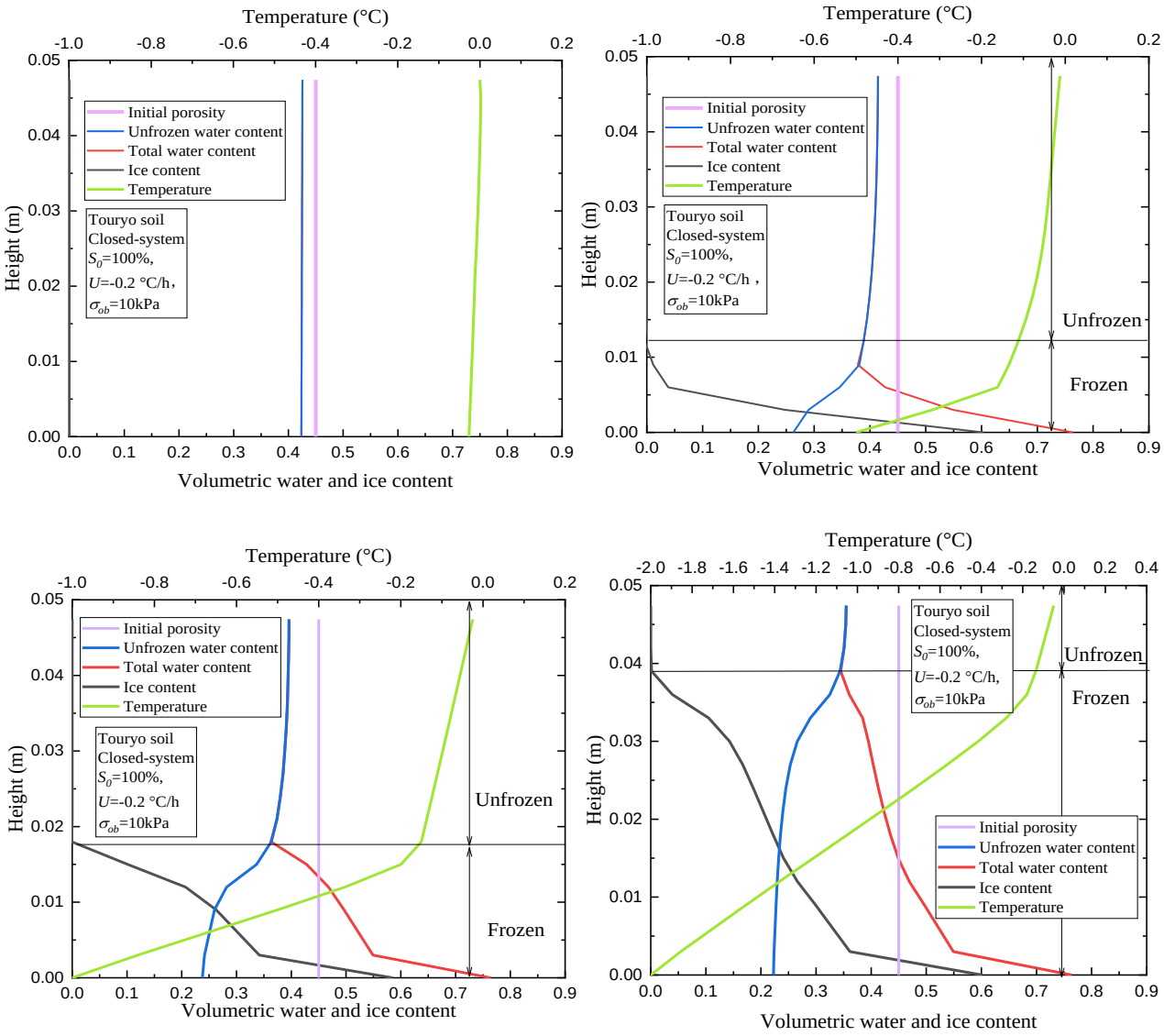

Figure 4.11 Volumetric water and ice content and temperature profile in freezing process on (a) 0h; (b) 2.5h; (c) 5h; (d) 10h.

The unfrozen zone is the area without ice content. Once ice generates, the area is considered to be the frozen area. As shown in Figure 4.10, the temperature changes rapidly in the frozen zone, while the temperature becomes steady in the unfrozen zone due to the ice formation. Since the thermal conductivity of water is lower than that of ice, the heat flux in the frozen zone is more accessible to transfer than that in the unfrozen area, which leads to the temperature gradients in the frozen and unfrozen zones. In the unfrozen zone, the total water content (water and ice) is always coincident with the unfrozen water content, and the ice content keeps zero. The unfrozen water content drops in both frozen and unfrozen zone while ice content increases in the frozen zone. The total water content is much more prominent in the frozen area than in the unfrozen area, which

illustrates that the soil sucks water from the soil in the unfrozen area driven by cryogenic suction gradient during the freezing process and causes ice accumulation nearby the freezing front.

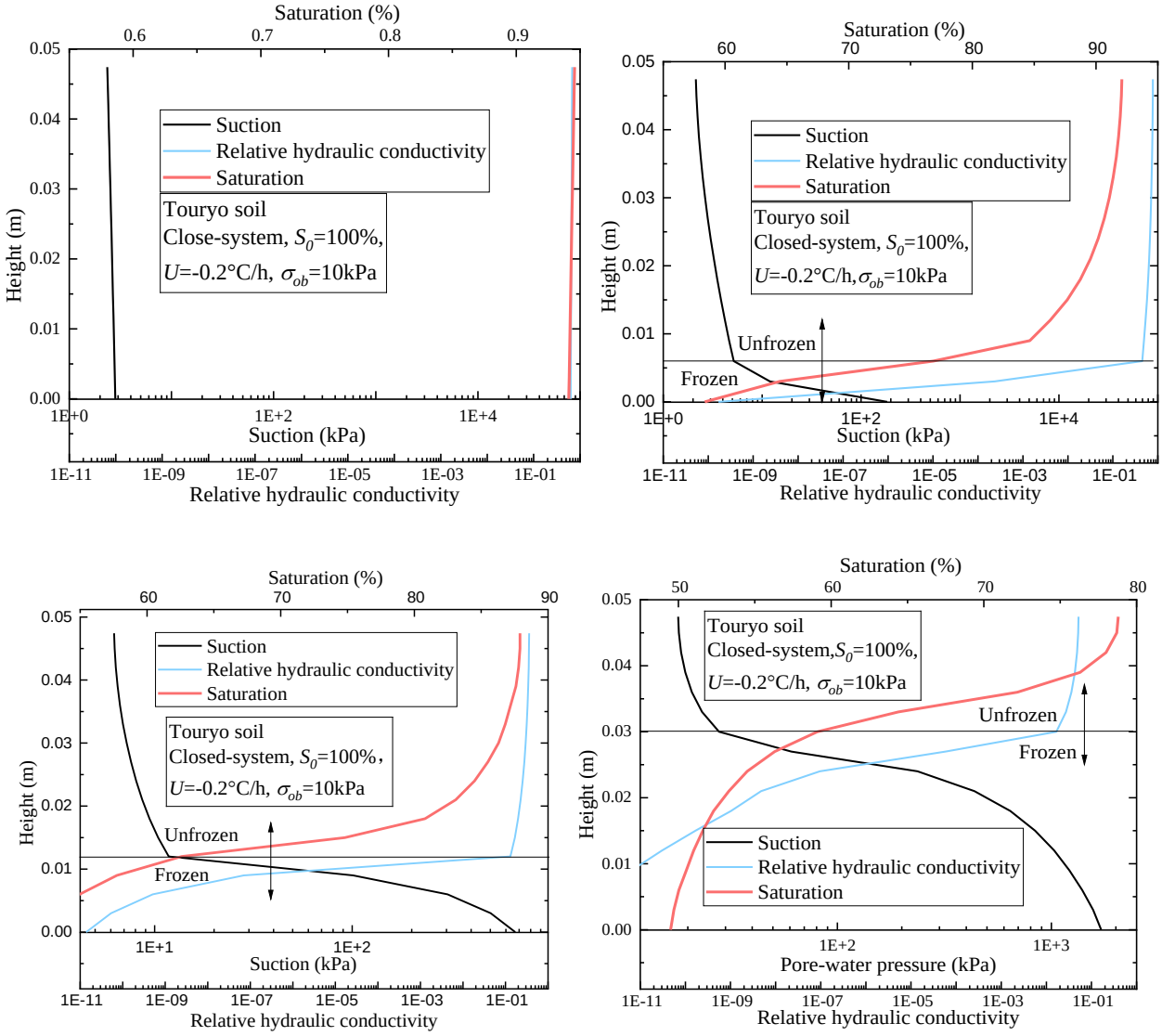

Figure 4.12 Volumetric unfrozen water and ice content profile and frost heave ratio relationship in freezing process on (a) 0h; (b) 2.5h; (c) 5h; (d) 10h.

Suction, saturation, and relative hydraulic conductivity are the main factors that would affect the unfrozen water migration. The profiles in 10 hours freezing process are shown in Figure 4.11. In saturated conditions, the initial porosity means the volumetric water content. It can be seen that the cryogenic suction increased sharply while the relative hydraulic conductivity decreased rapidly in the frozen area, resulting in a significant increment of total water content near the freezing front, as shown in Figure 4.12. Here, Figure 4.12 presents the volumetric unfrozen water and ice content profiles as well as the deformation relationship at 0, 2.5, 5, 10

hours of freezing, respectively. Moreover, as the relative hydraulic conductivity decrement is more significant than the pore-water pressure increment, water is hard to migrate in the deeper frozen area. Therefore, the ice content in the deeper frozen area increases slower than in the freezing front.

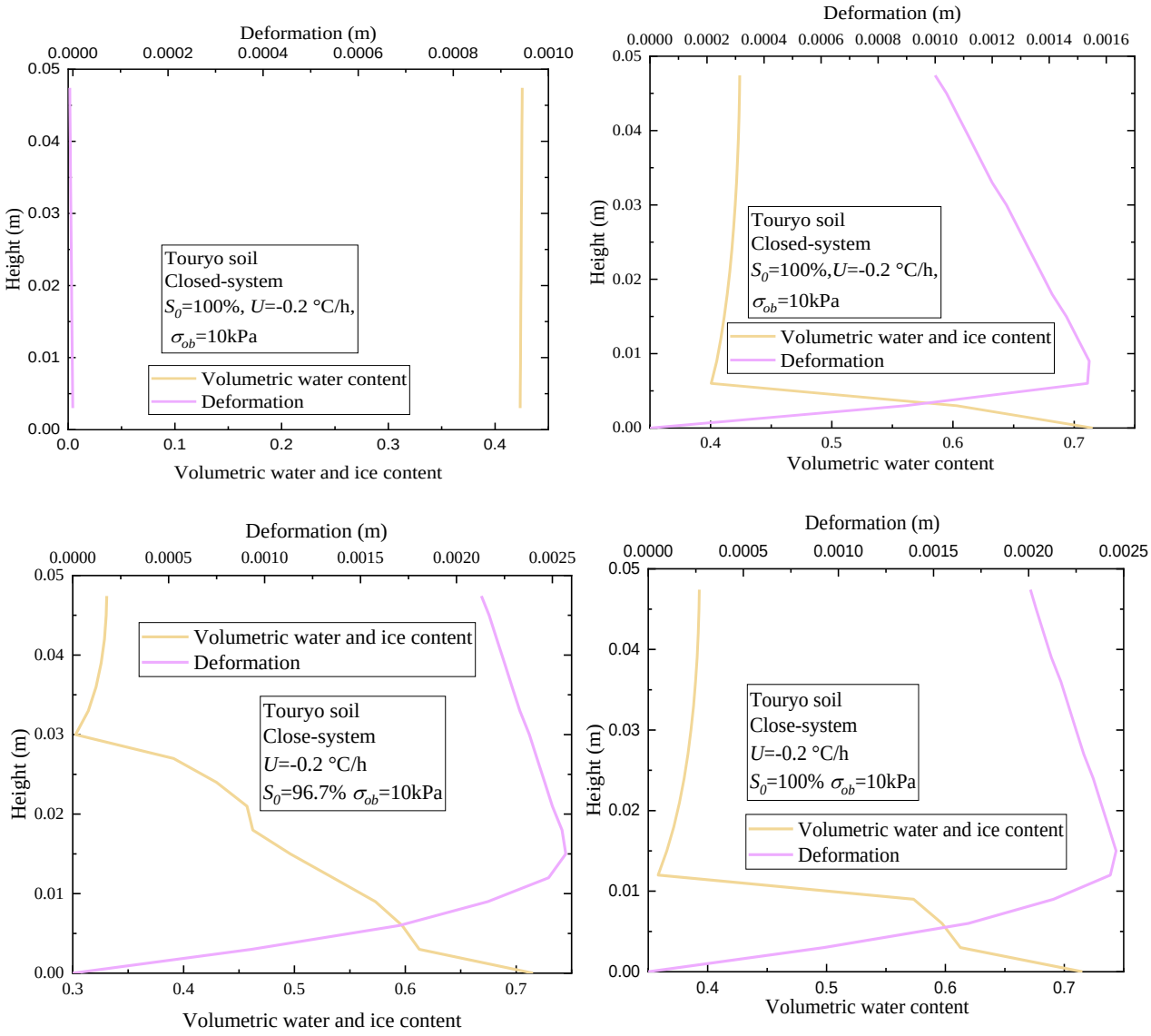

Figure 4.13 Volumetric unfrozen water and ice content profile and frost heave ratio relationship in freezing process on (a) 0h; (b) 2.5h; (c) 5h; (d) 10h.

The unfrozen water content in the unfrozen zone decreased gradually while the deformation increased as the frozen area developed. Figure 4.12 shows that there exists a maximum value along with the height of the specimen. During the freezing process, the unfrozen water migrates to the freezing front and is transferred to ice. The excessive water and ice content enlarge the specimen. Meanwhile, as unfrozen water migrates to the frozen area, the water content in the unfrozen zone is decreased. Under the overburden pressure, the

deformation of the soil above the freezing front was suppressed. In addition, Figure 4.12 shows that in the frozen zone, the frost heave amount grows faster at the early freezing process (from 0h to 2.5h) than at the end of freezing analysis (from 5h to 10h). And, it is attributed to the fact that, as the freezing developed, the unfrozen water content and permeability in the unfrozen zone kept decreasing, which makes it difficult for the unfrozen water to migrate to the freezing front, and the unfrozen water is insufficient to supply to the freezing front and form ice lens.

Simulating the freezing process generally comes up with high computational cost and numerical instabilities because of the highly nonlinear relationship between unfrozen water content, ice content, water head, temperature, and hydraulic conductivity caused by substantial latent heat and phase change. The proposed numerical model performed well for all the test problems. This model can be used for many different experiment conditions.

4.4 Summary

In this chapter, a coupled THM model was built to simulate partially saturated soil in the freezing process. The validity of this model is confirmed by comparing the simulated frost heave ratio and water migration amount with those of the test data. The proposed model performs well in predicting the frost heave and water migration amount for different soils. Parametric analysis indicates that the frost heave ratio is proportional to the initial degree of saturation, and it is inversely proportional to the cooling rate and overburden pressure. Moreover, simulation in the open system generates much more frost heave compared with that in the closed system. The proposed model can capture the main features of unsaturated soil during freezing, such as suction-induced freezing point depression, water redistribution caused by cryogenic suction gradient, and, most importantly, frost heave.

The research findings in this chapter indicate that the proposed model in this chapter provide a possible way to simulate the freezing process in both saturated and unsaturated soils, and experiment conditions may greatly influence the frost heave. It is of great significance to evaluate the frost heave in the unsaturated pavement. However, the vapor migration and plastic deformation is not considered in this part. These should be considered in the further assignment.

5 PREDICTION OF RAINFALL AND SNOWMELT INDUCED SLOPE FAILURE ON THE REGIONAL-SCALE

Chapter 3 presents a theoretical model that describes the water absorption phenomenon of WF during freezing. This chapter begins with a detailed introduction of the laboratory model test to examine the inhibition effect of WF on frost heave. Then a numerical model is developed based on the theory presented in Chapter 3. The reliability of the proposed model is verified by comparing the simulation results with the experimental results. The effects of different experimental conditions on the frost heave suppression effect of WF are discussed through numerical simulations. The conclusions drawn from this study provide some information on how to apply WF in engineering practice.

5.1 WF Model Test

5.1.1 Experiment set up

Figure 5.1 is a schematic diagram of a frost heave test device installing WF. Two thermostatic baths, which circulate an anti-freezing liquid at a specific temperature, are used to control the temperature of the upper cooling plate and lower cooling plate independently. The porous metal plate at the bottom of the device is connected to a water tank, to maintain a constant groundwater level (GWL) for the device. At the height of 150 mm from the pedestal, on one side of the model, a sliding opening of 100 mm in width and 0-2.5 mm in height is installed to place the geotextile. The specimen is installed with five moisture sensors (ECH2O soil moisture sensor), five thermal sensors (T-type thermocouples), and two suction sensors (tensiometers) to measure temperatures, saturations, and suctions at the observation point in the freezing process. The soil surface temperature is measured using a platinum resistance temperature detector. Besides, the displacement transducer is used to measure the specimen frost heave. The applied load represents the forces acting on the subgrade in the actual pavement structure.

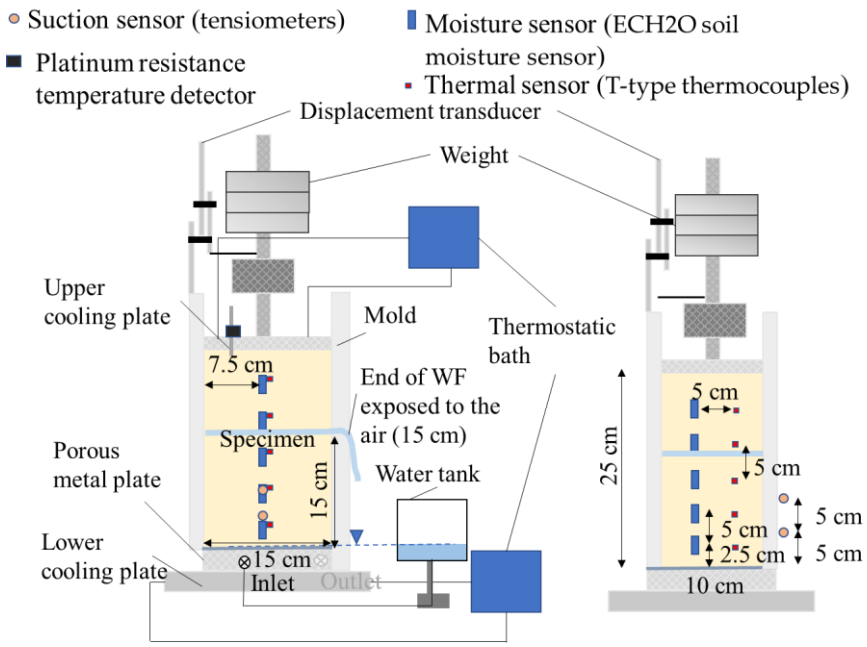

Figure 5.1 Schematic of the test apparatus.

5.1.2 Soil column preparation

The selected soil sample was obtained from Tomakomai, Hokkaido, where the soil is usually used as a subgrade layer. In addition, a density test (JIS A 1202:2009), a sieve analysis (JIS A 1204:2009), and a compaction test (JIS A 1210:2009) were conducted. The density (ρ_s) and the maximum dry density (ρ_{dmax}) of the soil are 2.64 g/cm3 and 1.27 g/cm3, respectively. The uniformity coefficient (Uc) is 153.8. This soil can be classified as SFG (sand fine particle and gravel) according to JGS 0051(2009). The optimum water content of the Tomakomai soil is 32.0%. After the in-situ soil is dried, it was sprayed with water until the water content reached 90% and sealed with plastic bags to prevent evaporation of moisture and get uniform water content distribution.

The test apparatus is shown in Figure 5.1. In the NWF model experiment, the wet soil samples were placed into the mold in 5 layers and compacted by layers from bottom to top. Each layer was compacted using a 2.5 kg rammer in order to achieve compaction of 95.0% (ρ_d = 1.21 g/cm3) and saturation of 90%. To prevent stratification of soil, the surface of each layer 1-4 was scraped after compaction. Before filling in the next layer of soil samples, a T-type thermocouple and a moisture meter were placed. The first layer of soil samples was 2.5 cm deep, and the second to fifth layers were each 5 cm thick. On the other hand, in the WWF model experiment, a dry WF (100 mm wide by 300 mm long) was laid into the soil after the soil sample was filled to

a depth of 150 mm, and its end was exposed from the preset slide at a length of 150mm. Afterward, the 4-5th layers of soil were placed on the top. The size for both soil columns is 250mm in height, 150mm in width, and 100mm in depth.

5.1.3 Test procedure

Figure. 5.2 shows the test setup of the frost heave model test. An overburden pressure of 10 kPa was applied at the top of the specimen in accordance with the pavement thickness in the field test. The frost heave model test of the soil column was carried out as follows. First, the initial condition of a test specimen was set with the saturation process followed by the drainage process, under a room temperature of 9 °C and a room humidity of 50%. In the saturation process, the GWL was set to 0.25m by adjusting the height of the water tank connected to the soil specimen, and the water inlet connected to the porous metal plate was opened, allowing water to flow into the soil specimen. When the temperature and water content of the soil specimen no longer fluctuate, the GWL was adjusted to the bottom of the soil specimen (0 m) to drain the water out. This status is considered as the initial condition of the soil specimen before the freezing process. It should be noted that the initial water content distribution for the WWF model is different from that for the NWF model. In the WWF model, the initial water content decreases more than the NWF model due to the drainage of the WF.

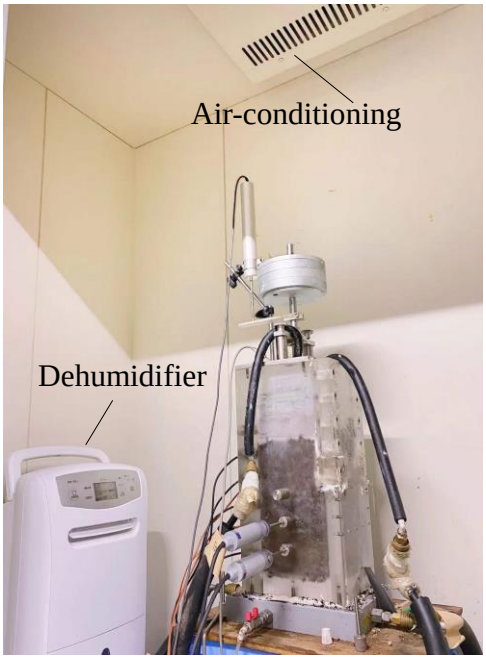

Figure 5.2 Picture of the test set up.

Next, once it was confirmed that the measured temperature and volumetric water content of the specimen were stable, the freezing process was conducted under a room temperature of 0 °C and a room humidity of 50%. At first, the temperatures

of the upper and lower cooling plates were set at 0.5°C using a thermostatic bath. This temperature was maintained until the soil specimen achieved a steady state. After that, the temperature of the upper cooling plate was rapidly dropped to -10°C, while keeping the temperature of the lower cooling plate constant. By generating latent heat (thermal shock), the supercooled state was avoided. Following the thermal shock, the temperature of the upper cooling plate was returned at -1.0°C, while the temperature of the lower cooling plate was maintained at 0.5°C. To maintain the freezing rate in the range of 1mm/h to 2mm/h, the temperature of the upper cooling plate was reduced from -1.0°C in a constant gradient (U=0.1°C/h) for 100 hours. During the freezing process, the water supply valve was kept open so that the water could migrate from the water tank to the soil specimen via the inlet. In addition, the mold had an opening that enabled one end of the WF to be exposed to air, where the moisture absorbed by the WF evaporated or drained out.

5.2 Verification of WF Evaporation Model

5.2.1 Model configuration

The simulations were performed under various test conditions, including WWF and NWF models, with different frost-sensitive soils, cooling rate (U), and GWL (l). Assuming that the bottom of the soil sample is the origin and upwards is positive, l is the distance from the origin to the upper surface of the saturated zone in the soil. Besides, the assumption of 2D plane strain was made and 850 quadrilateral cells were utilized to mesh the model. Line source was used in this model to represent the evaporation process of WF. Guo et al. (2019) concluded that evaporation of WF could be considered similar to water absorption when the WF exposed to air is equal to or greater than the WF buried in the soil. Since the lengths of the WF exposed to air and the WF buried in soil in the model test were both 150 mm, the water absorption of the WF could be considered equivalent to the evaporation of the WF, following the assumption by Guo et al (2019). Therefore, the evaporation process of WF is described by a line source, indicating that the water absorbed from the soil is directly discharged from the line source.

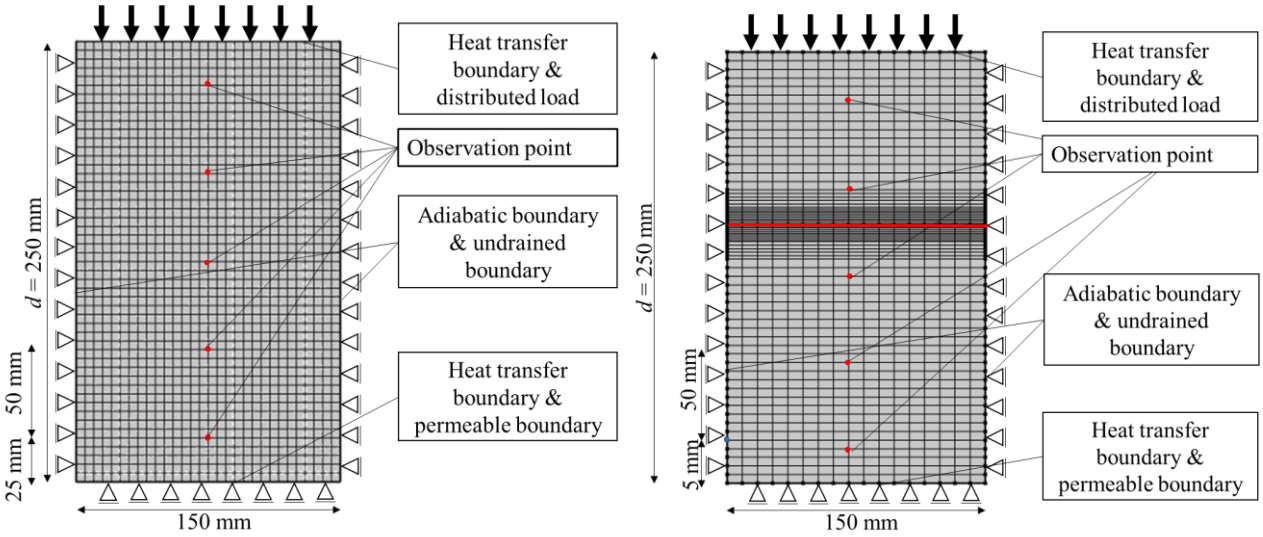

Figure 5.3 (a) NWF model and boundary conditions for model tests; (b) WWF model and boundary conditions for model tests.

The size of the sample, boundary conditions, and mesh of the two-dimensional model are presented in Figure 5.3. The water content near the WF varies significantly during the freezing process. Thus, in the WWF model, refined grid was adopted near the WF. The observation points in this study were placed at the same locations as the measured sensors in the model test, for the consistency between the numerical simulation and the test results. There are five observation points located at the height (d) of 25 mm, 75 mm, 125 mm, 175 mm, and 225 mm away from the origin, respectively. The dimensions of the soil column are 250mm x 150mm (H x W), which is similar to the actual model test. It is noted that the bottom of the soil is set at a baseline (0mm), and the value (d) is considered upward as positive.

The initial boundary conditions of the NWF model were set as follows. The base surface was fixed vertically, and its lateral boundaries were fixed horizontally in the mechanical field. The hydrostatic pressures were applied to the base surface to maintain a constant GWL; Impermeable boundaries were applied to the lateral sides and top surface in the hydraulic field. The adiabatic boundary condition was applied on the two lateral sides, while on the top and bottom surfaces, the constant thermal boundary condition was applied. Except for the suction boundary caused by WF, the boundary conditions for the WWF model are the same as those for the NWF model. As shown in Figure 5.3(b), the evaporation model (Eq. 3.30), working as a line source, has been applied to WF to simulate the drainage process caused by WF. The water absorption process occurs in this scenario at the WF buried within the specimen.

5.2.2 Material properties and input parameter

Tomakomai soil, Touryo soil, and Fujinomori soil were used in the model test, which are the same soil samples used in the one-dimensional frost heave test. Figure 4.3 and Table 4.1 provide information on the material properties and the input parameters.

5.2.3 Temperature filed verification

The temperature distribution is one of the most important indicators of frozen soil, since it affects soil frost penetration depth and therefore the design of the foundation burial depth. The numerical results were compared with the experimental data to validate the pro-posed model. All these experimental and numerical results were obtained from their respective single tests.

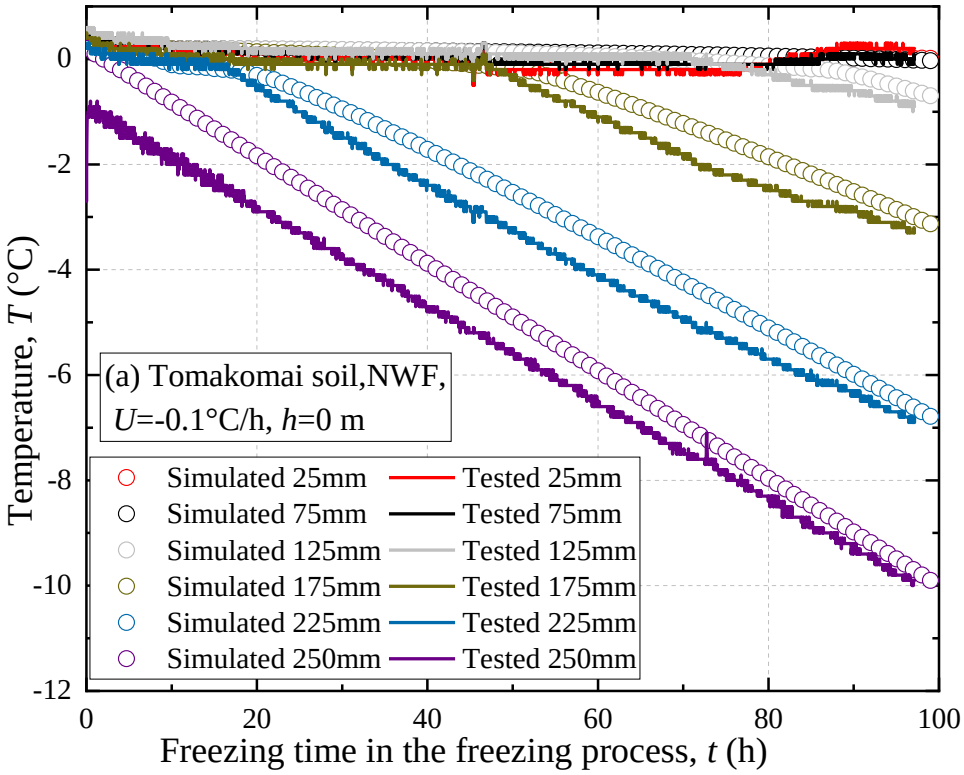

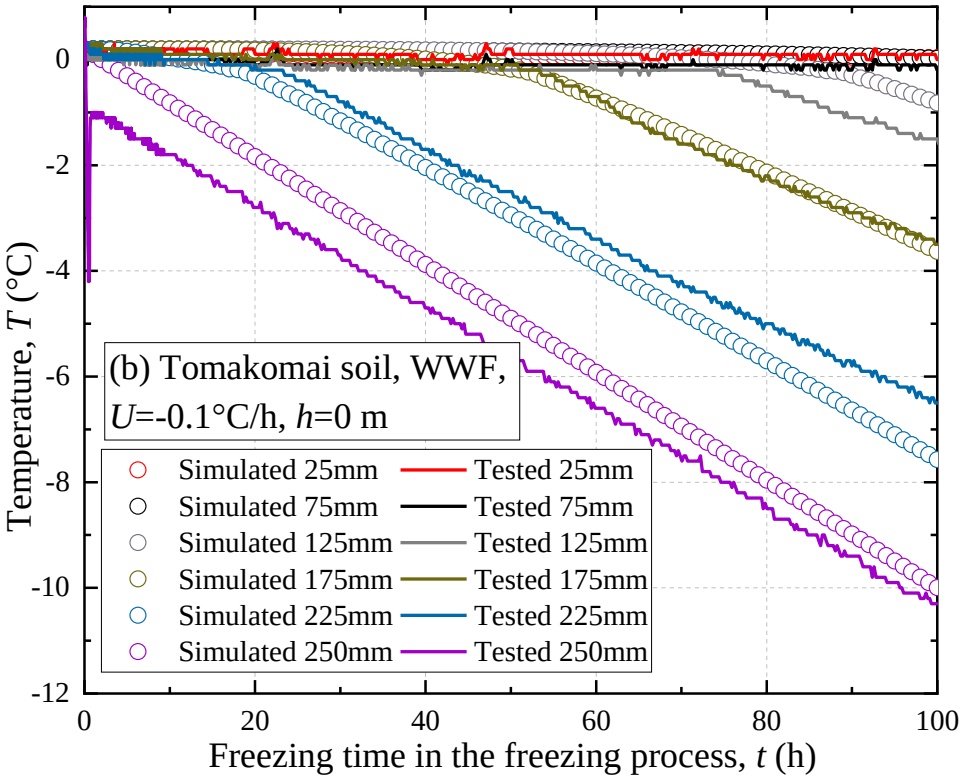

Figure 5.4 Comparison of the simulated and tested temperature development at the different observation points on (a) NWF model and (b) WWF model.

Figure 5.5 shows comparisons of the temperature distribution for soil columns at different observation points in the numerical and experimental studies. The simulation results for both the WWF and NWF models are consistent with the experimental results at each observation point. Additionally, the comparison of the results between the WWF model and the NWF model reveals that these two models do not show significant differences in temperature distribution and variations during the freezing process. The results demonstrate that the proposed model can accurately simulate temperature changes in the WWF and NWF models during the freezing process.

5.2.4 Hydraulic field verification

Figure 5.6 presented the volumetric water content variation in the freezing process at the different observation points of simulation results and experimental results. In the WWF model, simulation results for water content at 125mm differ significantly from experimental results. The moisture sensor at this site was found to be broken when checking the experimental equipment after the test. However, the numerical calculations were consistent with the experimental results for other observation points. The results indicate that the proposed model is capable of predicting the development and distribution of water content in the freezing process.

In both WWF and NWF models, the volumetric water content decreases rapidly once freezing begins; the closer the observation point is to the cold end, the more significant the reduction in volumetric water content. Furthermore, Table 2 presents the freezing rate (U_0), frost heave rate(U_h), frost heave ratio(ζ) and frost penetration depth(l_0) in model tests and numerical simulations. The freezing rate (U_0), frost heave rate(U_h), frost heave ratio(ζ) and frost penetration depth(l_0) stand for the rate at which the freezing front advances into the unfrozen soil, the amount of frost heave per unit time, the increase in volume of soil due to freezing expressed as a percentage of the volume before freezing and the depth to which the ground water in soil is expected to freeze (JGS 0171-2009, JGS 0172-2009). The freezing rate is determined by the freezing time and the frost penetration depth. Assuming the bottom surface as origin and d as the distance from the origin, upwards as positive, freezing begins at the top surface (d=250mm). The freezing rate was calculated by divide the distance between d=225mm and d=125mm with the time differential between the freezing front developed to the two points. Multiplying the freezing rate by the freezing time (100 hours) gives the frost penetration depth. Both in simulations and model tests, the WWF model has a deeper frost penetration depth than the NWF model. As a result of the lower water content due to the WF, the heat capacity of the soil mixture in the WWF model is smaller than the one in the NWF model, and the thermal conductivity is higher. Therefore, under the same freezing conditions, WWF model took less time to freeze to the same height as NWF model. Comparing at the same observation point and the same freezing time, the volumetric water content in the WWF model is much smaller than that in the NWF model. Additionally, the water content in both the WWF and NWF models decreased significantly with increasing freezing time. Compared to the NWF model, the WWF model showed a more significant decrease in water content over time. This phenomenon occurs because the water in the WWF model is sucked out by the WF.

Table 5.1 Frost heave test and simulation results.

	WWF		NWF	
	Simulated	Tested	Simulated	Tested
U_0 (mm/h)	1.724	1.882	1.587	1.562
U_h (mm/h)	0.157	0.156	0.276	0.295
l_0 (mm)	172.4	188.2	158.7	156.2
ζ (%)	6.28	6.26	11.04	11.79

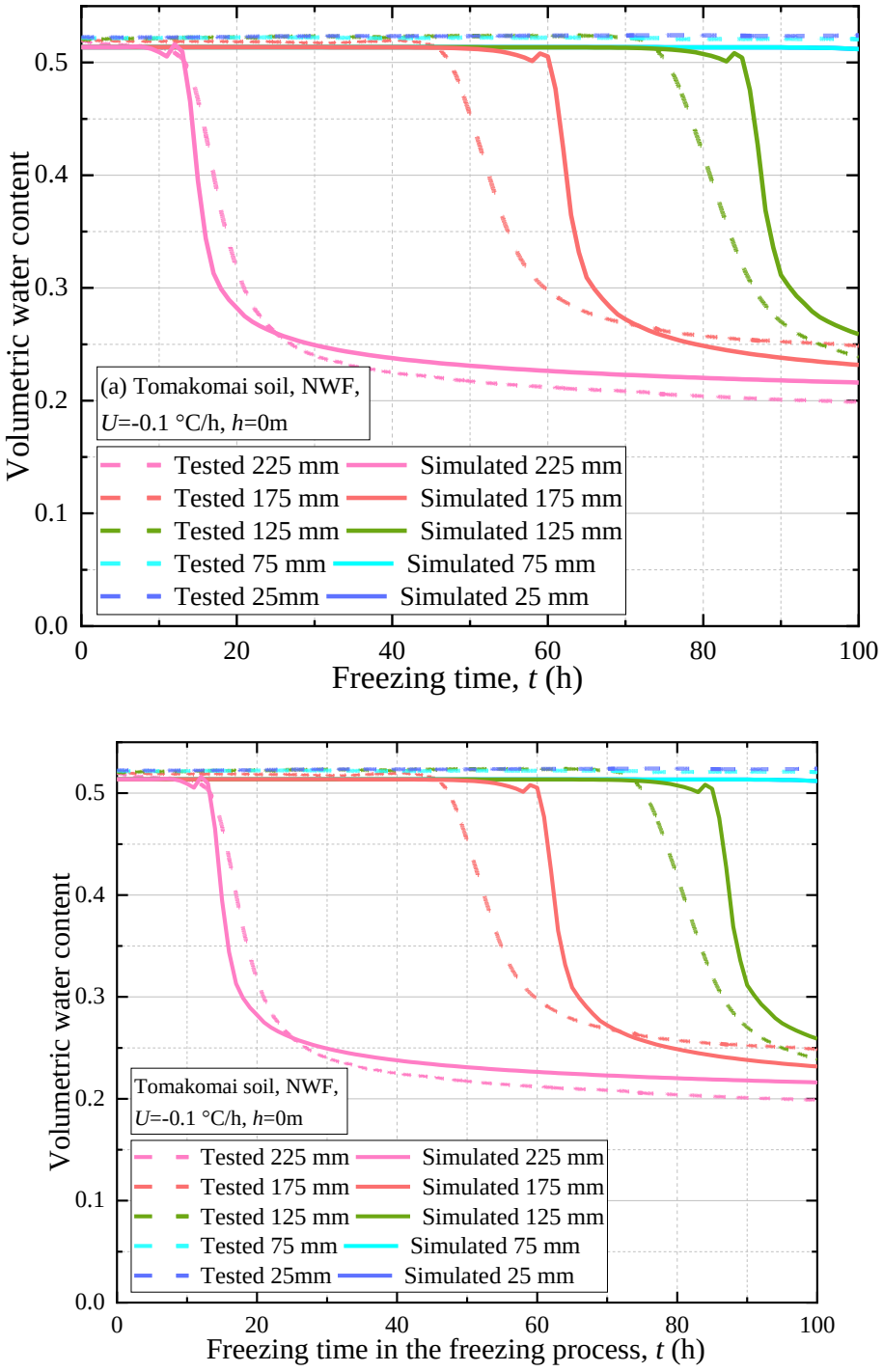

Figure 5.5 Comparison of the simulated and tested volumetric water content at the different observation points on (a) NWF model and (b) WWF model.

Figure 5.7 shows the change in distribution for degree of saturation (*S*) within the WWF and NWF models with time in the freezing process. Here d represents the distance from the bottom of the soil as the origin and upwards as positive. The saturation of WWF and NWF models gradually decreases as the temperature of the cold end decreases. Compared to the NWF model, the saturation around the WF is significantly reduced in the WWF model. In addition, the comparison

between the WWF and NWF models reveals that the saturation in the WWF model is significantly lower than the saturation in the NWF model. Based on the saturation changes observed in the WWF model and the NWF model during the freezing process, it is found that WF can significantly reduce the saturation during the freezing process, thereby depressing the development of frost heave. Furthermore, the saturation on the upper side of WF reduced more dramatically than on the underside, and Lin et al. (2019) also came to a similar conclusion in their experiment. Figure 5.7 illustrates that the water absorption effect of WF in Figure 5.6 and the frost heave depression effect of WF in Figure 5.8 can be rationally explained based on the simulation results with the proposed model.

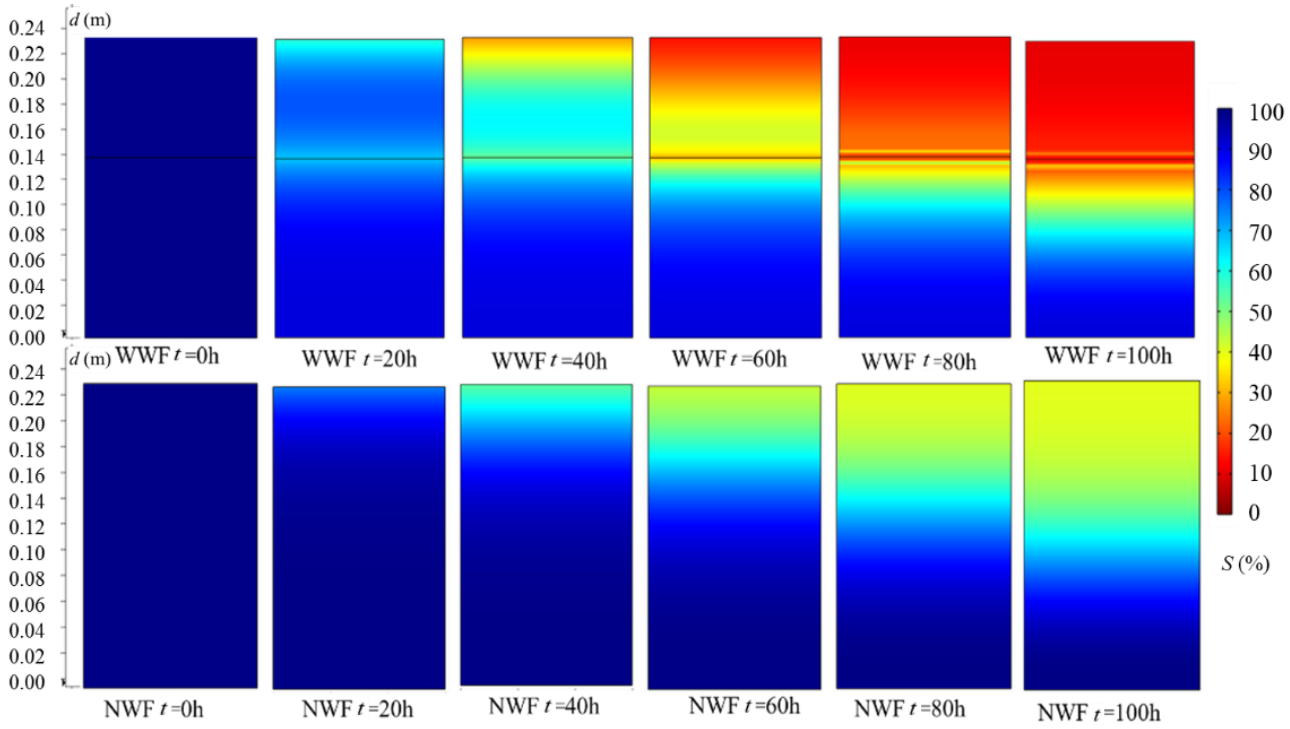

Figure 5.6 Comparison of saturation distribution for Tomakomai soil between NWF model and WWF model in the freezing process.

5.2.5 Mechanical field verification

A comparison of the measured frost heave strain during frost heave test with the simulated results are shown in Figure 5.8. It appears that the simulation results agree well with the experiment results. It should be noted that the WWF model produces significant-ly less frost heave rate and ratio than the NWF model at the same freezing time. This is due to the corresponding decrease of water content in the WWF model since WF has significant drainage effects(Zornberg et al., 2017; Guo et al., 2019). In addition, from the comparison of the experimental data and simulation results, it is shown that the model proposed in this study accurately de-scribes the depression effect of WF during freezing.

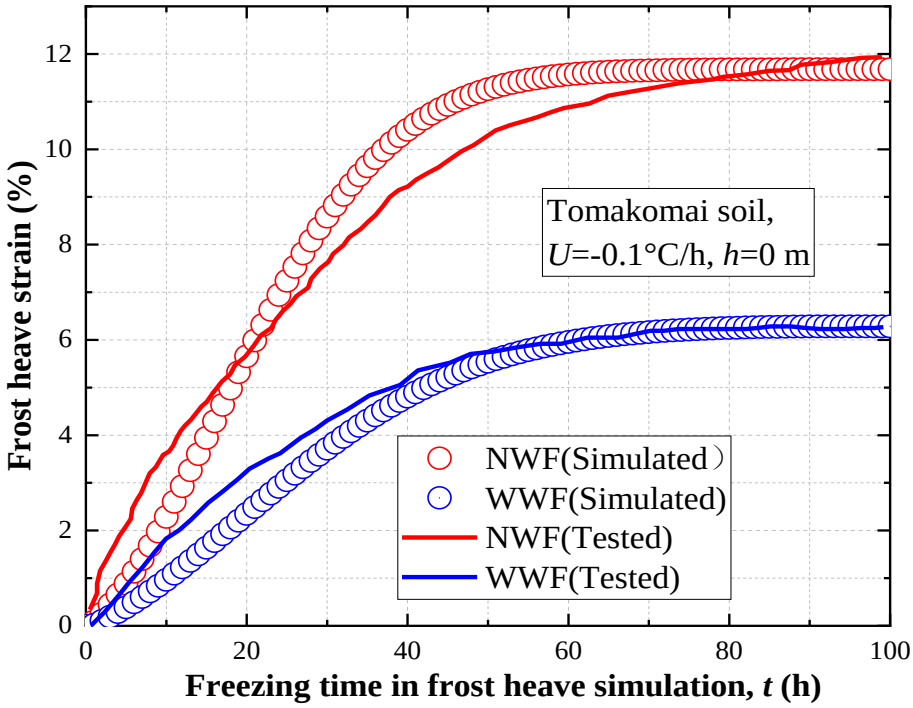

Figure 5.7 Comparison between numerical and experimental results of frost heave strain for frost heave tests of Tomakomai soil.

5.3 Parametric Analysis Using WF Evaporation Model

This study conducted three sets of comparison numerical experiments under different soil types, groundwater levels, and cooling rates as shown in Table 5.2 to illustrate the effectiveness of WF for depressing frost heave, because several factors may influence the efficacy of WF on depressing frost heave.

Table 5.2 Numerical simulation conditions.

Number	Soil type	GWL *l* (m)	*U* (°C/h)	WF Installation
1	Touryo soil	0	-0.1	WWF
2	Fujinomori soil	0	-0.1	WWF
3	Tomakomai soil	0	-0.1	WWF
4	Touryo soil	0	-0.1	NWF

5	Fujinomori soil	0	-0.1	NWF
6	Tomakomai soil	0	-0.1	NWF
7	Tomakomai soil	0.02	-0.1	WWF
8	Tomakomai soil	0.04	-0.1	WWF
9	Tomakomai soil	0.06	-0.1	WWF
10	Tomakomai soil	0.02	-0.1	NWF
11	Tomakomai soil	0.04	-0.1	NWF
12	Tomakomai soil	0.06	-0.1	NWF
13	Tomakomai soil	0	-0.05	WWF
14	Tomakomai soil	0	-0.2	WWF
15	Tomakomai soil	0	-0.05	NWF
16	Tomakomai soil	0	-0.2	NWF

5.3.1 Influence of soil type on frost heave inhibition effect of WF

This section investigates the frost heave depression effectiveness of WF in different soils using three types of frost-susceptible soils. The calculated frost heave strain of differ-ent soils in WWF and NWF models are shown in Figure 5.9. The overall frost heave strain in the WWF model of different soils is lower than that in the correspondent NWF model. Comparing the frost heave depression efficiency of WF in different soils, it can be found that by installing WF, the frost heave strain has decreased dramatically in Touryo soil, followed by Tomakomai soil, and lastly, Fujinomori soil. Although WF is effective in both Touryo soil and Tomakomai soil, it does not perform well in Fujinomori soil. One possible explanation is that Touryo soil has the most excellent permeability. In the NWF model, moisture can easily migrate upward to the freezing front due to the high permeability. Similarly, in the WWF model, soil with a high permeability would allow the moisture to be readily absorbed by the WWF compared to soils with lower permeability. Accordingly, the WF effect is more apparent in soils with high permeability.

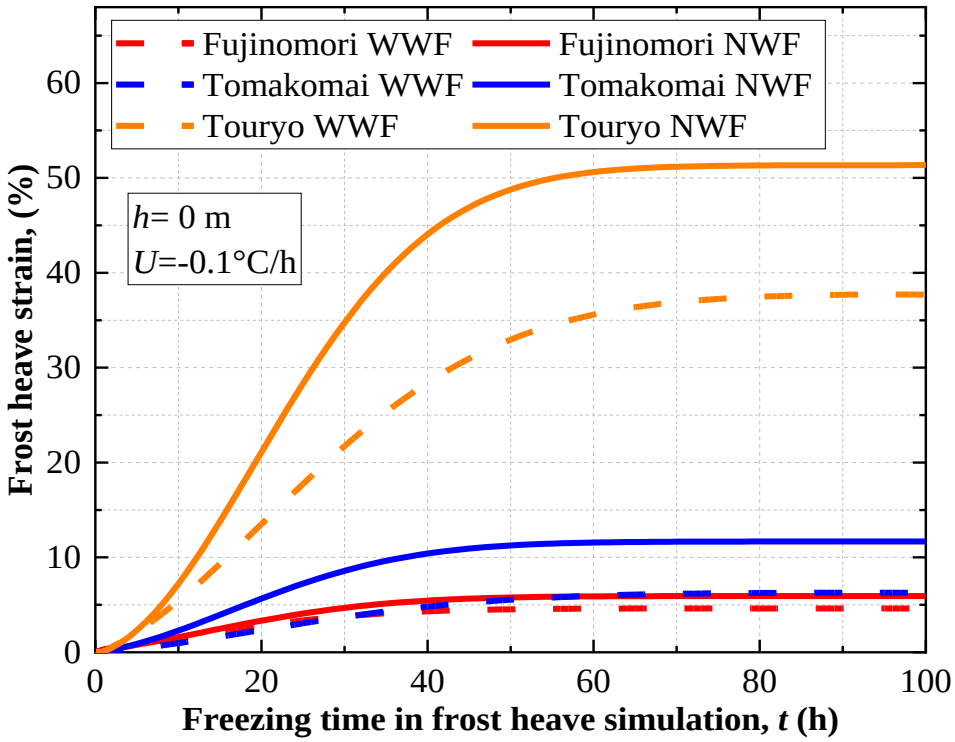

Figure 5.8 Effect of soil types on frost heave and WF depressing effect.

Figure 5.10 shows the saturation (*S*) distribution at the end of the freezing process with different types of soils in the WWF and NWF models. By comparing the saturation distributions in the WWF and NWF models for different soils, it is apparent that the saturation distributions for each of the soils in the WWF model were lower than those in the corresponding NWF model. There was a substantial decrease in saturation in the Touryo soil and Tomakomai soil by installing WF, while the reduction in soil saturation in the Fujinomori soil was relatively insignificant. The changes in the soil saturation after the installation of the WF are consistent with the observed results of frost heave inhibition. The above phenomenon indicates that WF can inhibit frost heave by reducing the water content in the soil, and the inhibition effect of WF is dependent on the permeability of the soil.

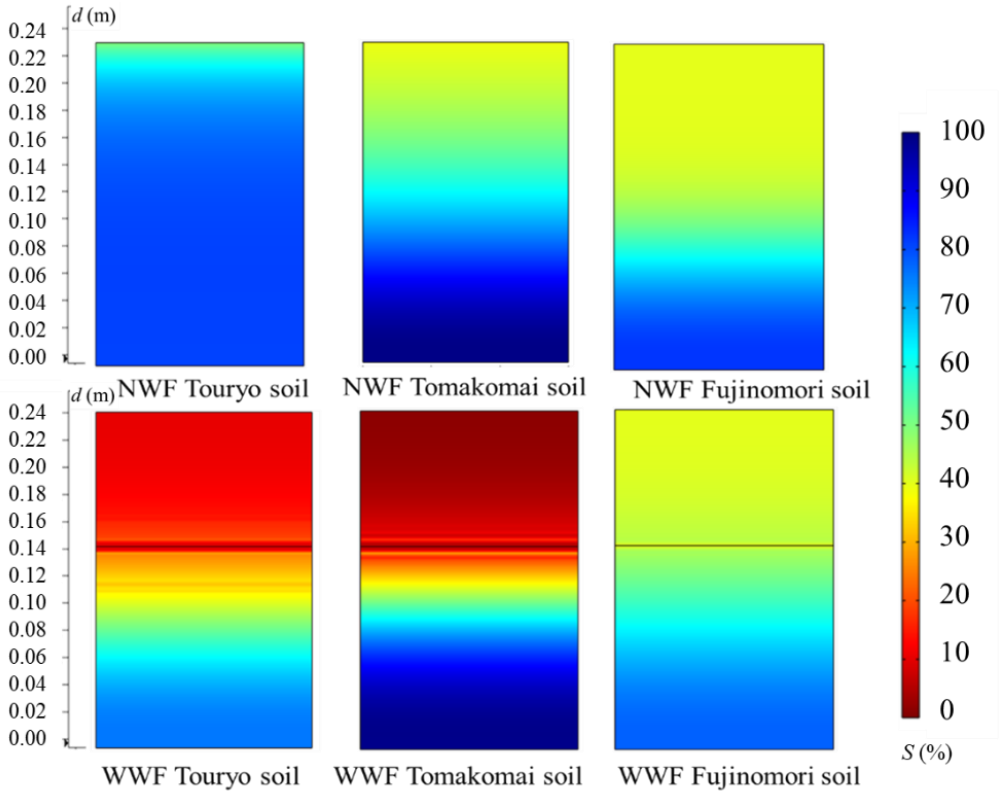

Figure 5.9 Effect of soil types on frost heave and WF depressing effect.

5.3.2 Influence of cooling rate on frost heave inhibition effect of WF

This section investigates the effects of the cooling rate on frost heave strain and the efficiency of drainage by the WF during the freezing process. Figure 5.11 illustrates the comparison between frost heave strain in the WWF and NWF models under different cooling rates. Moreover, a comparison of the saturation variations between the NWF and WWF models is presented in Figure 5.12 for different cooling rates during the freezing process. The WWF model shows the inhibiting effect of frost heave throughout the freezing process compared to the NWF model, regardless of the cooling rate. Moreover, according to the comparison of the simulated frost heave strain in the NWF models under different cooling rates, the frost heave strain increased as the cooling rate decreased. Based on this observation, the cooling rate has a greater impact on reducing frost heave strain during the freezing process. The slower cooling rate allows moisture to migrate upwards to the freezing front and form ice lenses, which leads to a larger amount of frost heave. A high cooling rate can rapidly convert the water in the soil into ice, thereby reducing the soil permeability and making it more difficult for the moisture to migrate. The insufficient water supply in the high-cooling-rate circumstance will result in a limited frost

heave ratio in the freezing process. Therefore, the increase in the cooling rate decreases the efficiency of the WF in inhibiting frost heave strain.

On the other hand, though the WF is evidently capable of effectively draining water under different cooling rates, as shown in Figure 5.12, it can sufficiently remove moisture from the soil, especially at the low cooling rate. Consequently, low cooling rates result in a more apparent reduction in frost heave strains of the WWF model during the freezing process. For example, the saturation distribution in the soil is almost similar when the cooling rates are 0.1 °C/h and 0.2 °C/h. The saturation distributions of U = 0.1 °C/h and U = 0.2 °C/h in their corresponding NWF models are significantly different, indicating that the WF has a greater drainage effect when the cooling rate is lower.

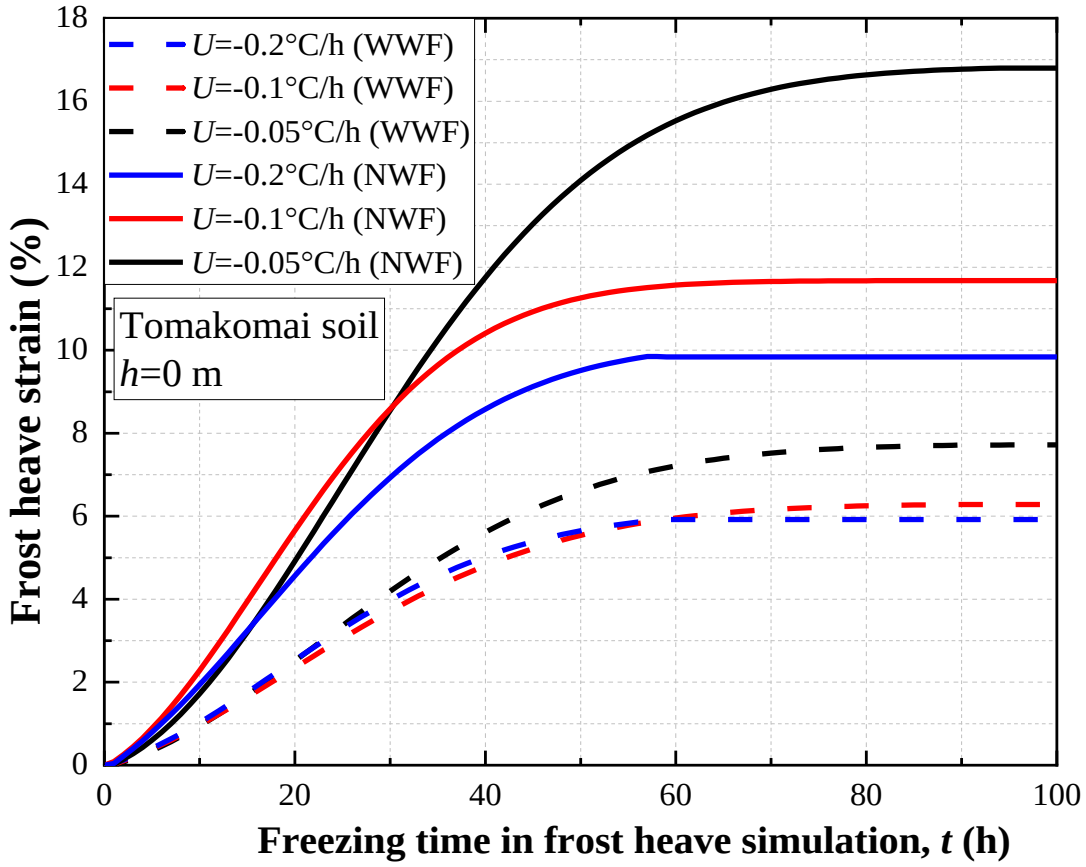

Figure 5.10 Effect of cooling rate on frost heave and WF depressing effect.

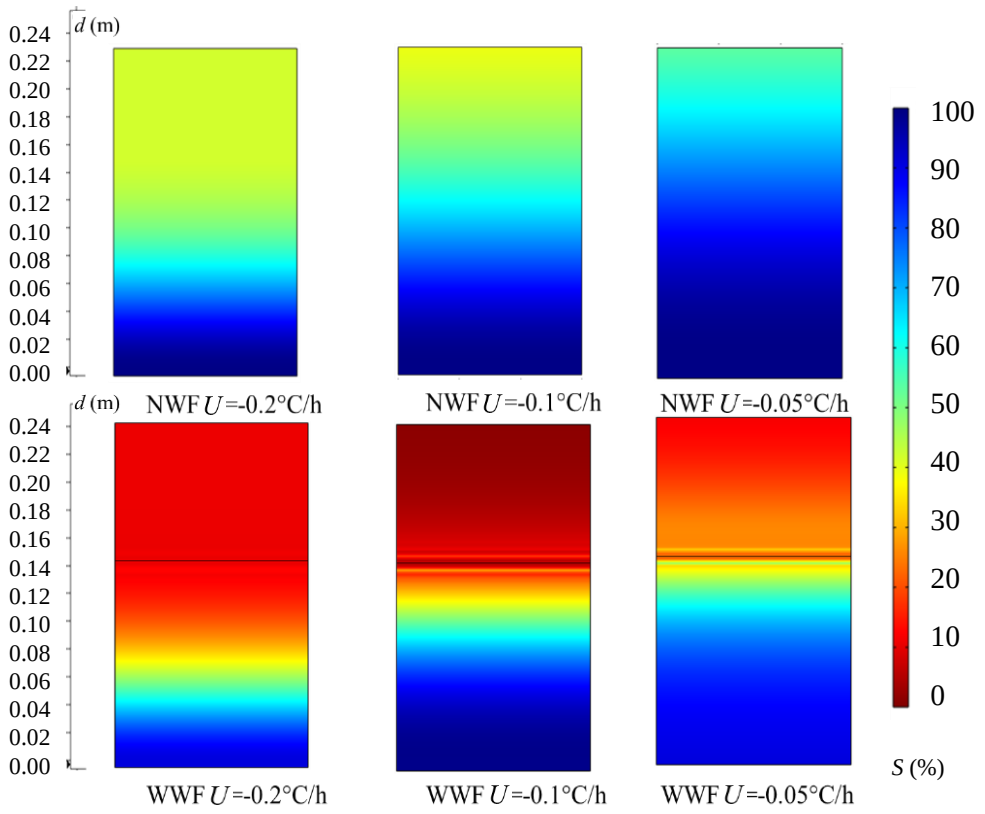

Figure 5.11 Comparison of saturation distribution between NWF model and WWF model in the freezing process.

5.3.3 Influence of groundwater table on frost heave inhibition effect of WF

Frost heave and the effects of WF are also influenced by groundwater availability. Groundwater provides the mass necessary for ice formation. Based on Beskow's pioneering study (1935) of frost heave, reducing GWL reduces frost heave. Sheng et al. (2013) also demonstrated that the higher the water level, the greater the amount of heave.

Figure 12 illustrates the simulated results of frost heave strain with time at different GWL for a fixed installation position for the WF in Tomakomai soil. Figure 10 illustrates how WF is very effective in suppressing frost heave in both Touryo and Tomakomai soils. However, the WF reduced 26.58% deformation in Touryo soil, while it decreased 46.2% deformation in Tomakomai soil. Therefore, in the simulation, the Tomakomai soil was found to be more effective in inhibiting frost heave in freezing process. Hence, the Tomakomai soil was chosen as the subject of investigation in order to observe more clearly the variation of the effect of WF on frost heave inhibition in response to variances in GWL. Besides, the saturation (S) variation during the freezing process in the NWF model and WWF model are shown in Figure 13. The frost heave strain

increases in both the NWF model and the WWF model as the GWL increases. It should be noted that the difference in frost heave strain between the NWF and WWF models at different GWL is 8.448% and 6.68%, respectively. Where 8.448% corresponds to GWL at 0mm, and 6.68% corresponds to GWL at 60mm. In other words, the depression effect of frost heave by WF decreases as GWL increases. The following reasons may account for the impact of GWL on frost heave strain. When GWL increases, the soil becomes more saturated. Consequently, soil permeability increases in such circumstances. This results in a significant increase in the water flow rate and the frost heave. Further, the higher the saturation, the greater the latent heat amount available in the soil, making it more difficult for the soil to freeze. In the WWF model, a higher GWL lowers the distance between WF and GWL, therefore making it significantly more difficult to drain all the excess water immediately, in other words, reducing drain water efficiency. Additionally, a higher GWL will also lead to greater soil saturation, which in turn creates a more significant frost heave strain during the freezing process.

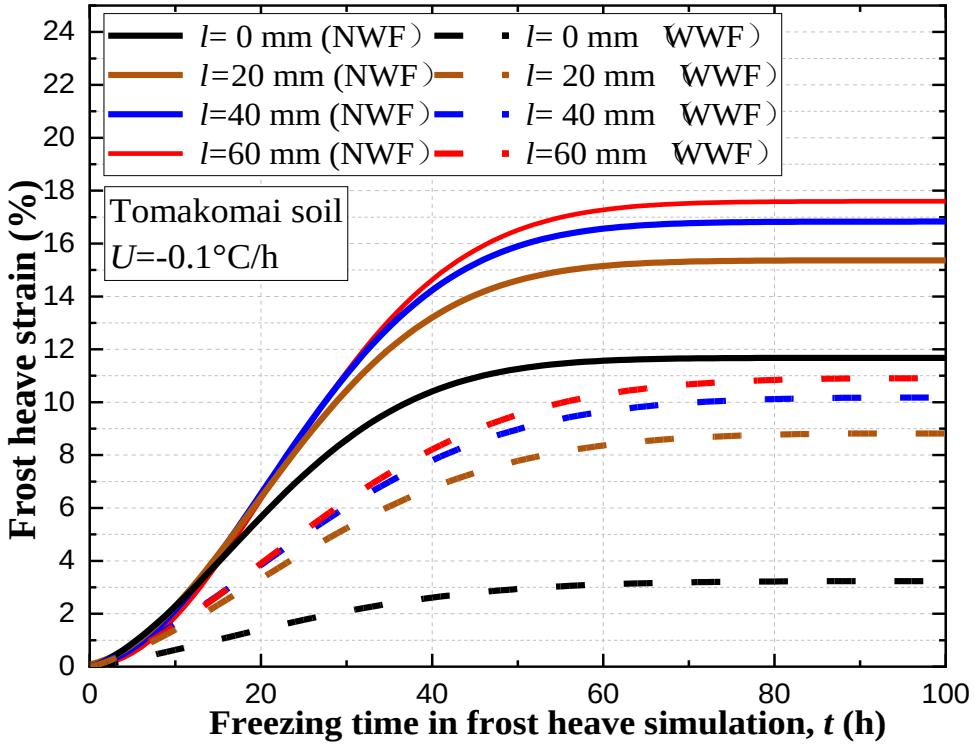

Figure 5.12 Effect of GWL on frost heave and WF depressing effect.

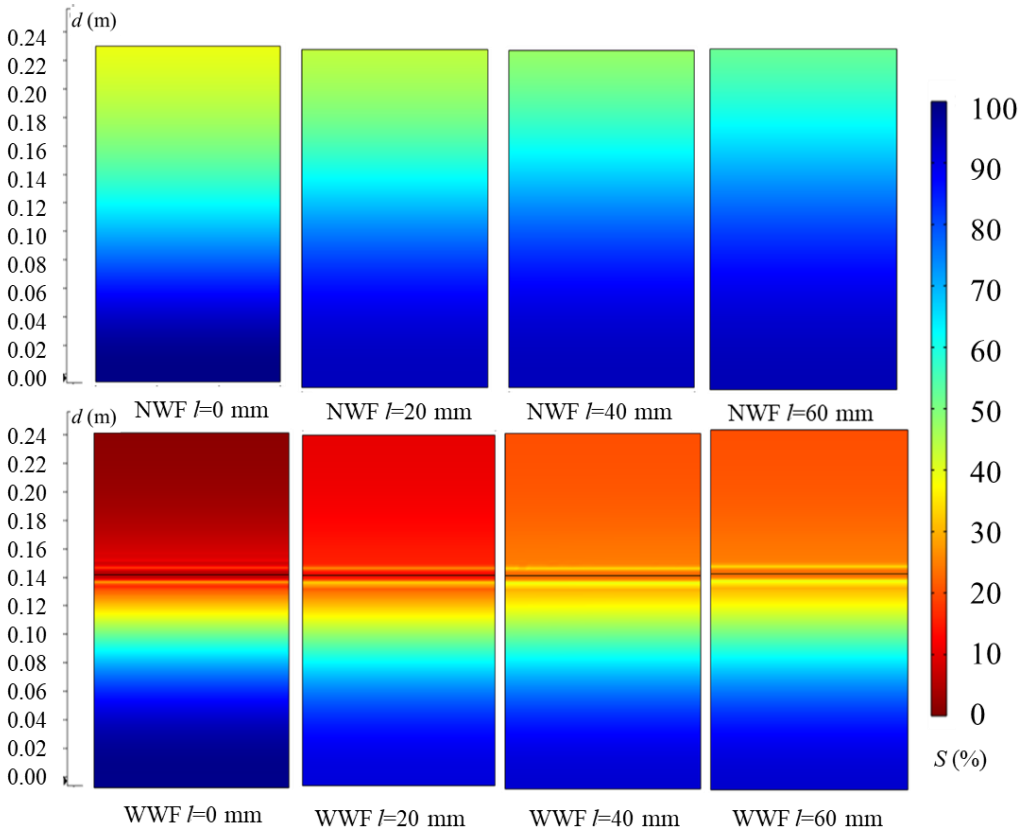

Figure 5.13 Effect of GWL on frost heave and WF depressing effect.

5.4 Summary

This chapter has proposed an evaporation model, which combined with a THM coupled FE model. The proposed model can evaluate the WF inhibition effect of frost heave under different situations and describe the influence of the surrounding environment, such as the saturation and temperature of the soil, on WF. The validity of the proposed model was examined by comparing the simulation results to the experimental results. As a result, it was verified that the proposed model could sufficiently predict the temperature, moisture, and frost heave of the soil column in the model test, and that the proposed model could simulate the suppression effect of WF on frost heave under different conditions.

The results from both the experimental and numerical simulations demonstrate that WF can effectively inhibit the occurrence of frost heave. This indicates that the pro-posed model is able to reproduce the transient evaporation process of WF during freezing, whose rate changes in accordance with the soil saturation and temperature, and that it can simulate the inhibition effect of WF on frost heave under different conditions. Moreover, the soil type, GWL, and cooling rate affect the inhibition effect of WF on frost heave strain in frost-susceptible soils. The WF was more effective in reducing

frost heave on sandy soils than on clay soils. For the same freezing time, a higher freezing rate tends to cause less frost heave, and the inhibition effect of WF on frost heave is correspondingly weakened. Moreover, when the GWL is increased, it also reduces the effectiveness of WF in inhibiting frost heave.

6 APPLICATIONS OF THM COUPLED MODEL IN PAVEMENT

In order to verify the reliability and applicability of the proposed model, this section simulated the field test with the proposed theoretical model. The experiments include temperature, water content and frost heave changes in winter for the sections with WF installed and without WF installed.

6.1 Overview

To investigate the effectiveness of frost heave inhibition by installing WF, a test pavement section installed with WF was constructed by the civil engineering research institute for cold region (CERI) on an embankment at the Tomakomai winter test track. The field measurements were collected between 2019.10.9 and 2020.3.13, which covers the months of autumn through spring. The pavement structure is shown in Figure 6.1. While the test pavement is 4.0 m in width and 3.7 m in length, the WF is buried within the roadbed, approximately 72 cm below the surface of the pavement. In the test pavement, the surface layer was constructed of dense graded asphalt concrete with a thickness of 12 cm, and the subgrade layer was constructed of recycled 40 mm graded aggregates (RC-40) and SFG with a thickness of 40 cm. The WF was buried 20 cm below the surface of the road. This is due to the fact that the WF can drain water more efficiently from the upper layer. In other words, effective water drainage from the frost susceptible roadbed would lead to more efficient frost heave inhibition. As can be seen in Figure 6.1, The thermocouples, moisture sensors and tensors are installed in the soil during the freezing process to monitor changes in temperature, moisture content, and matrix suction.

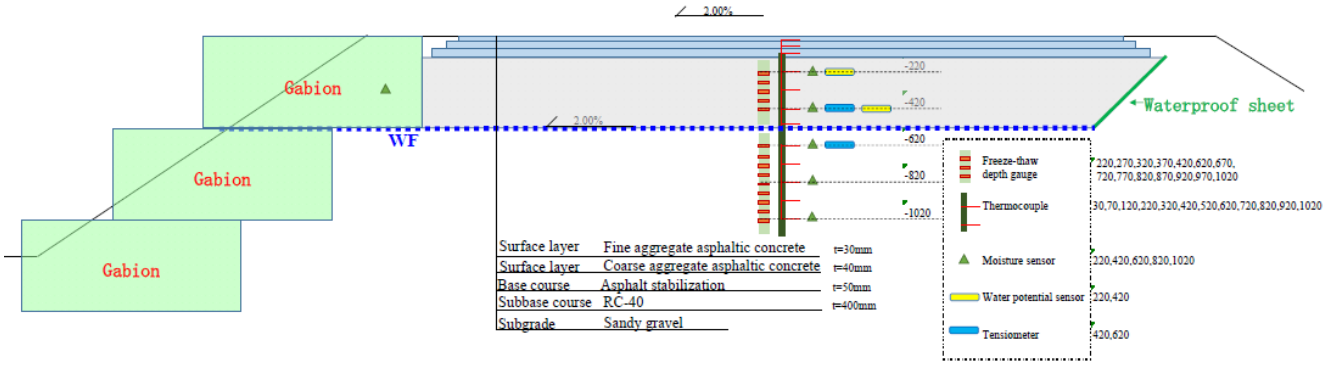

Figure 6.1 Schematic of the WF installed test pavement structure.

An area of 0.3 m wide was exposed to the atmosphere on the left end of the WF to allow for water evaporation into the atmosphere or drain out along the slope. Unlike the previously proposed WF-soil drainage system (Figure 6.2(a)), CERI has made improvements to the WF-soil drainage system (Figure 6.2(b)), which are as follows. First, unlike the conventional horizontal paving, WF incorporates a 2% slope in the new pavement structure paving, which allows WF to more easily drain the water absorbed from the surrounding soil along the slope. Second, the WF on the exposed side of the roadbed soil was held in place with a stone dragon. In conventional WF installation, the exposed WF directly on the shoulder of the road can cause the water discharged from the WF to flow back.

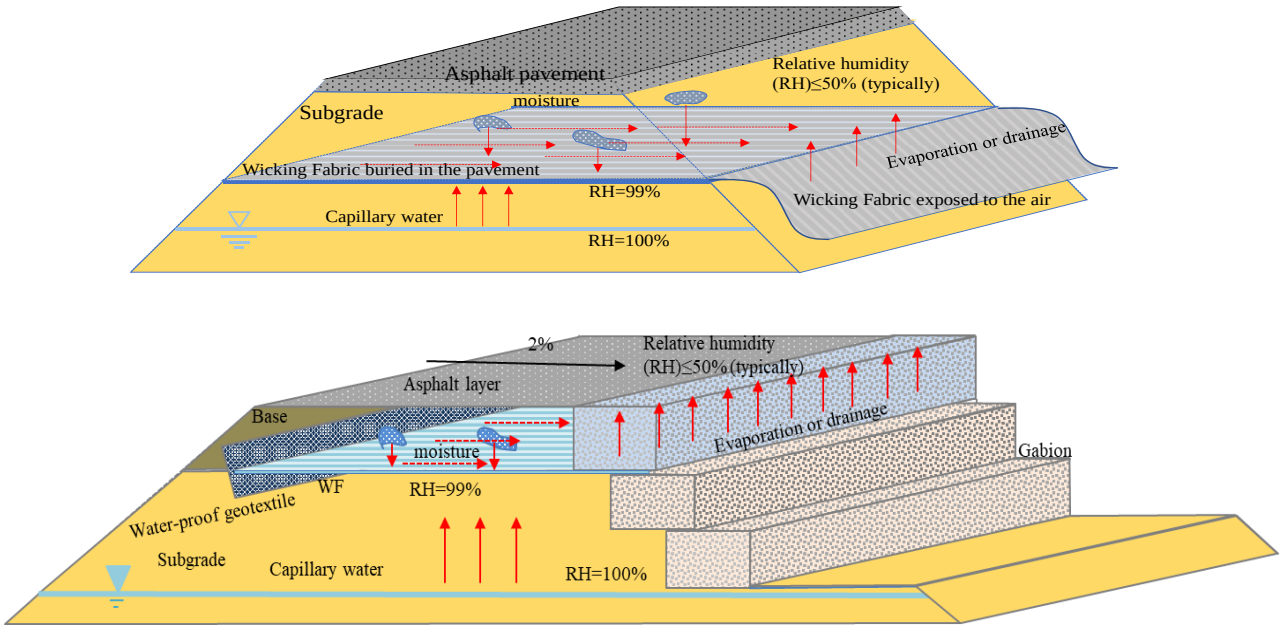

Figure 6.2 WF-soil drainage system diagram (a) of conventional way; (b) proposed by CERI.

In Figure 6,3, the ongoing pavement construction is depicted. The specific construction procedures are as follows,

(a) Remove the existing pavement surface and excavate the pavement down to the subgrade.

(b) Bury the sensors at the pre-determined depth below the WF and backfill the pavement with subgrade soil.

(c) Level the subgrade surface before installing the WF. Subsequently, backfill the pavement with subbase material.

(d) Installing the sensors at the predetermined depth in the subbase course above the WF.

(e) Constructing and compacting the slope. Afterwards, backfill the pavement with the subbase material.

(f) Following the completion of the slope and the base course has been compacted to 95% compaction, construct the base layer followed by the surface layer.

Figure 6.3 The construction process of installing WF.

6.2 Result and analysis

This section aims to establish a numerical model using the theoretical framework outlined in the previous section and the above-mentioned test section as a prototype. This proposed numerical model is used to investigate the effects of installing WF on temperature development, water content variation and frost heave deformation during the freezing process.

6.2.1 Simulation model and boundary conditions

The size of the sample, boundary conditions, and mesh of the two-dimensional model are presented in Figure 6.4. The water content near the WF varies significantly during the freezing process. Thus, in the WWF model, refined grid was adopted near the WF. There are six observation points located at the height (d) of 22 cm, 32 cm, 42 cm, 52 cm, 62 cm and 72 cm away from the pavement surface, respectively. Besides, the assumption of 2D plane strain was made, and 2723 quadrilateral cells were utilized in NWF model, the 4378 quadrilateral cells were utilized in NWF model to mesh the numerical model.

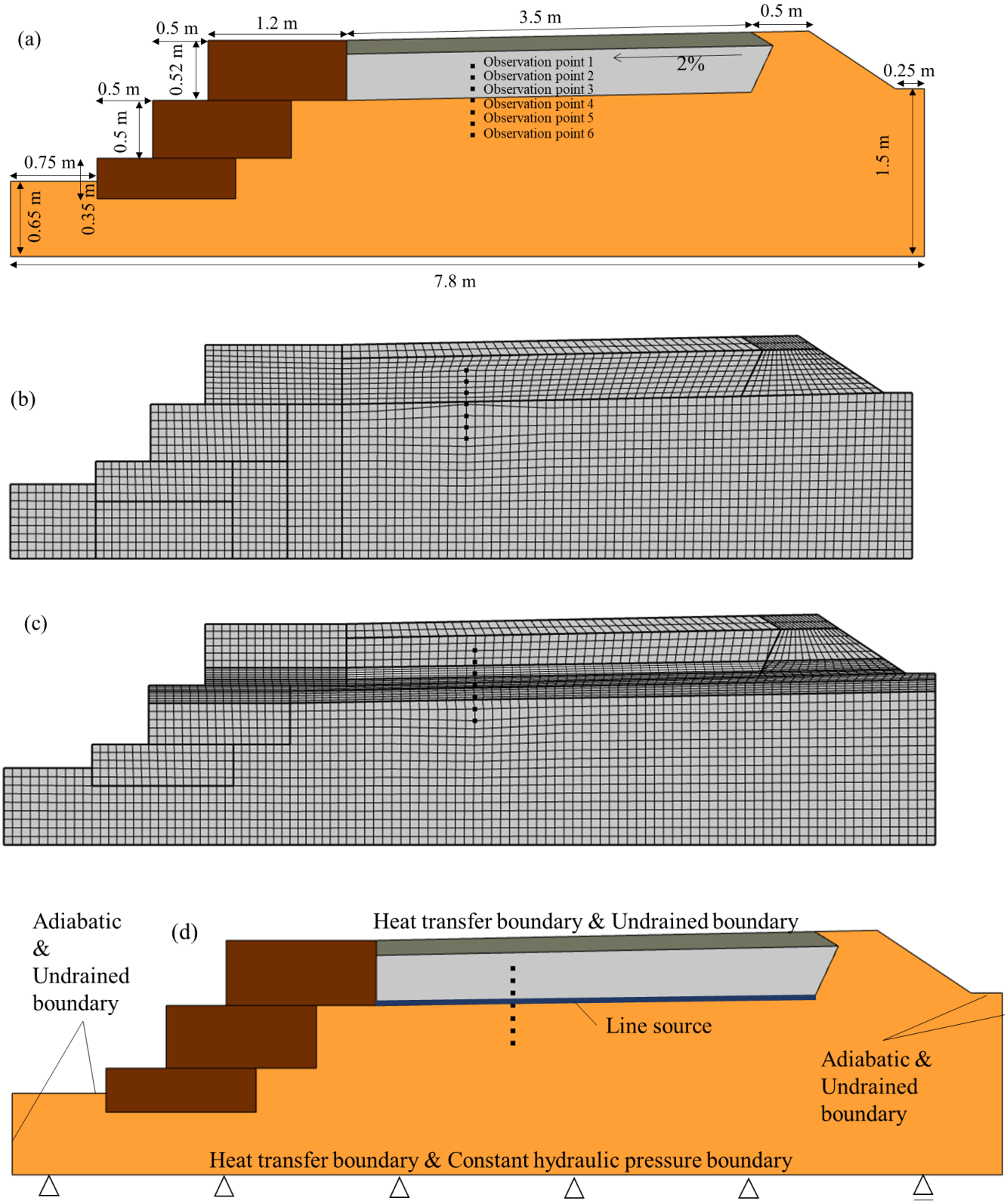

Figure 6.4 (a) Schematic of the pavement geometry; (b) Meshing schematic of the NWF pavement model; (c) Meshing schematic of the WWF pavement model; (d) Schematic of the boundary conditions.

The initial boundary conditions of the NWF model were set as follows. The base surface was fixed. The boundaries which perpendicular to the ground were fixed horizontally, the boundaries which paralleled to the ground were fixed vertically in the mechanical field. The hydrostatic pressures were applied to the base surface to maintain a constant GWL; Impermeable boundaries were applied to all the other boundaries in the hydraulic field. The exposed pavement surfaces are set with the time-dependent heat transfer boundary conditions, the temperature applied at the pavement surface is shown in Figure 6.5, for the other boundaries are set as adiabatic boundary condition in thermal field. Except for the suction boundary caused by WF, the boundary conditions for the WWF model are the same as those for the NWF model. As shown in Figure 6.4(d), the evaporation model (Eq. 3.30), working as a line source, has been applied to WF to simulate the drainage process caused by WF. The water absorption process occurs in this scenario at the WF buried within the specimen. and the material properties used in this model are shown in the Table 6.1.

Table 6.1 Soil properties used in the numerical simulations.

Abbreviation/ symbol	Parameter	Value				Unit
		As layer	Subbase course (RC-40)	Subgrade (Tomakomai soil)	Gabion	
C_s	Volumetric heat capacity	1.9E6	1.3E6	8.59E5	7.7E6	$J/m^3 \cdot K$
λ_s	Thermal conductivity of the soil mixture	1.448	0.83	1.61	2.13	$W/(m \cdot K)$
χ	Material parameters accounting for the particle shape effect	0.75	0.75	0.75	0.75	$W/(m \cdot K)$
η	Material parameters accounting for the particle shape effect	1.2	1.2	1.2	1.2	1
ρ_d	Dry density of soil particles	781.7	4529.41	1200	4529.41	Kgm^{-3}
n	Porosity	0.04	0.21	0.55	0.32	1
T_m	Final freezing temperature at	273.05	272.95	273.05	273.05	K

	atmospheric pressure					
α_{vg}	Van-Genuchten-Mualem fitting parameter	0	1340	25.02	6600	MPa^{-1}
λ_{vg}	Van-Genuchten- Muale fitting parameter	0	1.87	1.54	2.56	1
S_s	Saturated degree of saturation	0	100	95.1	100	%
S_r	Residual degree of saturation	0	13.9	33.5	6.9	%
k_s	Saturated water hydraulic conductivity	3.6E-5	9.1E-1	9.16E-9	5.4	ms^{-1}
α_{Tu}	Thermal expansion coefficient	3E-5	1.0E-5	1.2E-6	1.2E-5	K^{-1}
E	Young's modulus of soil	10000	45.3	8.5	45.3	MPa
H	Modulus related to matric potential	7653	7653	7653	7653	m
υ	Poisson's ratio	0.35	0.35	0.4	0.35	1

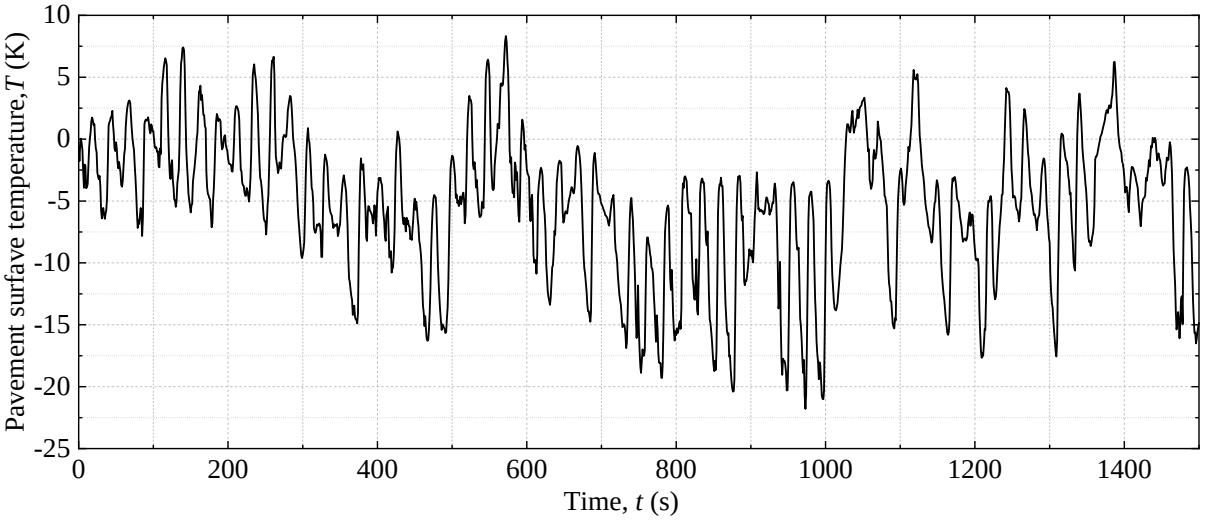

Figure 6.5 The measured temperature at the pavement surface.

The temperature and volumetric water content are shown in Figure 6.6.

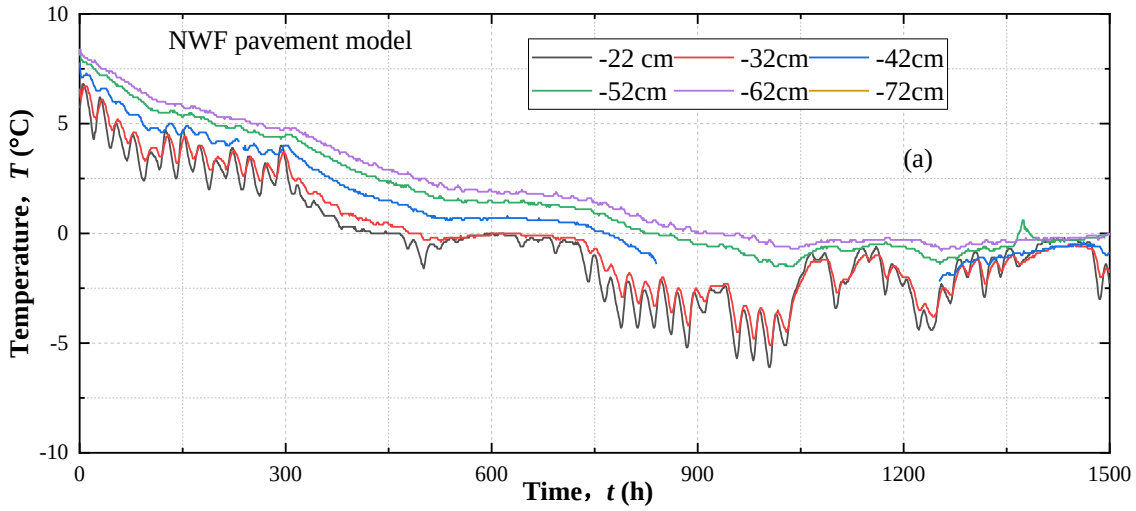

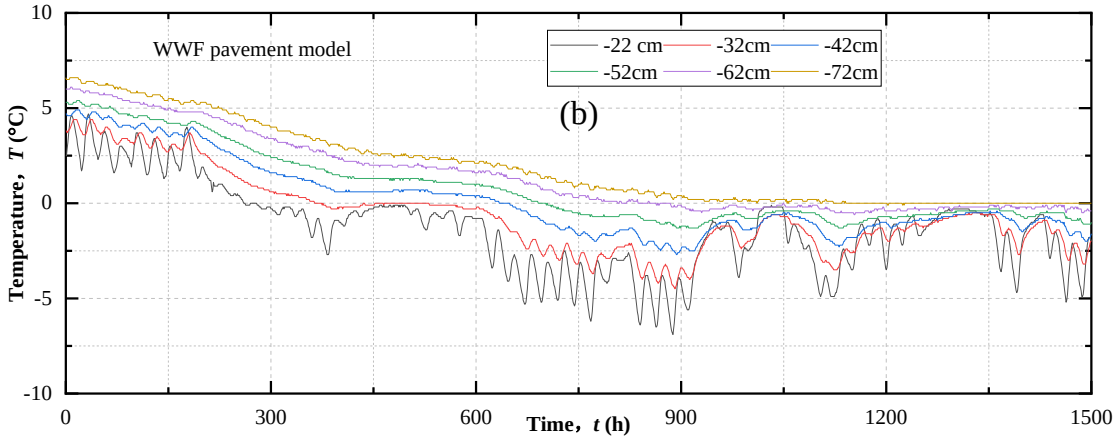

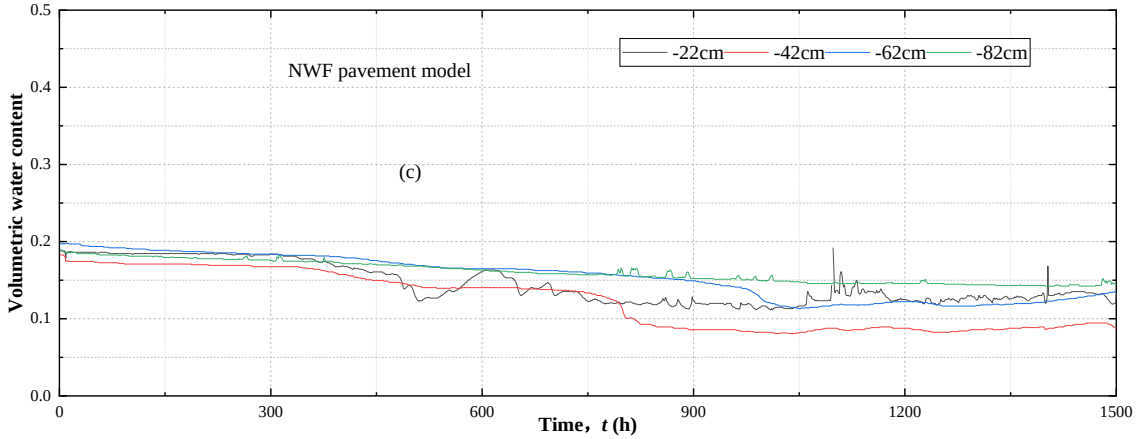

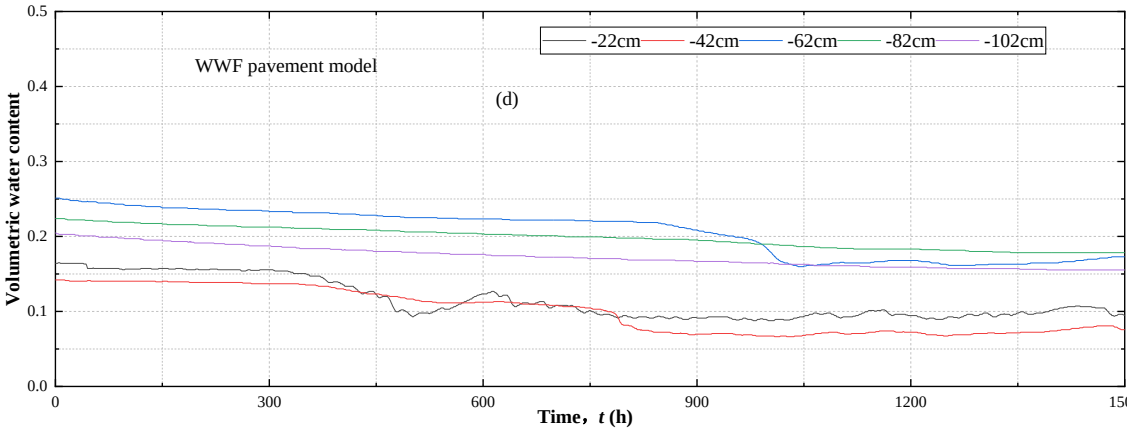

Figure 6.6 The measured data at the observation point: (a) the temperature variation of NWF pavement model during the measured period at observation points, (b) the temperature variation of WWF pavement model during the measured period at observation points, (c) the volumetric water content variation of NWF pavement model during the measured period at observation points, (d) the volumetric water content variation of NWF pavement model during the measured period at observation points.

6.2.2 Simulation results

The following section compares simulation results for pavements with and without WF, including temperature, saturation, and frost heave deformation during freezing. The temperature and water content distribution on each observation point for the NWF and WWF pavement model are shown as follow.

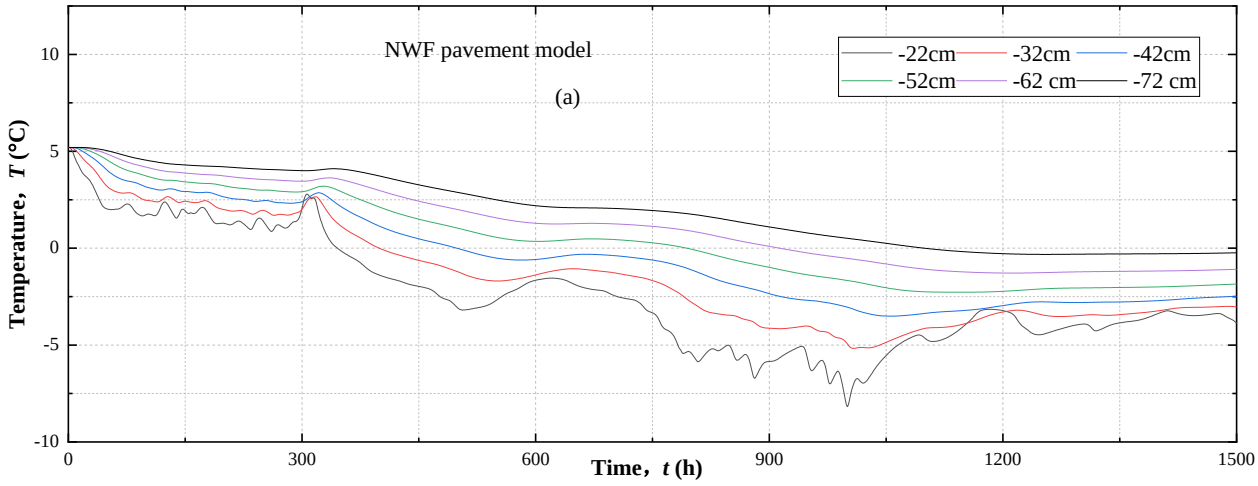

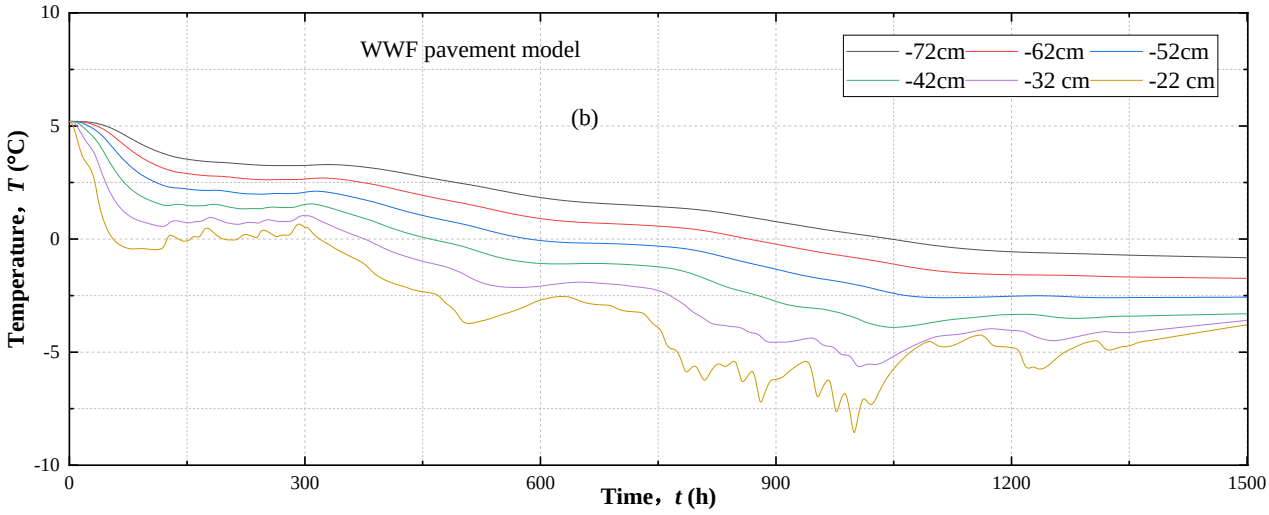

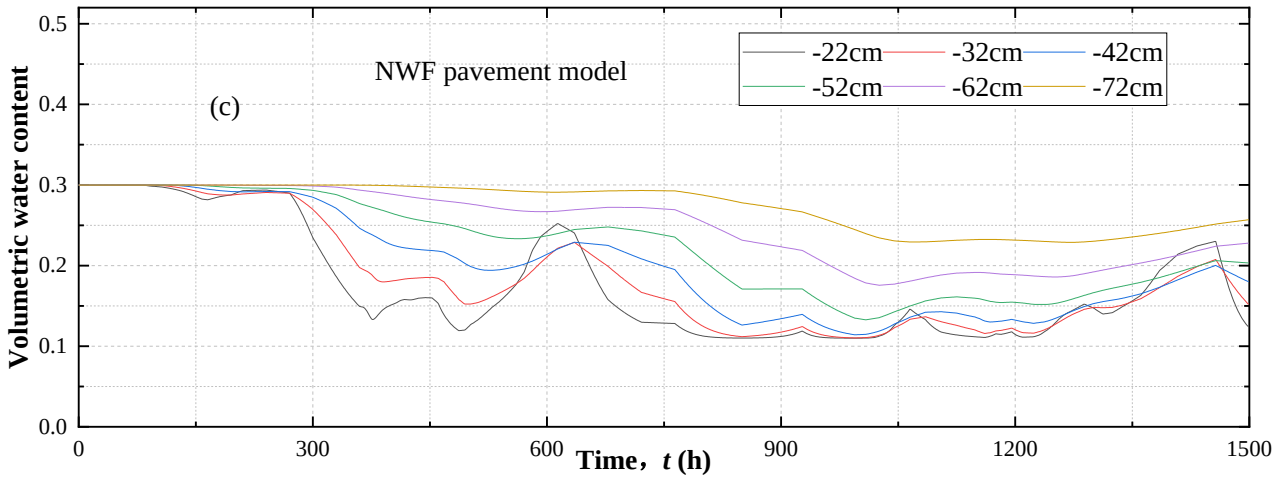

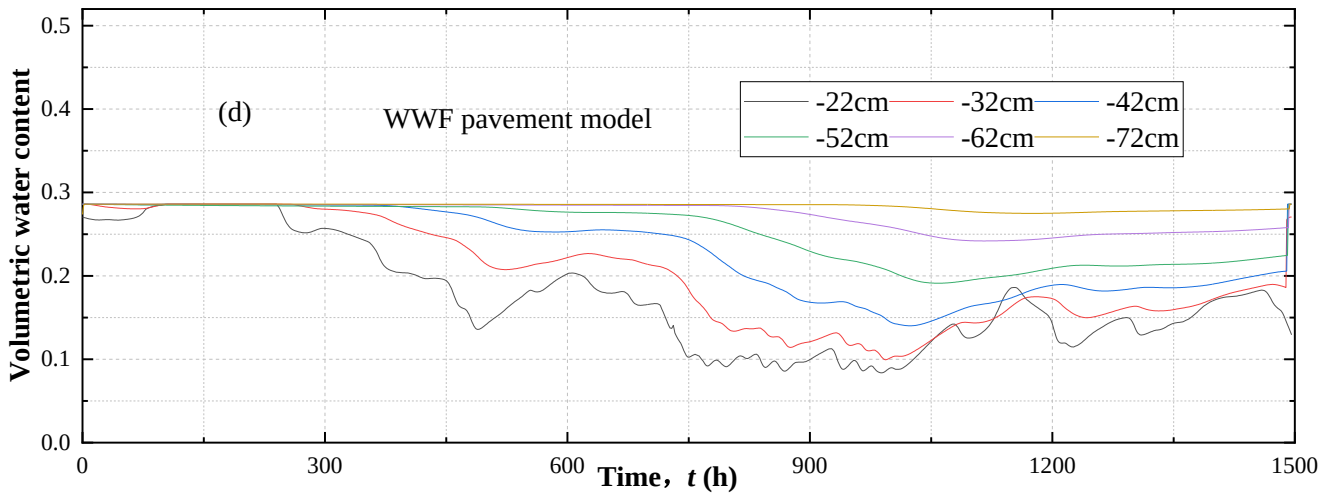

Figure 6.7 The simulated results at the observation point: (a) the temperature variation of NWF pavement model at observation points, (b) the temperature variation of WWF pavement model at observation points, (c) the

volumetric water content variation of NWF pavement model at observation points, (d) the volumetric water content variation of NWF pavement model at observation points.

The numerical simulation is close to the monitoring resultsin terms of temperature variation during the freezing process at each monitoring point. The observation point 1, which is closest to the surface (the cooling end), cools most rapidly. However, the simulation results for observation points 4, 5, 6, and 7 are slightly higher than the measured results. This may be due to the fact that the thermal conductivity and heat capacity of WF are not considered in the simulation. In the proposed model, the water absorption process of WF is simplified to the evaporation process.

According to Figure 6-7, the numerical calculation results are consistent with the trend of the measured values. Nevertheless, there are still some differences between the numerically calculated results and the measured values, which may be due to the fact that the environment's relative humidity variation, solar radiation, and wind effects are not taken into consideration when setting the boundary conditions.

The temperature distribution of NWF model and WWF pavement model are shown in Figure 6.8. It can be seen that the temperature distribution of the two models at the end of the freezing process are approximated. It is important to note that although WF drains water from the soil effectively during the freezing process, the water and ice contents only affect the time required to drop the temperature but not the temperature distribution at the end of the freezing process.

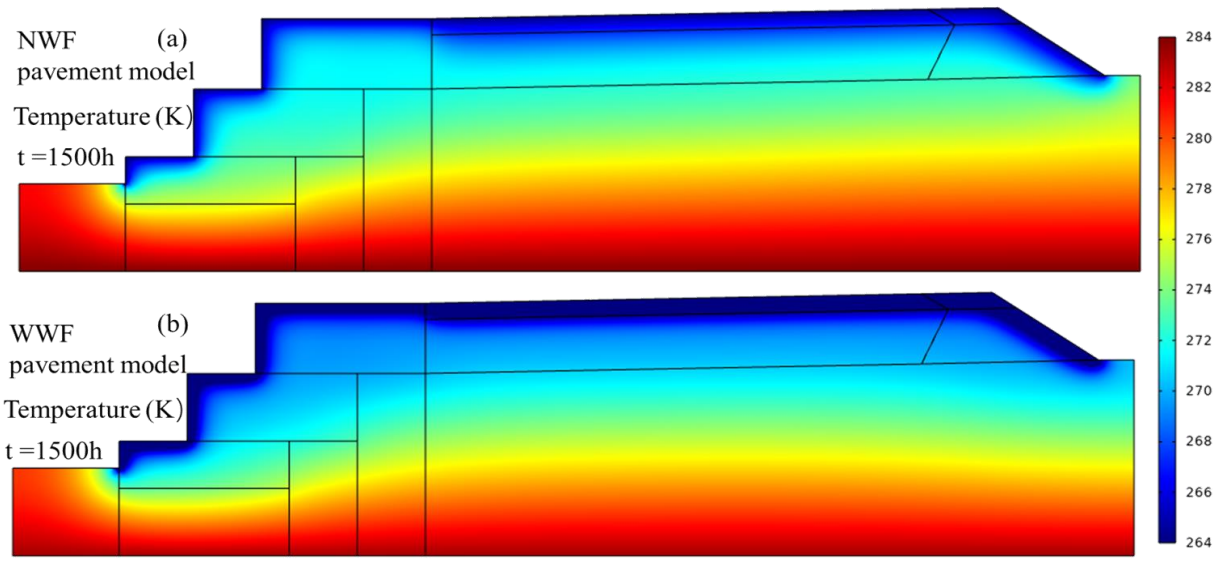

Figure 6.8 The temperature distribution of tested pavement at the end of the freezing process in (a) NWF pavement model; (b) WWF pavement model.

The saturation distribution of NWF model and WWF pavement model at the end of the freezing process are shown in Figure 6.9. As can be seen, the saturation in the WWF pavement model is significantly less than that in the NWF pavement model. Above the WF, the soil saturation decreases most dramatically, and the soil saturation around the WF decreases as well.

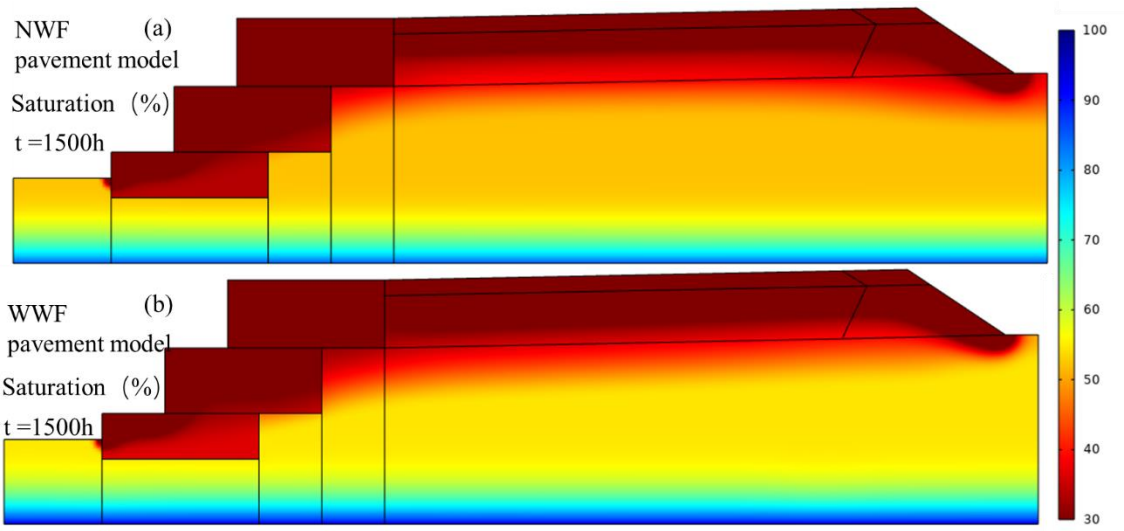

Figure 6.9 The saturation distribution of tested pavement at the end of the freezing process in (a) NWF pavement model; (b) WWF pavement model.

The frost heave deformation of the NWF model and WWF pavement model are shown in Figure 6.10. The comparison of frost heave deformation in these two different pavement structures suggests that the frost heave deformation generated in the WWF pavement model after freezing is smaller than that generated in the NWF pavement model. This is because in the WWF pavement model, the moisture is effectively evaporated by the WF. Consequently, the deformation caused by frost heave in NWF pavement model is larger than that in WWF pavement model due to water migration and accumulation.

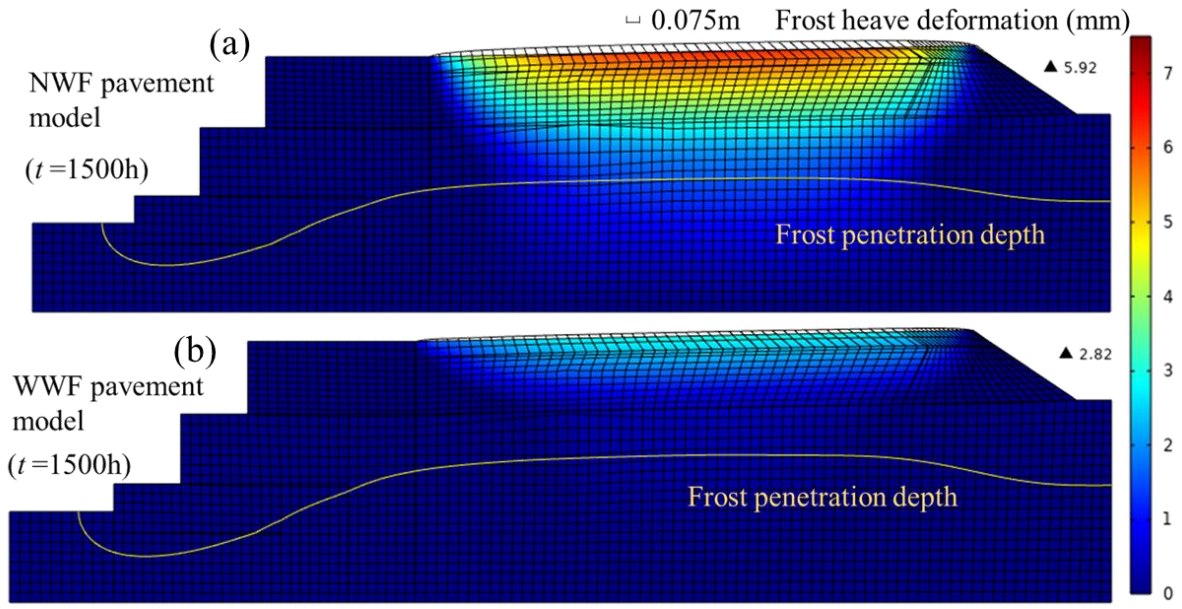

Figure 6.10 The frost heave deformation of tested pavement after freezing process in (a) NWF pavement model and (b) WWF pavement model.

6.3 Summary

This chapter presents the field test of WF and simulates the field test by employing a proposed model to evaluate its performance. The proposed model can effectively simulate the variation in temperature, saturation, and frost heave deformation on the pavement with WF during the freezing process. Comparing the simulation results of WWF and NWF models shows that, although the differences in temperature distribution after freezing are smaller, the saturation and frost heave deformations are significantly reduced in WWF model, which indicates the effectiveness of WF in inhibiting frost heave.

7 CONCLUSIONS AND RECOMMENDATIONS

This paper investigates the challenges of cold region engineering construction and maintenance with numerical simulations as the main focus, supplemented by laboratory experiments and field tests. Richards equation, heat transfer model, evaporation model, and elasticity theory are used to establish the theoretical framework for the THM coupled model. The model provides a theoretical foundation for the design, construction and maintenance of a variety of types of projects in cold regions.

The conclusions and recommendations of this study are summarized in four parts. The first part is from Chapter 3 explaining the theoretical framework of the THM model and the simplified evaporation model. The second part is from Chapter 4 detailly explaining the main finding of the study on frost heave in partially saturated soil by introducing the one-dimensional frost heave test and simulating a Multiphysics coupled numerical model and the soil properties variation in the freezing process. The third part is from Chapter 5 detailly explaining the main finding of the study on evaluation of the WF frost heave inhibition effect by conducting the model test and simulation. The fourth part is from Chapter 6 explaining the performance and practicality of the proposed model by apply the numerical model to the field test.

7.1 Conclusions

The findings from Chapter 3 can be outlined as follows:

1. This chapter presents the theoretical framework of the THM coupling model and evaporation model. Additionally, it discusses the simplification process and the scope of application for evaporation models. The proposed model can be used to simulate the freezing process of unsaturated soils.

2. The proposed THM coupled model considers water-ice phase change, heat transfer, moisture migration and frost heave deformation. The evaporation model incorporates the characteristics of water absorption and drainage in WF. Moreover, the change in water content and temperature in the soil during the freezing process may affect the efficacy of WF evaporation, so these factors are also included as part of the evaporation model.

The findings from Chapter 4 can be outlined as follows:

1. The proposed model in this chapter provide a possible way to simulate the freezing process in both saturated and unsaturated soils, and experiment conditions may greatly influence the frost heave.

2. The frost heave ratio is proportional to the initial degree of saturation, and it is inversely proportional to the cooling rate and overburden pressure. Moreover, simulation in the open system generates much more frost heave compared with that in the closed system. The proposed model can capture the main features of unsaturated soil during freezing, such as suction-induced freezing point depression, water redistribution caused by cryogenic suction gradient, and, most importantly, frost heave.

The findings from Chapter 5 can be outlined as follows:

1. This indicates that the proposed model is able to reproduce the transient evaporation process of WF during freezing, whose evaporation rate changes in accordance with the soil saturation and temperature, and that it can simulate the inhibition effect of WF on frost heave under different conditions.

2. The soil type, groundwater table, and cooling rate affect the inhibition effect of WF on frost heave deformation in frost-susceptible soils. The WF was more effective in reducing frost heave on sandy soils than on clay soils. For the same freezing time, a higher cooling rate tends to cause less frost heave, and the inhibition effect of WF on frost heave is correspondingly weakened. Meanwhile, when the groundwater table is increased, it also reduces the effectiveness of WF in inhibiting frost heave.

The findings from Chapter 6 can be outlined as follows:

1. The proposed model can effectively simulate the variation in temperature, saturation, and frost heave deformation on the pavement with WF during the freezing process.

2. Comparing the simulation results of WWF and NWF models shows that, although the differences in temperature distribution after freezing are smaller, the saturation and frost heave deformations are significantly reduced in WWF model, which indicates the effectiveness of WF in inhibiting frost heave.

7.2 Future Assignments

Although a THM coupling model was developed in this study, the draining process of WF was simplified by using the evaporation model, and the proposed model has demonstrated its validity in predicting frost heave, soil temperature, and moisture distribution. There are still a number of problems that require further investigation.

1. Only the freezing process is considered in the proposed THM model. In reality, in addition to the cracking, which may result from the freezing process, the accumulation of water from thawing may cause the pavement to weaken, resulting in pavement degradation.

2. Since the moisture migration in WF is simplified by the evaporation model, the proposed model overestimates evaporation when the contact area between WF and the dry environment is not large enough.

3. The deformation in the current model is calculated based on the assumption of small deformation and linear elasticity. The calculation of large deformation and plastic deformation of the soil is still not realized.

4. In unsaturated soils, migration of gaseous water and the formation of a compartmentalized layer can lead to water accumulation and pavement strength reduction in the presence of substantial amounts of water and rapid cooling. The model presented in this study does not consider gaseous water migration.

LIST OF REFERENCES

1. Anderson, D. M., A. R. Tice, and H. L. McKim, 1973, The unfrozen water and the apparent specific heat capacity of frozen soils: International Conference on Permafrost, 2d, Yakutsk, Siberia, 1973. Papers.
2. Azevedo, M. M. de, 2016, Performance of geotextiles with enhanced drainage, Thesis: doi:10.15781/T2JM2428D.
3. Bahador, M., T. M. Evans, and M. A. Gabr, 2013, Modeling Effect of Geocomposite Drainage Layers on Moisture Distribution and Plastic Deformation of Road Sections: Journal of Geotechnical and Geoenvironmental Engineering, v. 139, no. 9, p. 1407–1418, doi:10.1061/(ASCE)GT.1943-5606.0000877.
4. Beskow, G. Soil freezing and frost heaving with special application to roadsand railroads. *Swed. Geol. Surv. Yearb.* **1935**, *26*, 375 (In Swedish)
5. Briggs, L. J., 1897, The mechanics of soil moisture: Washington, Gov't print. off, 36 p., p. 1–36, doi:10.5962/bhl.title.43273.
6. Brooks, R. H., A. T. Corey, Colorado State University, and Hydrology and Water Resources Program, 1964, Hydraulic properties of porous media: Fort Collins, Colorado State University, [Hydrology and Water Resources Program.
7. Cornell Local Roads Program, C.U. Those Cracks on the Edge of the Road What Causes Them 2008 [cited 2017 September 10, 2017]; Available from: http:// www.clrp.cornell.edu/ nuggets_and_nibbles/ articles/2008/cracks.html.
8. Chamberlain, E. J., 1981, Frost Susceptibility of Soil, Review of Index Tests,: COLD REGIONS RESEARCH AND ENGINEERING LAB HANOVER NH.
9. Côté, J., and J.-M. Konrad, 2005, A generalized thermal conductivity model for soils and construction materials: Canadian Geotechnical Journal, v. 42, no. 2, p. 443–458, doi:10.1139/t04-106.
10. Dall'Amico, M., S. Endrizzi, S. Gruber, and R. Rigon, 2011, A robust and energy-conserving model of freezing variably-saturated soil: The Cryosphere, v. 5, no. 2, p. 469–484, doi:10.5194/tc-5-469-2011.
11. De Vries, D. A., 1958, Thermal properties of soils: Amsterdam, Physics of the plant environment, 210–235 p.
12. Derjaguin, B. V., and N. V. Churaev, 1978, The theory of frost heaving: Journal of Colloid and Interface Science, v. 67, no. 3, p. 391–396, doi:10.1016/0021-9797(78)90227-8.
13. Dirksen, C., and R. D. Miller, 1966, Closed-System Freezing of Unsaturated Soil: Soil Science Society of America Journal, v. 30, no. 2, p. 168–173, doi:10.2136/sssaj1966.03615995003000020010x.
14. Duquennoi, C., M. Fremond, and M. Levy, 1989, Modelling of thermal soil behaviour: no. 95, p. 895–915.
15. Edgar, T. V., R. Mathis, T. McGary, and J. C. Potter, 2014, Frost Heave Mitigation Using Structural Polymer Injection, 14–1029.
16. Edlefsen, N., and A. Anderson, 1943, Thermodynamics of soil moisture: Hilgardia, v. 15, no. 2, p. 31–298.
17. Everett, D. H., 1961, The thermodynamics of frost damage to porous solids: Transactions of the Faraday Society, v. 57, p. 1541, doi:10.1039/tf9615701541.
18. Fayer, M. J., 2000, UNSAT-H Version 3.0:Unsaturated Soil Water and Heat Flow Model Theory, User Manual, and Examples, 820201000: Pacific Northwest National Lab. (PNNL), Richland, WA (United States), doi:10.2172/781853.
19. Flerchinger, G. N., and K. E. Saxton, 1989, Simultaneous heat and water model of a freezing snow-residue-soil system II. Field verification: American Society of Agricultural and Biological Engineers, v. 32, no. 2, p. 573–576.
20. Fredlund, M. D., D. Tran, and D. G. Fredlund, 2016, Methodologies for the Calculation of Actual Evaporation in Geotechnical Engineering: International Journal of Geomechanics, v. 16, no. 6, p. D4016014, doi:10.1061/(ASCE)GM.1943-5622.0000730.
21. Fredlund, D. G., A. Xing, and S. Huang, 1994, Predicting the permeability function for unsaturated soils using the soil-water characteristic curve: Canadian Geotechnical Journal, v. 31, no. 4, p. 533–546, doi:10.1139/t94-062.
22. Fremond, M., and M. Mikkola, 1991a, Thermomechanical modelling of freezing soil: p. 17–24.
23. Fremond, M., and M. Mikkola, 1991b, Thermomechanical modelling of freezing soil: p. 17–24.
24. Gaskin, P. N., and H. B. Sutherland, 1973, Pore water and heaving pressures developed in partially frozen soils: p. 409.
25. Gens, A., and S. Olivella, 2001, THM phenomena in saturated and unsaturated porous media: Revue Française de Génie Civil, v. 5, no. 6, p. 693–717, doi:10.1080/12795119.2001.9692323.
26. van Genuchten, M. Th., 1980, A Closed-form Equation for Predicting the Hydraulic Conductivity of Unsaturated Soils: Soil Science Society of America Journal, v. 44, no. 5, p. 892–898, doi:10.2136/sssaj1980.03615995004400050002x.
27. Gieselman, H., 2007, Effect of a hydrophobic layer on the upward movement of water under freezing conditions, Master of Science: Ames, Iowa State University, Digital Repository, p. 6950862, doi:10.31274/rtd-180813-7420.
28. Guo, J., J. Han, X. Zhang, and Z. Li, 2019, Evaluation of Moisture Reduction in Aggregate Base by Wicking Geotextile using Soil Column Tests: Geotextiles and Geomembranes, v. 47, no. 3, p. 306–314, doi:10.1016/j.geotexmem.2019.01.014.
29. Guo, Y., C. Lin, W. Leng, and X. Zhang, 2022, Laboratory evaluation of different geosynthetics for water drainage: Geosynthetics International, doi:10.1680/jgein.21.00005.

30. Guo, J., F. Wang, X. Zhang, and J. Han, 2017, Quantifying Water Removal Rate of a Wicking Geotextile under Controlled Temperature and Relative Humidity: Journal of Materials in Civil Engineering, v. 29, no. 1, p. 04016181, doi:10.1061/(ASCE)MT.1943-5533.0001703.
31. Guymon, G., R. Berg, and T. Hromadka, 1993, Mathematical model of frost heave and thaw settlement in pavements: NASA STI/Recon Technical Report N.
32. Guymon, G. L., and J. N. Luthin, 1974, A coupled heat and moisture transport model for Arctic soils: Water Resources Research, v. 10, no. 5, p. 995–1001, doi:10.1029/WR010i005p00995.
33. Hachem, E., and A. Ghassan, 2018, Moisture drainage under unsaturated soil conditions with the aid of enhanced lateral drainage (ELD) geotextiles, Thesis: doi:10.15781/T21R6NK4N.
34. Han, J., and J. Guo, 2017, Geosynthetics used to stabilize vegetated surfaces for environmental sustainability in civil engineering: Frontiers of Structural and Civil Engineering, v. 11, no. 1, p. 56–65, doi:10.1007/s11709-016-0380-8.
35. Han, J., and X. Zhang, 2014, Recent advances in the use of geosynthetics to enhance sustainability of roadways, in Nakhon Ratchasima, Thailand.
36. Hansson, K., J. Šimůnek, M. Mizoguchi, L.-C. Lundin, and M. Th. van Genuchten, 2004, Water Flow and Heat Transport in Frozen Soil: Numerical Solution and Freeze–Thaw Applications: Vadose Zone Journal, v. 3, no. 2, p. 693–704, doi:10.2136/vzj2004.0693.
37. Harlan, R. L., 1973a, Analysis of coupled heat-fluid transport in partially frozen soil: Water Resources Research, v. 9, no. 5, p. 1314–1323, doi:10.1029/WR009i005p01314.
38. Harlan, R. L., 1973b, Analysis of coupled heat-fluid transport in partially frozen soil: Water Resources Research, v. 9, no. 5, p. 1314–1323, doi:10.1029/WR009i005p01314.
39. Henry, K., and R. Holtz, 2011, Geocomposite capillary barriers to reduce frost heave in soils: Canadian Geotechnical Journal, v. 38, p. 678–694, doi:10.1139/cgj-38-4-678.
40. Holtz, R. D., W. D. Kovacs, and T. C. Sheahan, 1981, Introduction to Geotechnical Engineering: Englewood Cliffs, Prentice-Hall.
41. Ishikawa, T., I. Kijiya, T. Tokoro, and S. Akagawa, 2015, Frost heave behavior of unsaturated soils under low overburden pressure and its estimation: Journal of Japan Society of Civil Engineers, Ser. E1 (Pavement Engineering), v. 70, no. 3.
42. Ishikawa T, Tokoro T, Akagawa S, 2015. Frost Heave Behavior of Unsaturated Soils Under Low Overburden Pressure and Its Estimation. Proceedings of GEO Quebec.
43. Jame, Y.-W., 1977, Heat and mass transfer in freezing unsaturated soil.
44. Jame, Y.-W., and D. I. Norum, 1980, Heat and mass transfer in a freezing unsaturated porous medium: Water Resources Research, v. 16, no. 4, p. 811–819, doi:10.1029/WR016i004p00811.
45. Jame, Y.-W., and D. I. Norum, 1972, Phase cdmposttion of a partially frozen soil: p. 18.
46. Janoo, V. C., and R. L. Berg, 1990, Thaw weakening of pavement structures in seasonal frost areas: Transportation Research Record, no. 1286.
47. Japanese Industrial Standards Committee. *Test Method for Density of Soil Particles JIS A 1202*; Japanese Standards Association: Tokyo, Japan, 2009. (In Japanese)
48. Japanese Industrial Standards Committee. *Test Method for Density of Soil Particles JIS A 1204*; Japanese Standards Association: Tokyo, Japan, 2009. (In Japanese)
49. Japanese Industrial Standards Committee. *Test Method for Density of Soil Particles JIS A 1210*; Japanese Standards Association: Tokyo, Japan, 2009. (In Japanese)
50. Japanese Geotechnical Society. *Japanese Geotechnical Society Standards—Laboratory Testing Standards of Geomaterials*; Maruzen Publishing Co., Ltd.: Tokyo, Japan, 2015.
51. Japanese Geotechnical Society. *JGS 0171-2009 Test Method for Frost Heave Prediction of Soils*; Japanese Geotechnical Society: Tokyo, Japan, 2009
52. Japanese Geotechnical Society. *JGS 0172-2009 Test Method for Frost Susceptibility of Soils*; Japanese Geotechnical Society: Tokyo, Japan, 2009
53. Jiang, N., W. Pan, B. Luo, L. Yan, and S. Xiang, 2014, Simultaneous unidirectional and bidirectional chaos-based optical communication using hybrid coupling semiconductor lasers: Science China Information Sciences, v. 57, no. 1, p. 1–11, doi:10.1007/s11432-012-4721-5.
54. Kinosita, S., 1989, Preventing measures against frost action in soils: no. 95, p. 733–748.
55. Konrad, J.-M., and N. R. Morgenstern, 1980a, A mechanistic theory of ice lens formation in fine-grained soils: Canadian Geotechnical Journal, v. 17, no. 4, p. 473–486, doi:10.1139/t80-056.
56. Konrad, J.-M., and N. R. Morgenstern, 1980b, A mechanistic theory of ice lens formation in fine-grained soils: Canadian Geotechnical Journal, v. 17, no. 4, p. 473–486, doi:10.1139/t80-056.
57. Konrad, J.-M., and N. R. Morgenstern, 1982a, Effects of applied pressure on freezing soils: Canadian Geotechnical Journal, v. 19, no. 4, p. 494–505, doi:10.1139/t82-053.
58. Konrad, J.-M., and N. R. Morgenstern, 1982b, Effects of applied pressure on freezing soils: Canadian Geotechnical Journal, v. 19, no. 4, p. 494–505, doi:10.1139/t82-053.

59. Konrad, J.-M., and N. R. Morgenstern, 1981a, The segregation potential of a freezing soil: Canadian Geotechnical Journal, v. 18, no. 4, p. 482–491, doi:10.1139/t81-059.
60. Konrad, J.-M., and N. R. Morgenstern, 1981b, The segregation potential of a freezing soil: Canadian Geotechnical Journal, v. 18, no. 4, p. 482–491, doi:10.1139/t81-059.
61. Koopmans, R. W. R., and R. D. Miller, 1966, Soil Freezing and Soil Water Characteristic Curves: Soil Science Society of America Journal, v. 30, no. 6, p. 680–685, doi:10.2136/sssaj1966.03615995003000060011x.
62. Lay, R. D., n.d., Development of a Frost Heave Test Apparatus, M.Sc.: 90 p.
63. Li, Z., 2021, Research on coupling of multifield in frozen soil based on hybrid mixture theory, Dissertation: Harbin Institute of Technology.
64. Li, N., B. Chen, F. Chen, and X. Xu, 2000, The coupled heat-moisture-mechanic model of the frozen soil: Cold Regions Science and Technology, v. 31, no. 3, p. 199–205, doi:10.1016/S0165-232X(00)00013-6.
65. Li, N., F. Chen, B. Su, and G. Cheng, 2002, Theoretical frame of the saturated freezing soil: Cold Regions Science and Technology, v. 35, no. 2, p. 73–80, doi:10.1016/S0165-232X(02)00029-0.
66. Li, S., M. Zhang, W. Pei, and Y. Lai, 2018, Experimental and numerical simulations on heat-water-mechanics interaction mechanism in a freezing soil: Applied Thermal Engineering, v. 132, p. 209–220, doi:10.1016/j.applthermaleng.2017.12.061.
67. Li, S., M. Zhang, Y. Tian, W. Pei, and H. Zhong, 2015, Experimental and numerical investigations on frost damage mechanism of a canal in cold regions: Cold Regions Science and Technology, v. 116, p. 1–11, doi:10.1016/j.coldregions.2015.03.013.
68. Lin, C., W. Presler, X. Zhang, D. Jones, and B. Odgers, 2017, Long-Term Performance of Wicking Fabric in Alaskan Pavements: Journal of Performance of Constructed Facilities, v. 31, no. 2, p. D4016005, doi:10.1061/(ASCE)CF.1943-5509.0000936.
69. Lin, C., X. Zhang, and J. Han, 2019, Comprehensive Material Characterizations of Pavement Structure Installed with Wicking Fabrics: Journal of Materials in Civil Engineering, v. 31, no. 2, p. 04018372, doi:10.1061/(ASCE)MT.1943-5533.0002587.
70. Liu, Z. (Leo), 2018, Multiphysics in Porous Materials, in Z. (Leo) Liu, ed., Multiphysics in Porous Materials: Cham, Springer International Publishing, p. 29–34, doi:10.1007/978-3-319-93028-2_4.
71. Liu, Z., Y. Sun, and X. (Bill) Yu, 2012, Theoretical Basis for Modeling Porous Geomaterials under Frost Actions: A Review: Soil Science Society of America Journal, v. 76, no. 2, p. 313–330, doi:10.2136/sssaj2010.0370.
72. Liu, Q., Z. Wang, Z. Li, and Y. Wang, 2020, Transversely isotropic frost heave modeling with heat–moisture–deformation coupling: Acta Geotechnica, v. 15, no. 5, p. 1273–1287, doi:10.1007/s11440-019-00774-1.
73. Liu, Z., and X. Yu, 2011, Coupled thermo-hydro-mechanical model for porous materials under frost action: theory and implementation: Acta Geotechnica, v. 6, no. 2, p. 51–65, doi:10.1007/s11440-011-0135-6.
74. Lu, J. G., M. Y. Zhang, and X. Z. Zhang, 2017, Status and progress of research on hydrothermal coupling in frozen soil: Journal of Glaciology and Geocryology, v. 39, no. 1, p. 102–111.
75. Luo, B., T. Ishikawa, T. Tokoro, and H. Lai, 2017, Coupled Thermo-Hydro-Mechanical Analysis of Freeze–Thaw Behavior of Pavement Structure over a Box Culvert: Transportation Research Record, v. 2656, no. 1, p. 12–22, doi:10.3141/2656-02.
76. Martin, R. T., 1959, Rhythmic ice banding in soil: Highway Research Board Bulletin, no. 218.
77. Mellor, M., and C. R. R. and E. Laboratory (U.S.), 1970, Phase Composition of Pore Water in Cold Rocks: Corps of Engineers, U.S. Army, Cold Regions Research and Engineering Laboratory, 72 p.
78. Miller, R. D., 1972, Freezing and heaving of saturated and unsaturated soils, in Highway Research Record.
79. Miller, J. S., and W. Y. Bellinger, 2003, Distress identification manual for the long-term pavement performance program: United States. Federal Highway Administration. Office of Infrastructure ….
80. Mu, S., and B. Ladanyi, 1987, Modelling of coupled heat, moisture and stress field in freezing soil: Cold Regions Science and Technology, v. 14, no. 3, p. 237–246, doi:10.1016/0165-232X(87)90016-4.
81. Mualem, Y., 1976, A new model for predicting the hydraulic conductivity of unsaturated porous media: Water Resources Research, v. 12, no. 3, p. 513–522, doi:10.1029/WR012i003p00513.
82. Nakamura, D., T. Suzuki, T. Goto, H. Kim, Y. Ito, and S. Yamashita, 2011, Changes in the permeability coefficient and the void ratio of compacted soil by the effect of freeze-thaw cycles: Journal of Japan Society of Civil Engineers, Ser. C (Geosphere Engineering), v. 67, p. 264–275, doi:10.2208/jscejge.67.264.
83. Nakano, Y., and J. Brown, 1971, Effect of a Freezing Zone of Finite Width on the Thermal Regime of Soils: Water Resources Research, v. 7, no. 5, p. 1226–1233, doi:10.1029/WR007i005p01226.
84. Nassar, I. N., and R. Horton, 1992, Simultaneous Transfer of Heat, Water, and Solute in Porous Media: I. Theoretical Development: Soil Science Society of America Journal, v. 56, no. 5, p. 1350–1356, doi:10.2136/sssaj1992.03615995005600050004x.
85. Nassar, I. N., and R. Horton, 1989, Water Transport in Unsaturated Nonisothermal Salty Soil: II. Theoretical Development: Soil Science Society of America Journal, v. 53, no. 5, p. 1330–1337, doi:10.2136/sssaj1989.03615995005300050005x.

86. Newman, G. P., and G. W. Wilson, 1997, Heat and mass transfer in unsaturated soils during freezing: Canadian Geotechnical Journal, v. 34, no. 1, p. 63–70, doi:10.1139/t96-085.
87. Nishimura, S., A. Gens, S. Olivella, and R. J. Jardine, 2009, THM-coupled finite element analysis of frozen soil: formulation and application: Géotechnique, v. 59, no. 3, p. 159–171, doi:10.1680/geot.2009.59.3.159.
88. Nixon, J. F. (Derick), 1991, Discrete ice lens theory for frost heave in soils: Canadian Geotechnical Journal, v. 28, no. 6, p. 843–859, doi:10.1139/t91-102.
89. Noborio, K., K. J. McInnes, and J. L. Heilman, 1996, Two-Dimensional Model for Water, Heat, and Solute Transport in Furrow-Irrigated Soil: II. Field Evaluation: Soil Science Society of America Journal, v. 60, no. 4, p. 1010–1021, doi:10.2136/sssaj1996.03615995006000040008x.
90. O'Neill, K., and R. D. Miller, 1985, Exploration of a Rigid Ice Model of Frost Heave: Water Resources Research, v. 21, no. 3, p. 281–296, doi:10.1029/WR021i003p00281.
91. Peppin, S. S. L., and R. W. Style, 2013, The Physics of Frost Heave and Ice-Lens Growth: Vadose Zone Journal, v. 12, no. 1, p. vzj2012.0049, doi:10.2136/vzj2012.0049.
92. Peterson, R. A., and W. B. Krantz, 2003, A mechanism for differential frost heave and its implications for patterned-ground formation: Journal of Glaciology, v. 49, no. 164, p. 69–80, doi:10.3189/172756503781830854.
93. Rosenqvist, M., K. Fridh, and M. Hassanzadeh, 2016, Macroscopic ice lens growth in hardened concrete: Cement and Concrete Research, v. 88, p. 114–125, doi:10.1016/j.cemconres.2016.06.008.
94. Roy, M., J. Crispin, J.-M. Konrad, and G. Larose, 1992, Field study of two road sections during a freeze-thaw cycle: Transportation Research Record, no. 1362.
95. Saarelainen, S., 1992, Modelling frost heaving and frost penetration in soils at some observation sites in Finland: The SSR model: Dissertation, Dissertation: Espoo, VTT Technical Research Centre of Finland.
96. Scanlon, B. R., S. W. Tyler, and P. J. Wierenga, 1997, Hydrologic issues in arid, unsaturated systems and implications for contaminant transport: Reviews of Geophysics, v. 35, no. 4, p. 461–490, doi:10.1029/97RG01172.
97. Sheng, D., 1994, Thermodynamics of freezing soils : theory and application.
98. Sheng, D., S. Zhang, Z. Yu, and J. Zhang, 2013, Assessing frost susceptibility of soils using PCHeave: Cold Regions Science and Technology, v. 95, p. 27–38, doi:10.1016/j.coldregions.2013.08.003.
99. Shoop, S. A., and S. R. Bigl, 1997, Moisture migration during freeze and thaw of unsaturated soils: modeling and large scale experiments: Cold Regions Science and Technology, v. 25, no. 1, p. 33–45, doi:10.1016/S0165-232X(96)00015-8.
100. Siswosoebrotho, B. I., and P. Widodo, 2005, The influence of fines content and plasticity on the strength and permeability of aggregate for base course material: Proceedings of the Eastern Asia Society for Transportation Studies, v. 5, p. 12.
101. Striping, R.L. 5 Common Causes of Damaged and Cracked Asphalt: How to Prevent Damage. 2017 [cited 2017 September 5, 2017]; Available from: https://randazzoline.com/5-common-causes-damaged-cracked-asphalt-preventdamage.
102. Stuurop, J. C., S. E. A. T. M. van der Zee, C. I. Voss, and H. K. French, 2021, Simulating water and heat transport with freezing and cryosuction in unsaturated soil: Comparing an empirical, semi-empirical and physically-based approach: Advances in Water Resources, v. 149, p. 103846, doi:10.1016/j.advwatres.2021.103846.
103. Taber, S., 1929, Frost Heaving: The Journal of Geology, v. 37, no. 5, p. 428–461, doi:10.1086/623637.
104. Taber, S., 2015, The Mechanics of Frost Heaving: The Journal of Geology, doi:10.1086/623720.
105. Taber, S., 1930, The Mechanics of Frost Heaving: The Journal of Geology, v. 38, no. 4, p. 303–317, doi:10.1086/623720.
106. Taylor, G. S., and J. N. Luthin, 1978, A model for coupled heat and moisture transfer during soil freezing: Canadian Geotechnical Journal, v. 15, no. 4, p. 548–555, doi:10.1139/t78-058.
107. Teng, J., N. Yasufuku, S. Zhang, and Y. He, 2016, Modelling water content redistribution during evaporation from sandy soil in the presence of water table: Computers and Geotechnics, v. 75, p. 210–224, doi:10.1016/j.compgeo.2016.02.009.
108. Tetens, O., 1930, Uber einige meteorologische Begriffe: v. 6, p. 297–309.
109. Thomas, H. R., P. Cleall, Y.-C. Li, C. Harris, and M. Kern-Luetschg, 2009, Modelling of cryogenic processes in permafrost and seasonally frozen soils: Géotechnique, v. 59, no. 3, p. 173–184, doi:10.1680/geot.2009.59.3.173.
110. Tokoro T, Ishikawa T, Akagawa S, 2016. Temperature dependency of permeability coefficient of frozen soil. In Proceedings of GEO Vancouver, British Columbia, Canada.
111. Ueda, Y., O. Takahiro, and T. Takeshi, 2005, Study on the frost heave ratios in triaxial directions of soil based on effective stresses consideration: 土木学会論文集, no. 806, p. 67–78.
112. Vogel, T., M. Th. van Genuchten, and M. Cislerova, 2000, Effect of the shape of the soil hydraulic functions near saturation on variably-saturated flow predictions: Advances in Water Resources, v. 24, no. 2, p. 133–144, doi:10.1016/S0309-1708(00)00037-3.
113. Williams, P. J., and M. W. Smith, 1989, The Frozen Earth: Fundamentals of Geocryology: Cambridge, Cambridge University Press, Studies in Polar Research, doi:10.1017/CBO9780511564437.

114. Wu, Q., Z. Lu, Z. Tingjun, W. Ma, and Y. Liu, 2008, Analysis of cooling effect of crushed rock-based embankment of the Qinghai-Xizang Railway: Cold Regions Science and Technology, v. 53, no. 3, p. 271–282, doi:10.1016/j.coldregions.2007.10.004.
115. Yasuoka, T., T. Ishikawa, B. Luo, Y. Wu, K. Maruyama, and C. Ueno, 2022, Coupled Analysis on Frost-Heaving Depression Effect of Geosynthetics Drainage Material for Road Pavement, in E. Tutumluer, S. Nazarian, I. Al-Qadi, and I. I. A. Qamhia, eds., Advances in Transportation Geotechnics IV, Cham: Springer International Publishing, Lecture Notes in Civil Engineering, p. 509–520, doi:10.1007/978-3-030-77234-5_42.
116. Ye, Y., Z. Wang, A. Cheng, and M. Luo, 2007, Frost heave classification of railway subgrade filling material and the design of anti-freezing layer: Zhongguo Tiedao Kexue/China Railway Science, v. 28, p. 1–7.
117. Yu, X., S. Dong, and Y. Jiang, 2022, A Novel Random Finite Element Model for Frost Effects on Soils and Cold Region Pavement.
118. Yu, L., Y. Zeng, and Z. Su, 2020, Understanding the mass, momentum, and energy transfer in the frozen soil with three levels of model complexities: Hydrology and Earth System Sciences, v. 24, no. 10, p. 4813–4830, doi:10.5194/hess-24-4813-2020.
119. Zeng, Y., Z. Su, L. Wan, and J. Wen, 2011a, A simulation analysis of the advective effect on evaporation using a two-phase heat and mass flow model: Water Resources Research, v. 47, no. 10, doi:10.1029/2011WR010701.
120. Zeng, Y., Z. Su, L. Wan, and J. Wen, 2011b, Numerical analysis of air-water-heat flow in unsaturated soil: Is it necessary to consider airflow in land surface models? Journal of Geophysical Research: Atmospheres, v. 116, no. D20, doi:10.1029/2011JD015835.
121. Zhang, K., and J. Kevern, 2021, Review of porous asphalt pavements in cold regions: the state of practice and case study repository in design, construction, and maintenance: Journal of Infrastructure Preservation and Resilience, v. 2, no. 1, p. 4, doi:10.1186/s43065-021-00017-2.
122. Zhang, X., W. Presler, and Alaska University Transportation Center, 2012, Use of H2Ri wicking fabric to prevent frost boils in the Dalton Highway Beaver Slide area, Alaska final report., INE/AUTC 12.23.
123. Zhang, X., W. Presler, L. Li, D. Jones, and B. Odgers, 2014, Use of Wicking Fabric to Help Prevent Frost Boils in Alaskan Pavements: Journal of Materials in Civil Engineering, v. 26, no. 4, p. 728–740, doi:10.1061/(ASCE)MT.1943-5533.0000828.
124. Zhang, Y., L. Xiong, and L. Liu, 2019, A Comparison of Soil Improvement Techniques for Frost Heave Mitigation, in H. Shehata, and H. Poulos, eds., Latest Thoughts on Ground Improvement Techniques, Cham: Springer International Publishing, Sustainable Civil Infrastructures, p. 193–203, doi:10.1007/978-3-030-01917-4_16.
125. Zhao, Y., T. Nishimura, R. Hill, and T. Miyazaki, 2013, Determining Hydraulic Conductivity for Air-Filled Porosity in an Unsaturated Frozen Soil by the Multistep Outflow Method: Vadose Zone Journal, v. 12, no. 1, p. vzj2012.0061, doi:10.2136/vzj2012.0061.
126. Zornberg, J. G., M. Azevedo, M. Sikkema, and B. Odgers, 2017, Geosynthetics with enhanced lateral drainage capabilities in roadway systems: Transportation Geotechnics, v. 12, p. 85–100, doi:10.1016/j.trgeo.2017.08.008.

LIST OF NOTATIONS

Description	Symbol
Volumetric heat capacity of the soil mixture	C_v
Volumetric heat capacity	C_a
Heat capacity of soil particle	C_s
Heat capacity of unfrozen water	C_u
Heat capacity of ice	C_i
Temperature in the soil mixture	T
Nominal freezing temperature	T_m
Freezing temperature of the soil	T_f
Thermal conductivity of the soil mixture	λ
Thermal conductivity of saturated soil	λ_{sat}
Thermal conductivity of the dry soil	λ_{dry}
Normalized thermal conductivity	λ_r
Thermal conductivity of soil	λ_s
Thermal conductivity of unfrozen water	λ_u
Thermal conductivity of ice	λ_i
Empirical parameter depending on soil types (to calculate normalized thermal conductivity)	K_0
Relative hydraulic conductivity	K_{wr}
Material parameters accounting for the particle shape effect	χ
Material parameters accounting for the particle shape effect	η
Latent heat of fusion	L_f
Density of ice	ρ_i
Density of water	ρ_u
Volumetric mean pressure in the pore water	p_i

Volumetric mean pressure in the crystal	p_w
Interfacial free energy between solid and liquid	σ_{iw}
Radius of spherical ice particle	r
Effective pore radius	r_p
Segregation potential	SP_0
Water intake velocity	v_w
Temperature gradient at the freezing front	∇T
Frost heave deformation	Δd
Hydraulic conductivity of the soil	K_r
Saturated water hydraulic conductivity	K_s
Impedance factor related to ice content	I
Empirical parameters related to saturated hydraulic conductivity	E_i
Volumetric total water content	θ
Volumetric ice content	θ_i
Volumetric water content	θ_u
Total hydraulic head	h
Saturated matric potential	h_s
Degree of saturation	S
Effective saturation	S_e
Relative degree of saturation	S_{re}
Saturated degree of saturation	S_s
Residual degree of saturation	S_r
Hydraulic capacity	C_H
Van-Genuchten- Mualem fitting parameters	α_{vg}
Van-Genuchten- Mualem fitting parameters	n_{vg}
Unit vector along the direction of gravity	$\boldsymbol{i}$

Fourth-order tensor of material stiffness	C
Displacement vector	u
Body force vector	F
Porosity of the soil	n
Sink term	SI
Actual evaporation	AE
Potential evaporation	PE
Matric suction	ψ
Dimensional empirical parameter	ζ
Gravity acceleration	g
Molecular mass of water	w_v
Relative humidity of overlaying air	RH
Unit mass of water	γ_w
Universal gas constant	R
Slope of the saturation vapor pressure versus the temperature curve at the mean temperature of the air	Γ
Psychrometric constant	η_e
Heat budget	Q_n
Aerodynamic evaporative term	E_a
Wind speed	U_a
Saturation vapor pressure of the mean air temperature	e_{a0}
Actual vapor pressure of the air	e_a
Vapor pressure of the air at the air temperature T_a	$e^0(T)$
Air temperature	T_a
Maximum temperature of the air	T_{amax}
Minimum temperature of the air	T_{amin}
Minimum relative humidity of the air	RH_{amin}

Maximum relative humidity of the air	RH_{amax}
Cooling rate	U
The distance from origin	d
Groundwater level	l
With wicking fabric	WWF
Non-Wicking fabric	NWF
Displacement vector	u